MODELING AND SIMULATION STUDIES OF PULSE POWER SYSTEM WITH NANOSECOND RISE TIME FOR ULTRA WIDEBAND APPLICATIONS

By

SABYASACHI MITRA
ENGG01201004027

A thesis submitted to the

Board of Studies in Engineering Sciences

In partial fulfillment of requirements

for the Degree of

DOCTOR OF PHILOSOPHY

of

HOMI BHABHA NATIONAL INSTITUTE

April, 2018

Homi Bhabha National Institute

Recommendations of the Viva Voce Committee

As members of the Viva Voce Committee, we certify that we have read the dissertation prepared by Sabyasachi Mitra entitled "Modeling and Simulation Studies of Pulse Power System with Nanosecond Rise Time for UWB Applications" and recommend that it may be accepted as fulfilling the thesis requirement for the award of Degree of Doctor of Philosophy.

Chairman – Dr. A.P.Tiwari		Date: 13/4/18
Guide / Convener - Dr. Archana Sharma	Archana	Date: 13-4-18
Co-guide -		Date:
External Examiner – Dr. S.V.Kulkarni		Date: 13.04.18
Member 1- Dr. A.K. Bhattacharjee	AKBhattacharjee	Date: 13/04/2018
Member 2- Dr. V.H.Patankar	V.H.Patankar	Date: 13/04/18
Member 3- Dr. S.Kar	SKar	Date: 13.04.18

Final approval and acceptance of this thesis is contingent upon the candidate's submission of the final copies of the thesis to HBNI.

I/We hereby certify that I/we have read this thesis prepared under my/our direction and recommend that it may be accepted as fulfilling the thesis requirement.

Date: 16.04.18

Place: Mumbai

Archana

Guide (Dr. Archana Sharma)

STATEMENT BY AUTHOR

This dissertation has been submitted in partial fulfillment of requirements for an advanced degree at Homi Bhabha National Institute (HBNI) and is deposited in the Library to be made available to borrowers under rules of the HBNI.

Brief quotations from this dissertation are allowable without special permission, provided that accurate acknowledgement of source is made. Requests for permission for extended quotation from or reproduction of this manuscript in whole or in part may be granted by the Competent Authority of HBNI when in his or her judgment the proposed use of the material is in the interests of scholarship. In all other instances, however, permission must be obtained from the author.

Sabyasachi Mitra.

Sabyasachi Mitra

DECLARATION

I, hereby declare that the investigation presented in the thesis has been carried out by me. The work is original and has not been submitted earlier as a whole or in part for a degree / diploma at this or any other Institution / University.

Sabyasachi Mitra.

Sabyasachi Mitra

List of Publications arising from the thesis

- Sabyasachi Mitra, et al. “Computational estimation of sparkgap inductance in nitrogen medium” *Review of Scientific Instruments* vol. 85, pp.046112,2014; DOI: 10.1063/1.4871697.

- Sabyasachi Mitra, et al “Development of 125 kV, 5 ns Pulse Generator for Ultra Wide Band Applications”, *IEEE Transactions on Dielectrics and Electrical Insulation* Vol. 22, No. 4; 2015; DOI:10.1109/TDEI.2015.004760.

- S. Mitra, S. Singh, R. Kumar and A. Sharma, “Development of a novel voltage divider for measurement of sub-nanosecond rise time high voltage pulses” *Review of Scientific Instruments* 87, 024703 (2016)

- S. K. Singh, S. Mitra, Ranjeet Chaurasia, Archana Sharma and K. C. Mittal, “Balanced TEM Horn Antenna for UWB System with Sub nanosecond Rise Time”, *National Symposium on High Power Radio Frequency and Microwave, 4-6 Sep 2013*

- Sandeep Kumar Singh,, Sabyasachi Mitra, Pasula Naresh, Senthil Kalyanasundam, Ranjeet Chaurasia, Archana Sharma and Kailash C. Mittal, “A high power UWB system with subnanosecond rise time using balanced tem horn antenna” *IEEE International Power Modulator and High Voltage Conference,1-5 June,2013*.

Dedicated to Service of the Great Nation I Belong To…

ACKNOWLEDGEMENTS

First and foremost I would like to express my deep and sincere gratitude to my guides Dr. Archana Sharma and Dr. K. V. Nagesh for their valuable guidance, constant encouragement, inspiration and good wishes. I would like to thank Dr. A. K. Ray, Dr. L. M. Gantayet, Shri D. P. Chakravarthy, Dr. K. C. Mittal and Shri R. K. Rajawat for their contributions, comments and insights during the course of the research work.

I must thank to my doctoral committee chairman Prof. A.P. Tiwari for his continuous support and valuable suggestions during my research work and for monitoring my progress every year. I would like to express my sincere thanks to my doctoral committee members, Prof. A. K. Bhattacharjee, Prof. S. V. G. Ravindranath, Prof. V. H. Patankar , Prof. D. C. Kar and Prof. S. Kar for their valuable comments and suggestions throughout this journey.

I wish to show my sincere thanks to my colleague Mr. Sandeep Singh, Mr. K. Senthil, Mr. Ankur Patel, Mr.V. K. Sharma, Dr. A. Roy, Mr. Romesh Chadra, Mr. Rehim Rajan, Mr. P. C. Saroj, Mr. Satendra Dagore, Mrs. Rakhee Menon and Mrs. Ritu Agarwal for their help, motivation and cooperation.

I would like to express my special thanks to Dr. C.S. Reddy, Dr. S.V. Tewari, Dr. Pasula Naresh for helping me in this endeavor as companions. I would like to take this opportunity to thank Mr. Ranjeet chaurasiya, Mr. Danish mirza Beig, Mr. Sachin Patil, Mr. Sharad Vaity for their continued support in realization and implementation of technical aspects of the experiments.

This journey would not have started without dreams of two persons, my parents, who wanted to see me achieving this goal. Smiles in their faces, in my success, have remained the greatest motivation in this long journey. I would like to thank my wife for her support in tougher times and daughter for looking up to me always. This has encouraged me to strive beyond the obvious.

Finally, I would like to thank the Department of Atomic Energy for providing me the opportunity and funding my Doctoral research work.

Sabyasachi Mitra.

Date: 13.04.18 Sabyasachi Mitra

MODELING AND SIMULATION STUDIES OF PULSE POWER SYSTEM WITH NANOSECOND RISE TIME FOR ULTRA WIDEBAND APPLICATIONS

By

SABYASACHI MITRA
ENGG01201004027

A thesis submitted to the

Board of Studies in Engineering Sciences

In partial fulfillment of requirements

for the Degree of

DOCTOR OF PHILOSOPHY

of

HOMI BHABHA NATIONAL INSTITUTE

April, 2018

Chapter 1
Introduction

Extensive work is being carried out in the field of compressed high voltage high energy pulses for their immense importance in strategic applications [1,2]. Different laboratories in the world are persistently making efforts in generation of shorter pulses (in the range of 5-10 ns) of very fast rise time (sub nanoseconds to about a nanosecond). These pulses will contain high power ultra wide band (UWB) frequencies ranging from 100 MHz to 1 GHz and can be extremely susceptible and lethal for modern day electronics of wide range and variety [3-6]. These kinds of high energy pulses (1-5 Joules) or more can be fed directly to a matched broad band antenna to launch into the environment [7-10]. In this project, an attempt is made in generation and shaping of a high voltage pulse of 100-250 kV, 50-100 Ω, and 5-10 ns pulse width. Different methodologies have been reported about generation of such short pulses of bipolar or uni-polar nature in literatures [11-13]. Pulse forming lines, double pulse forming lines, Marx generators, and LC generators are a few of such equipments. Further challenges are involved in reduction of pulse width and increment of energy content of the pulse simultaneously, as it eventually affects the pulse shape. Use of optimized peaking capacitors and peaking gap is reported for improvement in rise time of short pulses. Performances of sparkgaps play one of the most vital roles in determining rise time of the output pulse [33]. Dynamic resistance and inductance of the sparkgaps need to be computed and minimized, to generate suitable pulse shapes for UWB applications. Different gas mixtures (i.e. nitrogen, sulphar hexa floride, argon etc.) at very high pressure have been suggested to achieve fast rise time [32]. Use of multi channel sparkgaps is one of the most reliable methodologies in the reduction of rise time. Development efforts involved behind them are extremely complicated in the nanosecond and sub nanosecond time range. This involves simultaneous triggering of multiple points of sparkgap with a delay of merely a few hundred picoseconds. Extremely low tolerance for jitter makes the design complex.

1.1 Typical pulsed power system for UWB application

The essence of pulse power lies in efficient pulse compression. It starts with normal continuous supply of 240V/ 415V and stepwise converts to the output of nanoseconds duration. Typical pulsed power systems are composed of four components i.e. High Voltage DC (HVDC) power supply, High voltage pulse generator (MARX generator [16,17] or Tesla transformer [18-19]), pulse forming

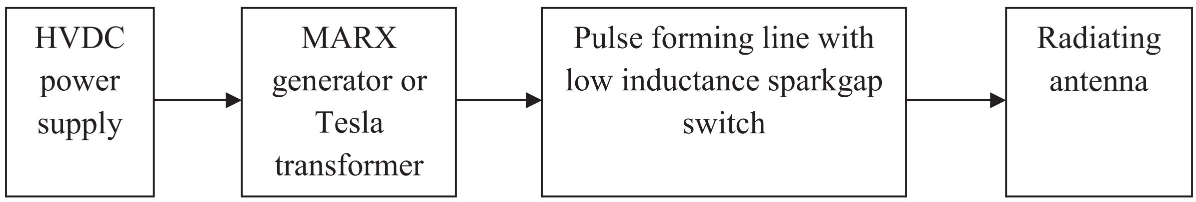

Fig.1.1 Block diagram of various sub-systems of an Ultra wideband system

line with low inductance sparkgap switch and a radiating antenna as shown in the block diagram of figure 1.1. Mostly HVDC power supply is commercially available up to 50 kV-60 kV range. To generate further higher voltage i.e. 100 kV to 1 MV or higher, usually a multiplier circuits like Cockroft Walton for DC and MARX generator or Tesla transformer are used for pulse output. These pulsed power equipments generate high voltage pulses of small width (100 ns to 1 µS). MARX generator charges capacitors in parallel and sequentially discharges them in series using sparkgap switches. The equivalent circuit diagram of a MARX generator is shown in figure 1.2. Pulse forming lines (PFL) are used for shaping and forming a pulse to the desired specification. Electrical equivalence of a pulse forming line is an infinite pi network, as shown in figure 1.5. A pulse charged from the MARX generator or Tesla transformer is discharged into a matched load through a fast sparkgap switch generating a square pulse at the output. Time duration of the pulse is decided by the length of the line and the wave travel velocity of the voltage wave front in the line.

1.2 Challenges in high power UWB systems

As reported in published literature worldwide, complexity of designing high power UWB systems is in their size and dimension. It is extremely desirable to get a sub nanoseconds fast rise time high voltage pulse source to realize a compact size UWB system. But containing extreme high voltage in the range of hundreds of kV in small dimensions is very difficult due to flashover issues whereas bigger size pulse forming lines and spark gap switches increase inductance of the discharge path. This eventually increases the rise time of the pulse. Thus requirements are contradictory in terms of high voltage (need more gap or track length) and low inductance (as close as possible). To resolve this problem usually fast MARX generators or Tesla transformers are used for charging of the pulse forming line, so that the applied electrical stresses can be enhanced without breakdown of the insulating medium. This reduces application time of high voltage and reduces probability of high voltage breakdown. However, designing of a fast MARX generator is again very complicated because of its complex geometry, multiple dielectrics and statistical variation in behavior. Moreover stray capacitances play very significant role in operation and behavior of low energy

MARX generators. These stray capacitances are difficult to estimate and make design of low energy MARX generator further complicated.

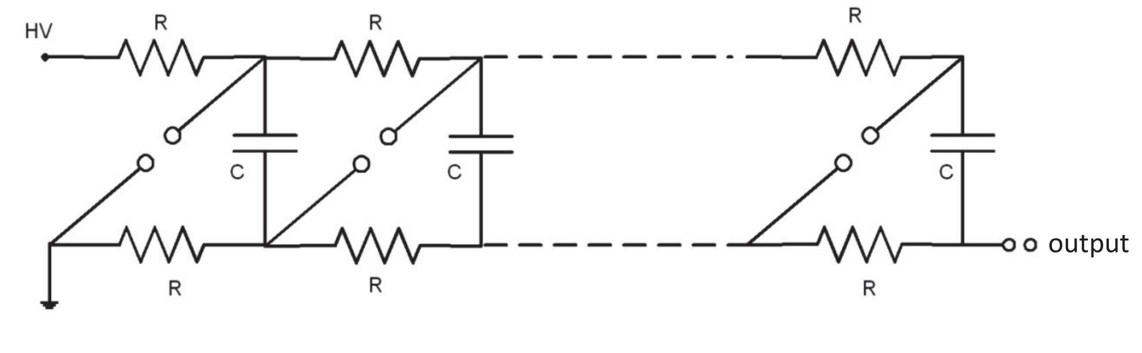

Fig.1.2 Equivalent circuit diagram of MARX generator

A sparkgap is a high voltage switch. Before firing sparkgap switch offers stray capacitance. After getting closed through an arc channel, it offers finite resistance and inductance depending on its structure and geometry. The resistance of a sparkgap switch is assumed to be extremely high while open. Upon closing, it gradually comes down to a very small resistance of few milli ohms with time. These spark gap switches are usually modeled as a capacitor parallel to a series connection of a resistance and an inductance. A typical sparkgap and its electrical equivalence are shown in figure 1.3 and figure 1.4 respectively. This resistance of sparkgap switch is time varying. The inductance of spark gap is a function of structure of the sparkgap and physical properties of the gas medium.

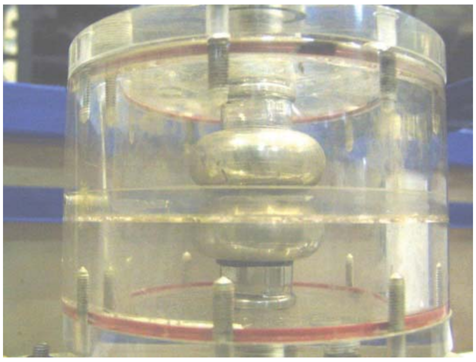

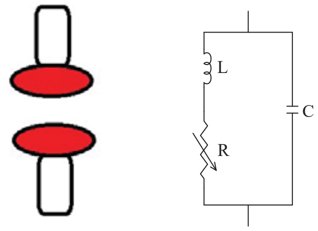

Fig.1.4 Equivalent circuit of sparkgap switch

Fig.1.3 photograph of typical sparkgap switch

Behavior of sparkgap inductance with respect to gas medium, pressure and gap between electrodes are not accurately calculable or predictable. These parameters play a crucial role in deciding rise time of high voltage pulse generated to feed UWB radiator. Moreover, structure of the sparkgap leading to antenna plays an important role in transmitting the high frequency components of the pulse to antenna load as shown in Fig.1.5. Frequency spectrum of the radiated pulse is shown in Fig.1.6. Any kind of discontinuity (in terms of impedance) will reflect on the pulse amplitude and shape significantly. Thus, design of the feed terminals becomes complex.

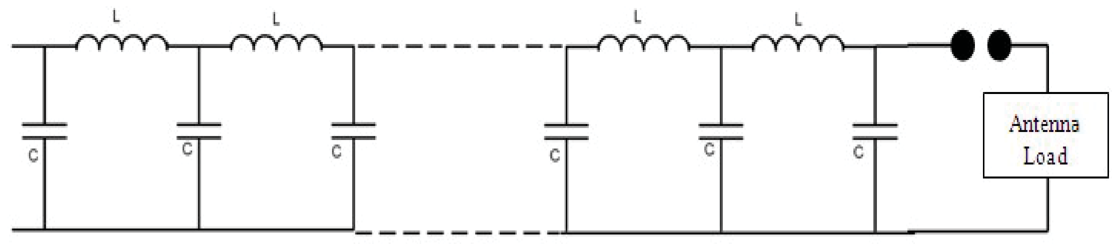

Fig.1.5 Typical schematic of Pulse forming Line with o/p switch and antenna load

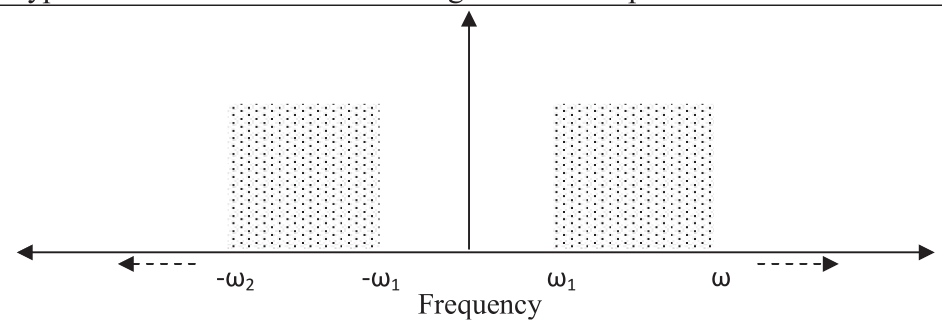

Fig.1.6 Typical frequency spectrum expected of UWB system

As most of the UWB pulsers operate at very high pressure (>30 bar), the UWB system requires mechanical compatibility of handling very high gas pressures i.e. 40-50 kg/cm^2. All these multidisciplinary requirements of engineering in a single structure make the design of a pulsed power source for UWB applications a challenging task.

1.3 Scope of this project

Under this thesis work, different types of pulsed power topologies suitable for UWB sources are studied and analyzed. In order to generate fast rise time pulse of sub nanosecond order rise time, inductance of final spark gap switch is identified as an important parameter to understand and optimize. Attempts are made to correlate the sparkgap inductance with gas medium, gas pressure and gap between electrodes.

A computer code has been developed to calculate arc channel growth with time during break down of a sparkgap. This code estimates arc channel diameter from the molecular and physical properties of the gas medium. It also estimates the inductance of the arc channel considering sparkgap enclosure as return path. Effect of different parameters on sparkgap arc channel is studied using this code. To validate the simulated results, acquired using the computer code, two experimental setups have been developed. One setup is for experiment up to 120 kV and 5 kg/cm^2 pressure and the other setup is up to 500 kV and up to 40 kg/cm^2 pressure. Experiments are carried out at various gas pressures, various gaps between electrodes and different gas media to understand their effect on inductance of spark gap arc channel. Details of experimental results and simulated results are elaborated in the thesis.

1.4 Thesis organization

In chapter 2, literature survey and present status of the worldwide available technology has been elaborated. Different types of reported UWB sources in variety of ranges (i.e mesoband, sub-hyper band, hyper band, etc.) are narrated in this chapter. Different types of pulsed power topologies used for these applications are studied in details and simulations are carried out to compare and understand their performance.

In chapter 3, simulation of the phenomena of arc channel growth with time has been elaborated. Arc channel dimensions are estimated based on temperature rise inside the arc channel with time. Inductance of arc channel is calculated based on arc radius obtained from the simulation and gap between the electrodes. Results obtained from the simulation show that the inductance of the arc channel increases with increase in the gas pressure and gap between the electrodes. The simulations also indicate that the inductance is higher in gases of higher molecular weight i.e. SF_6 (Sulphur hexa fluoride) compared to lighter gases i.e. N_2 (Nitrogen) or Ar (Argon). It is also indicated in the simulation that increase in the inductance due to increase in the electrode gap is much more significant compared to increase in pressure.

In chapter 4 detailed description of the experimental setup is provided. The experimental setup consists of a MARX generator, a pulse forming line and a sparkgap under test. Setup is so designed that experiments up to 5 kg/cm^2 can be carried out using this set up. This experimental setup is capable of generating 120 kV, 5 ns voltage pulses. Rise time of the pulse is measured using a specially designed load-cum-divider assembly. Details of the experimental setup and its components are provided in this chapter.

Chapter 5 illustrates the inductance measurement methodology in details. Rise time of the pulse is function of inductance of the sparkgap arc channel. Hence, inductance can be estimated from the rise time profile of the voltage pulse. Further in this chapter study of variation of gap and pressure on inductance of arc channel is carried out. Experiments are carried out by varying gap of electrodes from 1 mm to 9 mm in nitrogen atmosphere. During these experimental investigations, effect of gas pressure could be seen up to 5 kg/cm^2 (due to limitation of the experimental setup). Outcome of experimental results and simulated results are plotted to compare their trend.

In order to carry out the experimental investigations with higher pressure and gases with higher breakdown strength like SF_6, a different experimental setup was required. This new system was designed to generate 500 kV, 5 ns pulse and it was capable of handling pressure up to 40 kg/cm^2. In chapter 6 detailed description of this new experimental setup is provided. In this setup experiments are carried out with N_2 and SF_6 up to a pressure of 30 kg/cm^2 and 15 kg/cm^2 respectively.

Chapter 7 describes the experimental results for measurement of rise time and inductance. In this setup radiated measurements are used for measuring rise time and inductance of the sparkgap. Variation of the rise time in both gas media i.e. N_2 and SF_6 has been studied and analyzed.

In chapter 8, conclusions of the actual experimentations and studies have been presented with proposed future work.

Relevant references, referred in different sections of the thesis, are listed at the end of the thesis. Captured waveforms, experimental data and important mathematical identities used for statistical analysis of the experimental results, are enclosed in the appendix section of the thesis.

Chapter 2
Literature survey

In published literature research work is reported for selection of different types of pulse power source for suitability of Ultra Wide Band (UWB) applications. Studies related to source selection focuses mostly on reduction of erected inductances so that effective ranges of these high frequency pulses are increased. Different topologies like single pulse forming line [20] double pulse forming line or Tesla transformers [21] are attempted to reduce inductance in the discharge path. Further reports of methodologies to reduce inductance of switches like sparkgaps are also found [22, 23]. In this context variation of inductance of sparkgap with current and time are reported. Variation of inductance and rise time of spark gap with different gases as medium and mixtures of gases [24] with varied pressure [25] has been published. Multi channeling technology [26, 27] for reduction of inductance in various other applications is adopted successfully. For pulse shaping, use of peaking capacitor and peaking gap [28] and LASER triggering [29,30,31] is reported often, different modeling and analysis techniques are used for finding optimum shape, size and position of the capacitor.

2.1 Types of sources

2.1.1 Mesoband Sources: Mesoband sources have been successfully designed and built to generate high-power microwave frequency between 100 MHz and 700 MHz . These sources are typically designed in two different ways. Either a damped sine waveform is fed into a wideband antenna, or a wideband transient (from a Marx generator, for example) is switched into an antenna with elements of differing lengths in order to radiate a broad range of frequencies. Following the first method, Baum has

[12] described certain concepts that switch a high-voltage transmission line oscillator into a wideband antenna. The oscillator consists of a quarter wave section of a transmission line charged by a high-voltage source. It employs a self-breaking switch at the lower end of the transmission line. When the switch closes, the system generates a damped sine signal that is fed into an UWB antenna such as a half of an impulse radiating antenna (IRA). An initial working model of this type of source, called the MATRIX. It began full-scale testing at the Air Force Research Laboratory (AFRL) during 2003. It consists of quarter-wave transmission line charged to 150 kV connected to a 3.667-m (12 ft) diameter half-IRA. The frequency of oscillation is adjustable between 180 MHz and 600 MHz . It radiates a damped sine waveform with a peak electric field of 6 kV/m at 15 m with a percent bandwidth of about 10% (band ratio of 1.10). Following the second method, a number of mesoband sources are manufactured by DIEHL Munitions system in Germany. These include the DS110 series of damped sine sources. The radiated field and spectrum is measured at 1 m with a center frequency of 375 MHz from a pulsed source operating at 400 kV. DIEHL also makes the DS350, a very high-power device that produces high fields at 100 MHz from a full 1-MV generator. The DS350 system is a modular laboratory device specifically designed for effects testing. The system uses a multi-rod dipole antenna with a center switch. It will radiate a maximum of 300 kV/m at 1 m. The antenna voltage can be as high as 1 MV, and the peak radiated power is as high as 2 GW. Mesoband oscillators are also made by BAE Systems, Sowerby Research Center, U.K. These oscillators are unique solid-state modulators based on a nonlinear transmission line (NLTL) design. They generate very high Q damped sine waves with up to 50 oscillations per pulse and voltages exceeding 50 kV. Frequencies range from

10 MHz to 2 GHz, with PRFs in excess of 1 kHz. More advanced systems have the ability to chirp over a 40% tuning range.

2.1.2. Sub-hyperband Sources: The H-Series devices built at the Air Force Research Laboratory in Albuquerque, NM, use coaxial pulse-forming lines and high-pressure hydrogen switches to produce powerful and very compact UWB pulses. One of the most successful designs of the H-Series, the H-2, is built around a 4m diameter and forty coaxial lines. The H-2 source first became operational in late 1992 and was subsequently upgraded in 2000. It generates a prompt 300 kV pulse with a rise time of 250 ps and a total pulse length of 1.5 ns to 2 ns with a considerable amount of late-time, low-frequency ringing [10]. When fired into a large unbalanced TEM horn, the system radiates a sub-hyperband spectrum with maximum spectral amplitude around 150 MHz. The peak electric field strength has been measured to be 43 kV/m at 10 m, with a rise time of 238 ps. Another powerful sub-hyperband system is the Transient High Output Radiator (THOR), currently in use by the United States Navy at China Lake, CA. Maximum voltage into the antenna is 1 MV, giving a radiated waveform with a peak electric field of 68 kV/m at 10 m with a rise time of 200 ps and a pulse width [full-width at half-maximum (FWHM)] of 400 ps. The waveform and spectrum are similar to that of H-2. The spectrum contains energy between 200 MHz and 1 GHz with the maximum occurring at 280 MHz.

2.1.3. Hyperband Sources

1) Balanced Sources: The impulse radiating antenna (IRA) systems, which produce a high-power electromagnetic (HPEM) signal with a band ratio greater than two decades, are good examples of high-power hyperband sources. The original IRA, developed and fielded in 1994, used a high-pressure hydrogen switch, a focusing lens, and a four-arm TEM horn to produce an extremely powerful hyperband pulse from a

4-m reflector. With a charge of only 60 kV, this system generates a transient signal with a peak electric field of 4.6 kV/m at a range r = 305 m with a maximum PRF of 200 Hz. The IRA I system was subsequently refitted to a 2 m reflector, and designated the IRA II. The radiated spectrum of the 2 m IRA has been measured to be flat from 200 MHz to around 3 GHz with a band ratio of 10. Another compact, powerful balanced hyper band system is also being built for the United States Army in Huntsville, Alabama. Combining a 400 kV Marx made by Applied Physical Electronics, LC, San Antonio, TX, with a 1.2 m IRA by Farr Research, Inc., Albuquerque, NM, and the Army has created a useful system for electronics testing [11]. A number of companies and institutions in Europe have also developed small hyperband sources for UWB radars and landmine detection. Impulse radiating systems have been made by Otto von Guericke University, Magdeburg, Germany, TNO in the Netherlands, Spiez in Switzerland, the Royal Military Academy in Belgium, and U.K. The German and Dutch IRAs are based on a 9-kV pulser operating into a 0.9-m parabolic. They deliver 7 kV/m at 1 m with a risetime of 100 ps and a pulse width of 4 ns, at 800 Hz. The system in Spiez is based on a 2.8-kV pulser operating into a 1.8-m parabolic. It delivers 220 V/m at 41 m with a rise time of 100 ps, a pulse width of 4 ns, and a PRF of 800 Hz. DIEHL also makes a very compact hyperband source called the HRR32. It is a self-contained unit about the size of a coffee can that delivers 2 kV into an internal or external antenna and will deliver a peak power of 7 kW at 600 Hz.

2) Unbalanced Sources: The design of balanced hyperband sources such as the IRAs presents some difficulties, particularly at very high voltages where trigger jitter or BALUN design becomes an issue. In some cases, it is preferable to design a half-IRA

over a symmetry plane so that the high-voltage signal can be fed directly to the antenna from below with a coaxial transmission line. Such sources make the high-voltage problem much more tractable, but they do not have the uniformly symmetric field pattern of a full parabolic antenna due to the presence of the finite ground plane. One such unit, built by the AFRL from 1997 to 1999, was designated the "Jolt" [12]. This large, transient system is powered by a very compact 1-MV resonant transformer that is connected, via an integrated transfer capacitor and an oil peaking switch, into an half-IRA. This unique system will deliver a tightly focused radiated field with a FWHM on the order of 100 ps and a field-range product of approximately 5.3 MV at 200m. A similar unit built by WIS and Rheinm *etal* in Germany. It consists of a half-IRA antenna driven by a 100 kV Marx generator that radiates an impulsive wave form with a peak electric field of several kV/m at 100 m, a rise time of 100 ps, and a pulse duration of 650 ps.

2.2 Various types of UWB generators

According to conventional terminology, a pulse generator is classified as a sub-nanosecond one if the front of the output nanosecond pulse or the total pulse duration is shorter than 1 ns. In the latter case, two types of generators can be discerned [4]. They differ by the principle by which the energy accumulated in the storage of the nanosecond stage is utilized. These are shapers "cutting" a short pulse out of a longer one without a change in the power of the initial pulse or devices executing an amplitude-to-time conversion (pulse compression). Generators allowing for shaping 100 kV pulses across loads of tens of ohms can be referred to as high power subnanosecond pulse devices. Design of short pulse generators has contradictory requirements. For fast energy disposal of sub-nanosecond regime capacitance of these forming lines or energy storage elements need to be very small, which in a way restricts its dimension. However to handle high voltage, proper feed through and other insulators demand more thickness and surface separation between high voltage and ground. It is difficult to meet these requirements simultaneously. Hence in most of the system double stage compression is preferred. A high voltage pulse of tens of nano second is generated in the first stage, which charges the second stage forming lines. Second stage forming lines are designed assuming overvoltage operation of smaller time, utilizing the known effect of increase in the breakdown strength of the insulation with decreasing time of voltage action.

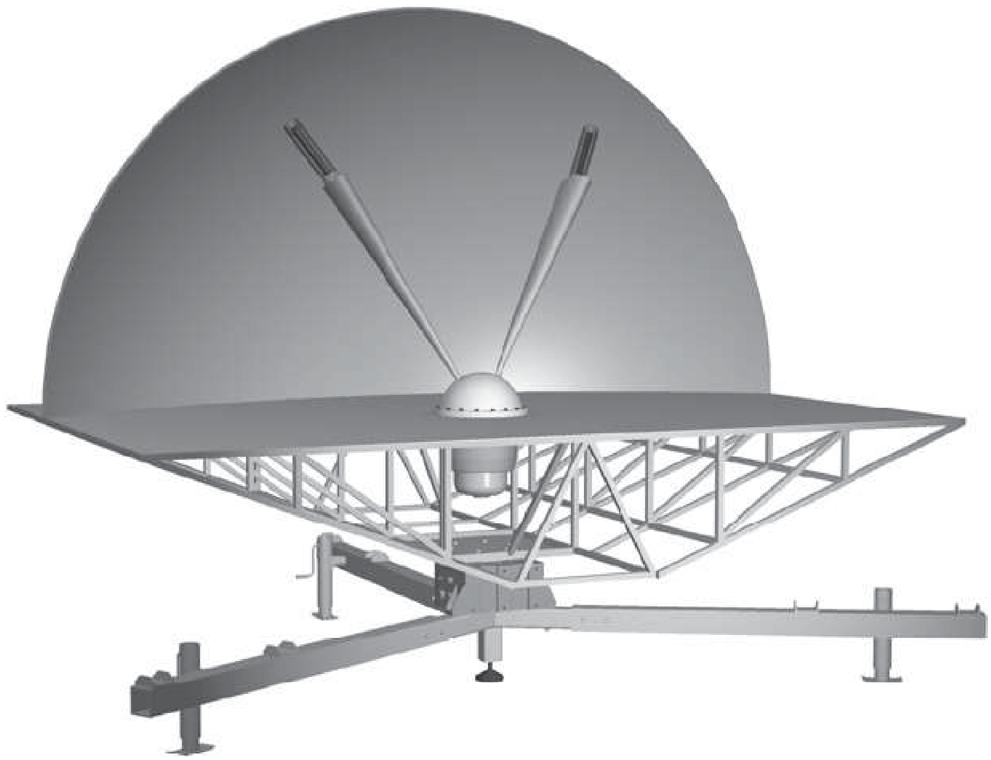

Fig.2.1 MATRIX switched oscillator source [7]

Hence, it is usually impossible to create a high-power sub-nanosecond pulse without a nanosecond compression stage; therefore, a basic element of each of the aforementioned devices is a generator which is able to form pulses of nanosecond duration. Each design of high-current sub-nanosecond generators includes a nanosecond high voltage generator (driver), whose characteristics substantially determine the output parameters and operating modes of a sub-nanosecond device as a whole. A common feature of all designs is an additional (peaking) spark gap set up at the driver output operating by the leading edge of the driver pulse (~ 1 ns). The nanosecond drivers used in practice were most frequently represented by fast Marx generators or forming lines with different versions of pulsed charging. A compressed gas (nitrogen, hydrogen) or liquid dielectric (usually transformer oil) was used as the working medium of the spark gap switches. In the latter case, a basic drawback of the devices with high pulse repetition rates is the complexity of the systems for removing oil-decomposition products from the discharge gap after each breakdown. Gas spark gaps have shown their advantages, in contrast to SGSs with liquid dielectrics, they allow controlling the breakdown voltage within a wide range by variation of the gas pressure and composition at a constant electrode gap. Different types of drivers or generators suitable for UWB applications are reported in literature. These generators are broadly classified and described below.

Generators with sharpening and cutting of nanosecond pulses: Sub-nanosecond generators with sequential sharpening and cutting of the initial nanosecond pulse are often used despite their comparatively low energy efficiency. Literature reports different versions of such schemes, which differ by the type of the cutting device. For sharpening of pulse front sparkgap switch is used in general. For pulse shortening, mainly two types of cutting arrangements are observed in literature a) use of sharpening spark gap switch [31] b) connecting short circuited coaxial line connected parallel to the load [6]. In the sub-nanosecond range, breakdown strengths of all the insulators usually increase.

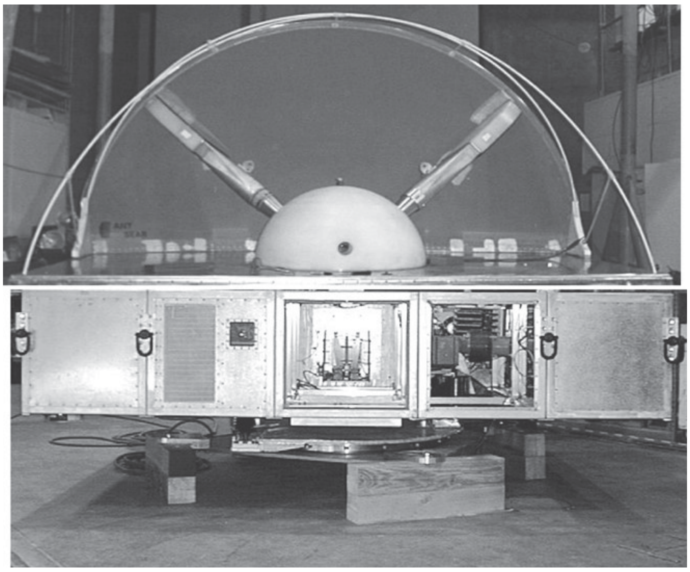

Fig.2.2 Photograph of JOLT system [12]

Energy Compression: From the standpoint of the energy efficiency of subnanosecond generators, a circuit with energy compression has an obvious advantage. In order to perform a time–amplitude conversion of the pulse energy, an additional capacitive storage is set up at the driver output. Usually multiple stages of capacitive storage and transfer of energy from one capacitor to another is carried out in this method. This topology has been experimented in SINUS-5 system at a voltage level of 700-900 kV.

Generators of bipolar sub-nanosecond pulses: A symmetrical bipolar pulse of double duration and a swing of $\pm U_1/2$ can be produced from a short initial traveling pulse with the amplitude U_1 or using modified Vvedenskii circuit [32] based on the simultaneous operation of two sparkgap switches (SGSs) located at the opposite ends of the forming line. High-voltage bipolar pulses with a total duration of ~0.5 ns were shaped by using a generator based on a RADAN-303 nanosecond driver and a subnanosecond converter with sharpening spark gap switches. Biggest advantage of this type of generator is that maximum amount of energy can be transmitted using antenna as the pulse generated using this type of driver is bipolar.

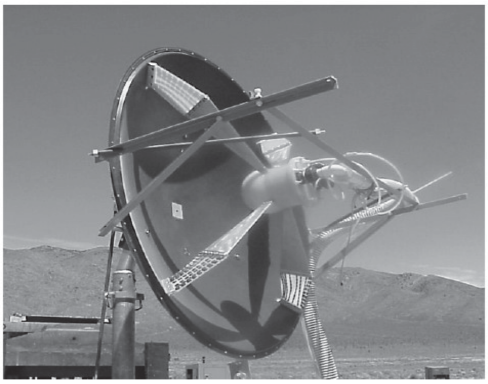

Fig.2.3 IRA II [1]

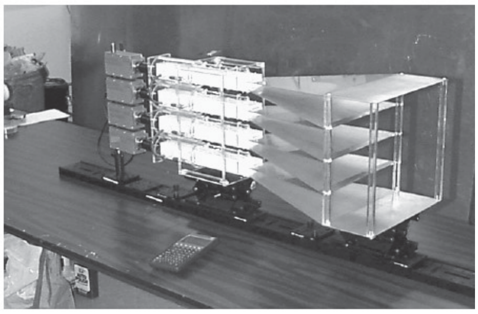

Fig.2.4 Four-element array antenna [2]

2.3 Study and simulation of reported UWB sources

For better understanding of the proposed topologies mentioned in different literatures are simulated using standard circuit simulation software. This gives a clear picture of circuit components of different topologies and criticality involved in achieving different parameters to get the expected results. Below is the table showing different topologies reported in literature and expected results obtained from simulations of the same.

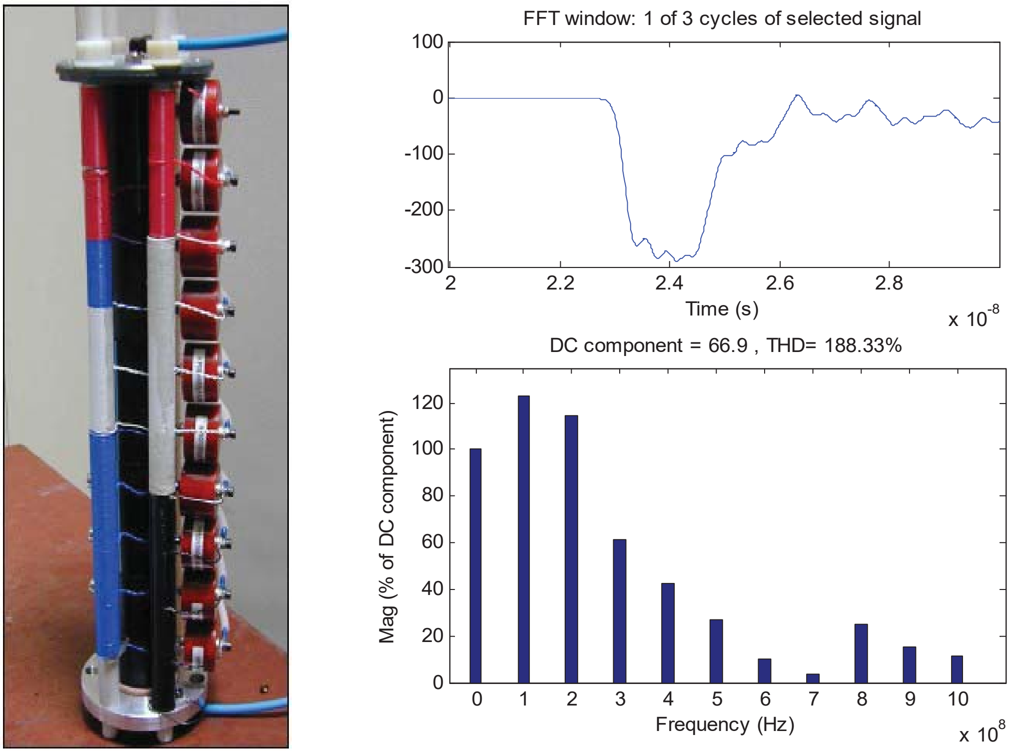

Fig.2.5. Repetitive auto-triggered MARX generator as the driver of an ultra wide band source by Cadilhon etal. and its simulated output. [17]

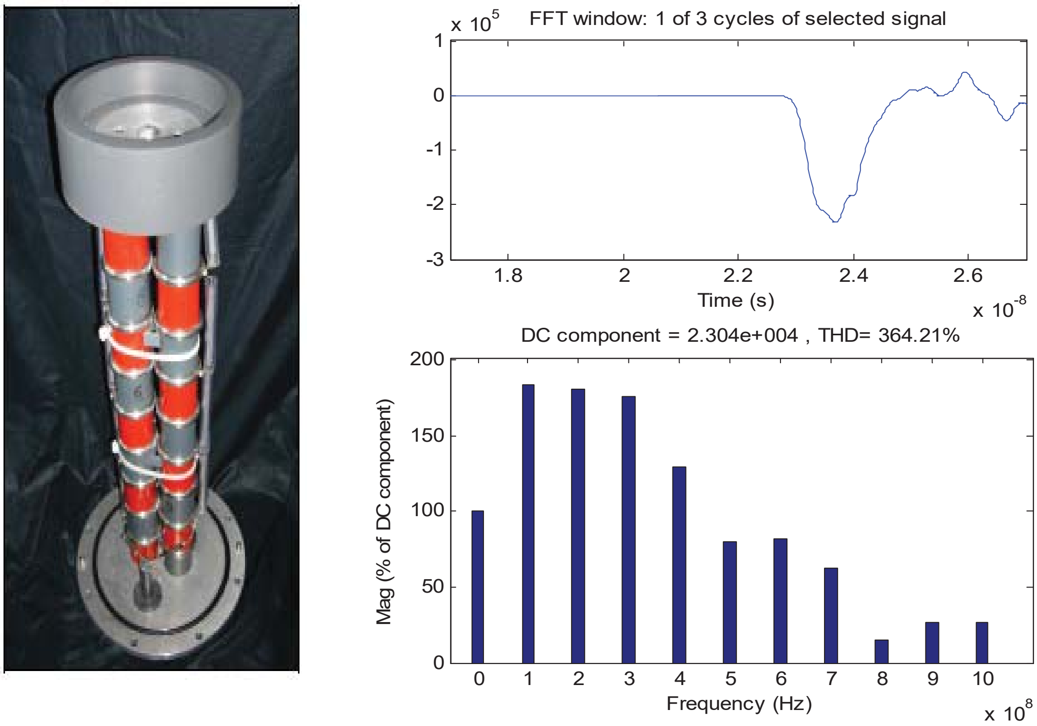

Fig.2.6. A 250 kV, 300 ps, 350 Hz MARX generator as UWB source and its simulated output [16].

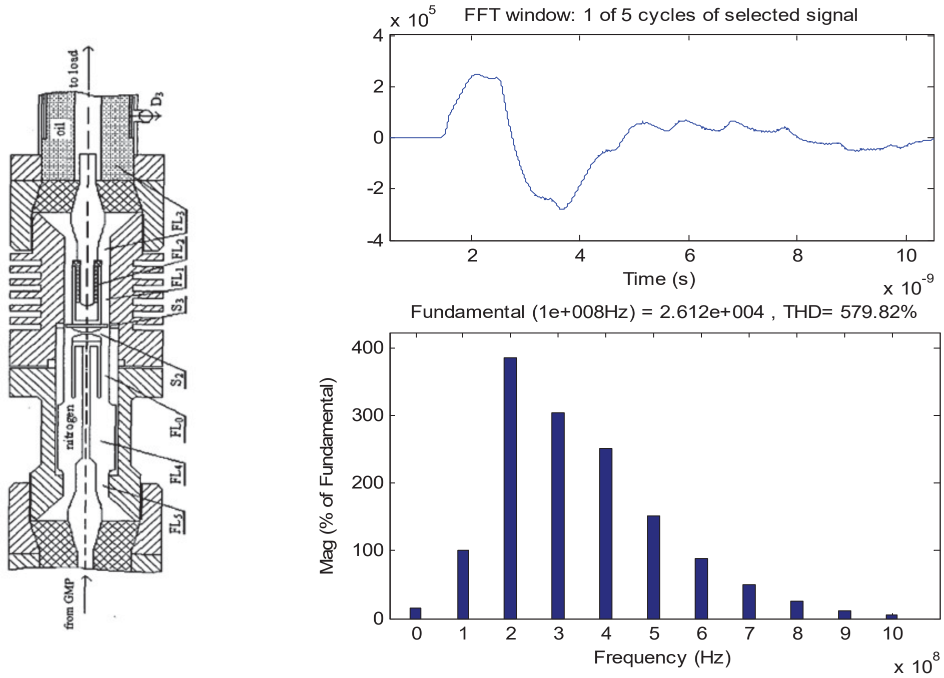

Fig.2.7 bipolar pulse former by Andreev et al. and its simulated output [21]

2.4 Multi-channeling for reduction of arc channel inductance

Multiple arc channel formation is one of the proven techniques of reduction of inductance related to sparkgap. Due to formation of multiple channels in the sparkgap, effective arc radius increases by several folds. This reduces inductances of the loop drastically. Technology involved in multi-channeling is tricky and involved. *Kim A. A., Kovalchuk B. M., Kremnev V. V., Kumpjak E. V., Novikov A. A.,* has elaborated the importance of multi-channeling and allied technologies in getting low inductance spark gap [23]. Fast rise time of charging pulse, minutely synchronized multiple trigger signal and extreme low jitter plays key role in successful implementation of multi-channeling. In this context many attempts are observed in the direction of LASER triggering. Nd-YAG LASER beams of picoseconds duration are used for this purpose of synchronized multi-channeling of sparkgaps [30, 31]. But this is very costly technology and not in the scope of this project as concentration has been devoted to un-triggered or self breakdown sparkgaps only, in this project.

2.5 Estimation of sparkgap inductance

Analyzing, anticipating and designing low inductance sparkgap switch is the inherent art of getting good UWB systems. A lot of work is going on worldwide in reducing the inductance of spark gap switches by varying gap, pressure, dielectric configuration and gap medium etc. Several models also have been developed to understand the inductance of spark gap channels. Different theories like town-send breakdown mechanism, avalanche model etc. tries to explain the phenomena reasonably well within their limitations [39]. However, pulsed breakdown phenomena, mostly, depends on experimental results, analysis of the results and empirical formulas. These are provided by J.C.Martin *etal.* for use in engineering and technological applications [40]. Lots of useful data: results of experiments and calculations are given by Yu.P. Raizer [41] . Paschen curve is used worldwide for understanding of gas discharges for wide range of applications. Petrovic et al. have validated the same even to micro discharge ranges [42]. Experimental results in case of gaseous breakdown exhibit statistical variation [43]. This is mostly attributed to purity of the experimental medium and effect of polluting particles in it. In high voltage breakdown, it is mostly believed, that affect of unwanted small particles in the experimental medium affect the experimental results drastically [39]. Many literatures emphasize the importance of secondary electrons in high voltage breakdown phenomena [44]. Studies carried out in different gas medium to understand the breakdown phenomena in gases, are reported in literatures [45].

2.5.1 Analytical calculation of arc channel inductance

Theoretical modeling of sparkgap channels are done by P. Persephonis, K. Vlachos, C. Georgiades, and J. Parthenios and attempted to match with experimental observations [34]. The inductance of an arc discharge has been modeled and a mathematical formula given for the arc inductance in terms of its geometrical dimensions by the authors in his paper. This formula agrees with the experimental results and can be used to determine the arc-channel radius within a specified operating range. Inductance measurements have been taken for various values of pressure, inter-electrode distance and applied voltage in a triggered spark gap. The dependence of inductance upon these parameters has been explained through the existing variations of the arc-channel cross section. Two mechanisms have been identified responsible for the variations of inductance. The first is diffusion and the second is the tendency of the current channel to vary diameter with pressure, inter-electrode distance and applied voltage.

2.5.2 Thermal profile of arc channel

Thermal characteristics of sparkgap channel are calculated by Ryo Ono et al. [35, 36] analytically, to understand thermal phenomena of the arc channel. During the period of switching, arc channel resistance changes from very high value of several mega Ohms (almost open circuit) to very low (almost short circuit) of few mili Ohms. Radius of the channel and inductance also becomes time varying, as current flowing through the arc channel changes. The rotational and vibrational temperatures of the N_2 molecule were measured in the capacitance spark discharge in air by Reza Najafzadeh and Ernest E. Bergmann [36]. The discharge voltage was 3.0–3.5 kV and the discharge energy was 0.03–1 mJ. The rotational and vibrational temperatures were estimated at approximately 500 K and 5000 K, respectively, independent of the discharge energy. This indicates that most of the electron energy is consumed for the excitation of vibrational levels. The expansion of the shock front of a laser-triggered, atmospheric air spark was studied by shadow photography with a transversely excited atmospheric UV nitrogen laser. It was found that the shock front of the short spark (0.5 mm) was cylindrical. Within a few nanoseconds of spark formation the diameter of the spark channel grows with time and the index of refraction is less than the surrounding gas.

2.5.3 Calculation of composition of arc plasma

Literatures narrate the elaborate methodology of calculation of arc plasma as function of temperature. By using Saha's equation, it is possible to calculate the ionization fraction of gases. S. Kuhlbrodt categorically details the methodology of calculations, to analyze the percentage of different ions and electrons fraction present in gas plasma [46]. For different gases i.e. Argon, sulphar hexa fluoride, nitrogen etc. it is possible to calculate the composition of plasma from its temperature. Ion fractions are function of temperature, ionization energies and spin factors of atoms. All other required physical parameter data are available in chemistry hand books. The methodology of calculation and results for different gases are given in many literatures published in reputed journals.

P. Swarbrick mentions [47] that composition of the SF_6 arc plasma can be determined by solving the various equations governing the gas particles of the plasma. Also, the electrical and thermal conductivities can be calculated; calculated results are in reasonable agreement with measured values obtained by Motschmann (1966). The significant differences between the properties of the SF_6 plasma and those of nitrogen have been shown to account for the different characteristics of the static arc and the transient circuit-breaker arc in the two gases. P. Swarbrick mentions that at low temperatures, the formation of negative fluorine ions in the plasma drastically reduces the electrical conductivity and results in the SF_6 arc gap being able to withstand very high rates of rise of recovery voltage following a critical current zero. In general the thermal conductivity of the SF_6 arc plasma is lower than that of nitrogen, thus explains, higher temperature gradients and lower voltage gradients, which had been experimentally observed in SF_6 arcs. In the literature [48] by Yasunori Tanaka *etal*, particle composition of plasma at 0.1 MPa in two temperature states was theoretically calculated, in which electron temperature is higher than gas temperature.

Similar work on nitrogen plasma has been carried out by P.Andre. It has been reported [49] that ion composition of nitrogen plasma can be calculated using analytical equations. Analytically calculated results and practical data are reported thoroughly. Calculation of ion composition of noble gas plasmas have been carried out by S. Kuhlbrodt et al. They have summarized the experimental data for the electrical conductivity of noble gas plasmas which were obtained over a few decades from explosively driven shock-wave experiments [46]. These results show a transition from nonmetallic to metallic-like behavior at high pressures. This transition can be explained qualitatively by pressure ionization of neutral atoms and the subsequent excitation of higher ionization stages. While the general tendencies in the behavior of the electrical conductivity are reproduced by the present theoretical approach, a detailed comparison of the equation of state data with experimental results is still lacking.

2.5.4 Estimation of conductivity of arc channel

Bottin et al. have explained the methodology of calculating plasma properties from its ion composition [50]. Throughout this paper they have reviewed the state-of-the-art of accurate models for transport properties of collision-dominated dilute perfect gas mixtures at low pressures and high temperatures, conditions which, in the aerospace field, are mostly encountered in the domains of high-speed and (re)entry flights, high-enthalpy facilities, and combustion processes. The accurate computation of the transport coefficients requires the knowledge of a broad spectrum of physical processes, accurate collision data and rigorous programming techniques.

Transport properties of collision-dominated dilute perfect gases can be computed by following the analysis of Chapman and Enskog [50], a statistical mechanics description of a mixture of particles subject to elastic binary collisions. The model described in the literature is valid provided that the plasma remains collision-dominated at all times, implying that the chemical reactions have no influence on the collisions, that the Debye length remains small, that the Coulomb potential is effectively screened, and that the plasma is un-magnetized. The analysis uses the hypothesis of small electron mass to simplify the expressions and it allows for weak thermal non-equilibrium conditions.

Using the classical spectral decomposition of the first-order perturbation of the equilibrium solution of the Boltzmann equation, expressions for the coefficients of viscosity, heavy species thermal conductivity, electron thermal conductivity, electrical conductivity and diffusion velocities can be expressed in terms of Laguerre–Sonine polynomials. The internal energy states are treated by way of Eucken's approximation. All the detailed expressions have been provided in this literature; they only require accurate values of the collision integrals between the species considered in the mixture.

The transport coefficients appear as solutions of linear systems of equations. The present model is recommended in all types of applications since it outperforms the so-called mixture rules approximate models in both speed and accuracy. Accurate collision integrals constitute the key parameter in the accuracy of the coefficients. Several sources of data have been referenced, and results for air mixtures provide examples of the sensitivity of the computed values to the collision integrals used. The most classical interaction potentials used today have been presented as background information. Finally, this review paper examines some analytical developments which can be carried out in the important practical case of thermo-chemical equilibrium conditions.

2.5.5 Application of numerical methods to estimate arc channel inductance

Many problems in scattering theory can be reduced to mathematical formulae containing the classical angle of deflection and the scattering phase shift. Since these values have often to be evaluated a large number of times in a single problem, it is important that they should be evaluated as efficiently as possible. For solving of deflection angle effective methodology is suggested by F. J. Smith [51].

With advancement of computer technology and simulation techniques, attempts has been made in critically analyzing the phenomena of arc channel formation and related dynamic variation of resistance, arc radius, current distribution and arc inductance. Numerical methodology has been used by Han & Han to calculate arc channel characteristics numerically [22]. Authors have found that, time dependent inductance of the field distortion spark gap largely influence the rise time of the output pulse of the pulsed power device. A new parameter estimation model, which used DFP imitation Newton method and four rank Runge-Kutta method, has been built. The value of the calculated inductance corresponds to that from experiment.

2.6 Conclusion

J.M. Lehr, C.E. Baum, W.D. Prather and F. J. Agee discusses the issues related to arc channel characteristics and ultrafast sparkgap switching in designing UWB generators [33]. The peak achievable rise time has been examined in three ways: investigation of critical carrier production rate to produce an electron avalanche which results in closure of a gaseous spark gaps; an examination of the limits imposed by the propagation of an electromagnetic wave in transmission line encased spark gap; the third method results from a circuit model of the sparkgap after breakdown. Results reported by the authors are in good agreement to their calculations.

In this thesis, all these previously reported work is ensemble to analytically find out arc channel inductance of a spark gap switch. Analytical model of A.Wells has been enhanced with numerical calculations. Code has been developed to calculate electrical parameters of the arc channel for a small time step. Temperature distribution of arc channel has been calculated using the same code and joule heating concepts [37]. Once temperature of the arc channel and its distribution is known, ion composition of the plasma is calculated following the methodologies given by S. Kuhlbrodt [46] and P.Andre [49]. These results are used to calculate transport properties of gas plasma and electrical conductivity of the same using Chapman- Enskog equations given by Bottin et al. [50]. Electrical conductivity of plasmas as function of temperature is also readily available in many literatures. Those data tables can also be directly used for the purpose of calculations. These calculations are iterated for each time step to find out evolution of arc channel. This code is incorporated with external circuit elements, for calculation of loop current and its effect on the arc channel evolution. These calculation methodologies and results obtained thereby are narrated in chapter 3 in detail.

For validation of the simulation results obtained in chapter 3, experimental setups are developed. Two different experimental setups are developed for experiments. Small experimental setup is designed for low voltage operation and can handle gas pressure up to 5 kg/cm^2. Detailed description of this experimental setup is given in chapter 4. Methods of experimentally measuring sparkgap inductance and validating the same with simulation results are narrated in chapter 5. For high pressure, high voltage experiments another experimental set up have been developed. This setup can go up to 1 MV and handle gas pressure up to 40 kg/cm^2. Details of this experimental setup are elaborated in chapter 6. Experimentally obtained results, experimental errors, method to derive arc channel inductance from the raw data and comparison of the same with simulation results are described in chapter 7 in detail.

An attempt has been made to calculate and experimentally verify the behavior of arc channel with time and resulting inductances thereby, in this thesis. Previously, significant work has been carried out in understanding plasma, its composition, thermal and electrical conductivity and other properties. Results of these studies are interpreted in the context of arc channel plasma, and thereby variations of arc channel inductance in a particular circuit. This study and its validation thereafter, in this thesis, will pave path for design of sparkgap switches for high voltage low inductance applications i.e. Ultra Wide band systems in future.

Chapter 3
Simulation of spark gap inductance

High voltage sparkgap arc channels are studied worldwide over the years. It has lots of applications in different fields of pulsed power technology (both industrial & strategic). Till date sparkgaps are considered to be the most reliable, rugged and low cost switch for high voltage applications. Even though, this is widely used historically across the world, still the technology of sparkgap operation lacks complete understanding. Behavioral unpredictability, shot to shot variations and involved complicated physics inside the device operation makes understanding of the device very difficult. Till date, several empirical formulae and experimentally reported data are mostly used for design of sparkgaps. During firing of a sparkgap a thin arc channel is formed between two electrodes of a sparkgaps. Arc grows and changes its properties with time till its extinction. During this period arc channel resistance changes from very high value of several mega Ohms (almost open circuit) to very low (almost short circuit) of few mili-Ohms and current flowing through the arc channel also changes with time. The phenomenon of high voltage breakdown is reasonably explained using Townsend or streamer theory. But these theories do not enlighten about arc channels electrical and physical parameters like radius, inductance, current distribution and temperature distribution. In this research work, it has been attempted to numerically estimate these physical parameters of an arc channel during transient growth of arc.

3.1 Problem formulation

To formulate such complicated phenomena some definite solvable model of the whole process is required. For understanding growth of arc channel, a model has been suggested by A.Wells *etal* in the year of 1969 [37]. This comprehensive model is used for numerical calculation of the above phenomena. This model suggested that arc channel can be assumed as a collection of hollow cylindrical conducting channels. Conductivities of these channels are function of their temperature. With the initiation of arc channel (at some point on the electrode) a very thin cylindrical channel of current flows through the medium. Corresponding channel gets heated up due to Joule heating. Temperature of the channel goes up bringing down the resistivity of that channel further and increasing the current density. Temperature of the surrounding cylindrical channels also goes up due to thermal diffusion and so does the current density. Gradually arc channel spreads and naturally decides its own dimension or radius. Calculation of this whole process involves plasma physics, ionization of gases at high temperature, electrical & thermal conductivity of gas plasma and specific heat of gas molecules. In this project this phenomena has been attempted to simulate using numerical techniques assuming that sparkgap switch is being used for discharging a capacitor.

3.2 Assumptions in the simulation

Sparkgap arc channel model developed for estimation of arc channel inductance and current distribution, has following assumptions:

1. Sparkgap is assumed to have parallel plate configuration and arc channel is cylindrical in structure.

2. Gas medium is homogeneous and does not contain any impurity.
3. Temperature and pressure of the gas medium is uniform at the beginning of the simulation i.e. $t = 0$;
4. Pressure of the gas is constant throughout the simulation period.
5. Arc channel is uniform longitudinally and azimuthally. Only radial variation of temperature and plasma condition is considered.
6. Mobility of electrons are much higher than atoms and ions, hence it is assumed that electrons are only mobile particle in the plasma.
7. To find out plasma composition Saha's equation is used. This equation is best suited for steady state plasma. Here it is assumed that for a single time step of simulation, plasma is stable.
8. Convection loss is considered to be negligible. Only radiation loss is considered for calculation of temperature inside the arc channel.
9. Pulse forming line is considered as loss less one and sparkgap switch is assumed as an ideal switch with internal series inductance and resistance.
10. Load is assumed as ideal resistive load without any lead inductance. All the distributed lead inductance of the circuit is assumed as lumped inductance.

3.3 Description of the program code

The model of arc channel as suggested by A.Wells conceptualizes an arc channel as collection of hollow cylindrical conducting channels. Conductivity of these channels is function of temperature of those plasmas. To simulate this condition program is divided into four sub programs

i) Subprogram to calculate circuit voltage and current.

ii) Subprogram to calculate thermal distribution of the arc channel.

iii) Subprogram to calculate resistance of arc channel.

iv) Subprogram to calculate inductance of arc channel.

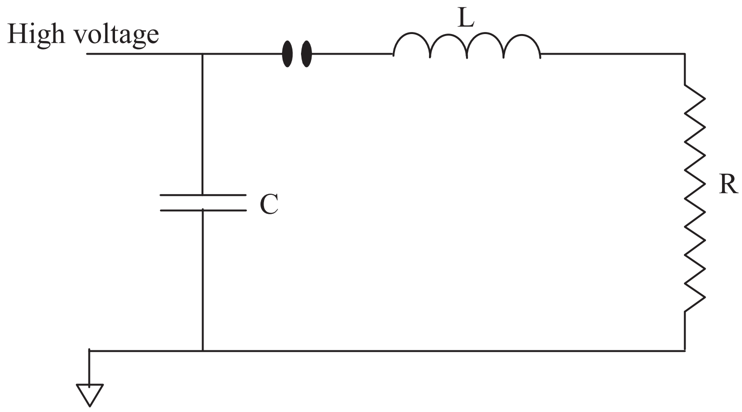

(a) Diagram of typical circuit arrangement used for simulation

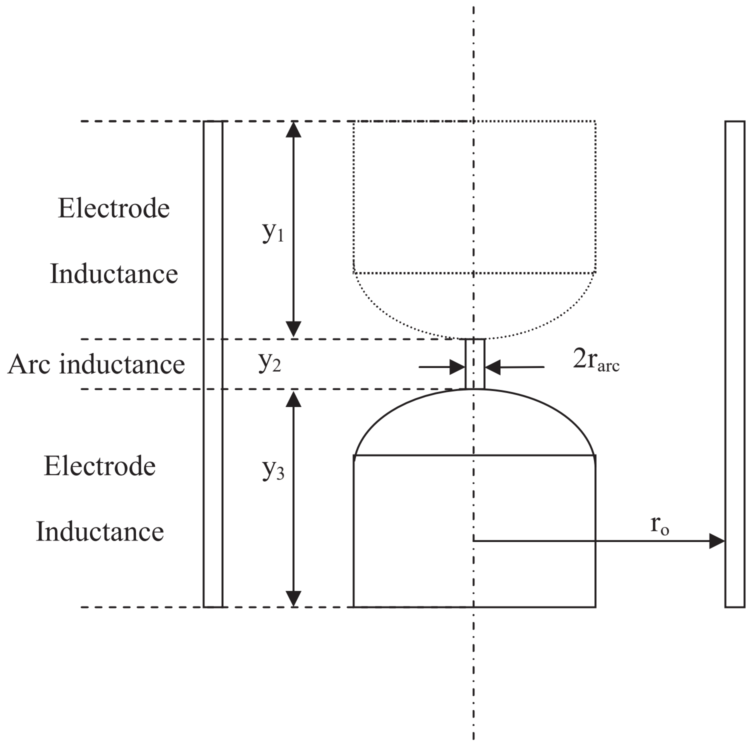

(b) Sparkgap switch inductance

Fig.3.1 Equivalent circuit diagram of capacitor discharge

Circuit shown in figure 3.1(a) describes the equivalent circuit diagram of the code. This circuit is composed of an energy storage capacitor, sparkgap switch and a load resistor. Sparkgap switch is assumed as an ideal switch with time varying resistance and inductance, connected in series to it. In this code, currents are calculated at every time step due to application of initial capacitor voltage at time = 0; voltage across the sparkgap, inductance and resistance parameters of the sparkgap are taken from other subprograms. All the calculations are carried out using Kirchhoffs' equation shown in equation number (3.1).

$$\int \frac{I.dt}{C} + (L + L_s)\frac{dI}{dt} + (R + R_s)I = V \quad (3.1)$$

Where, I is the current in the loop; V is the initial voltage in the capacitor; R is the loop resistance; R_s is resistance of sparkgap arc channel; L_s is inductance of the sparkgap arc channel.

With every time step increment in current is calculated in the circuits assuming all other parameters are constant at that small instant of time.

In experiments described in following section pulse forming lines are used in place of a lumped capacitor. In practice when a capacitor discharges as a pulse forming line transient equations are different than that of lumped assumptions of capacitor. To understand behavior of the switch during discharge from pulse forming line different equations are used. Instead of charged capacitor an ideal square pulse with source impedance of Z_0 (characteristic impedance of pulse forming line) is assumed and equations are modified as follows

$$(L + L_s)\frac{dI}{dt} + (R + R_s + Z_0)I = V \quad \text{for} \quad 0 < t < \tau$$

$$(L + L_s)\frac{dI}{dt} + (R + R_s + Z_0)I = 0 \quad \text{for otherwise} \tag{3.2}$$

Where, Z_0 is the characteristics impedance of the pulse forming line.

Second sub program calculates temperature and conductivity of the arc channel. Arc channel is assumed as collection of *'n'* number of coaxial hollow cylinders (these coaxial hollow cylindrical sub unit of arc channels are called kernels). Current flowing through these kernels is an input from first sub program.

Heat generated in each kernel rises the temperature of the kernel and that of adjoining kernels. To find out temperature rise in different kernels thermal diffusion equation is used. It is assumed that heat energy transfers by thermal conductivity of the gas plasma. Temperature rise in the kernel is calculated by mass of the gas in the kernel and specific heat of the gas plasma at the constant pressure. Equation (3.3) is used for calculation of rise of temperature of the arc channel kernels.

The code written has three main parts i.e. circuit simulating part, arc channel thermal calculation part and arc channel resistance, inductance and current distribution calculation part. Circuit simulation part calculates voltage and current of the circuit at each small interval *'dt'* assuming resistance and inductance of the system remains constant for that small period of time. Then thermal calculation part calculates the change in temperature in each element during the smallest elemental period and calculates new temperature distribution. A look up table correlates temperature with plasma conductivity of certain gas plasma and the third part of the program finds out new current distribution, equivalent resistance and equivalent inductance of arc channel to offer. The process iterates for the whole span of period for which simulation has to be done. Circuit diagram and equations involved are shown below.

$$\sigma(T)E^2 - \ mC_p(\frac{dT}{dt}) + \frac{d\left(rK(T)\frac{dT}{dr}\right)}{rdr} = 0 \qquad (3.3)$$

Where, *σ(T)* = electrical conductivity of plasma at temperature *T; K(T)* = thermal conductivity of plasma at temperature *T*; r is radius of arc channel; C_p = specific heat of gas plasma at pressure P*;* *E* = electric field inside arc channel.

In this equation the first term represents the amount of energy deposited into a kernel, second term defines the change in temperature due to heating and the third term represents heat energy conduction to adjacent kernels. Using this equation temperature distribution of the arc channel can be estimated at any instant of time. It should be noted that only one dimensional variation is considered for carrying out solutions assuming radial and axial symmetry in the arc channel.

In this equation electrical conductivity and thermal conductivity of gas plasma used for calculation. These values are function of temperature. Standard tables for these values of many gases are available. However calculation of the same also can be done using plasma equations [50]. At a certain temperature composition of plasma can be calculated using Saha equation [49].

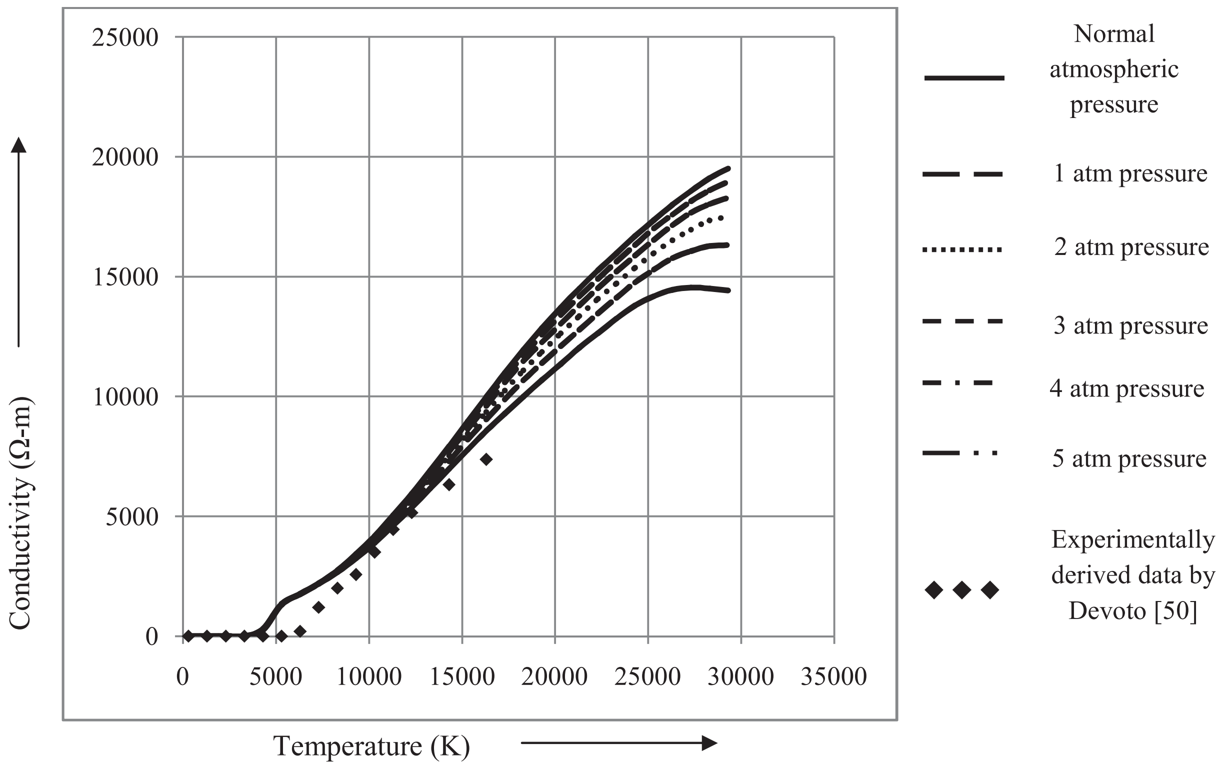

Fig.3.2 Conductivity of nitrogen gas at different pressure with temperature

Transport matrix equation and Chapman Enskog equation [50] can be used to find out conductivity of any gas plasma at a particular temperature. However, these values are mostly suitable assuming stable plasma condition. In figure (3.2) electrical conductivity of N_2 gas plasma at different temperature is plotted. These are calculated values and matches reasonably with reported literature data. However for gases like SF_6 calculations are much complicated. Hence for calculation, published literature data are used.

After calculation of temperature and conductivity of arc channel kernels equivalent resistances is calculated using equation (3.4).

$$R_s = {[\int i(n)^2 R_{arc}(n).dr]}/{I^2} \qquad (3.4)$$

Where, R_s is equivalent sparkgap resistance; I is the loop current; $R_{arc}(n)$ = Resistance of n^{th} arc channel kernel. $i(n)$ is current through n^{th} arc channel kernel.

In this equation numerator represents the total heat energy deposited in the arc channel and denominator represents square of the total current. Assuming that equal amount of active energy would have been consumed if the combination of resistances of arc channel kernels is replaced by single sparkgap resistance of value R_s.

Similar calculations for finding equivalent inductance of the arc channel are also carried out. But in this case calculations are little more complicated because of mutual coupling. Hence to address this issue, again energy equivalence concept is used. Here it may be mentioned that using energy equivalence concept for finding equivalent circuit parameters is easier as it involves calculation of scalar parameters only.

For calculation of inductance of each arc channel kernel, total flux encircling the arc channel kernel is calculated. This flux is summation of all the flux created by all the arc channel kernels simultaneously. Change in flux is calculated in each time step and by dividing the same with change in current in n^{th} arc channel kernel, inductance is calculated. Equation (3.5) represents the same in mathematical form.

$$L_{arc}(n) = \frac{d[\sum \Phi_{mn}]}{di(n)} \qquad (3.5)$$

Where, $L_{arc}(n)$ is the inductance of nth arc channel kernel; Φ_{mn} is flux produced by m^{th} arc channel kernel enclosed by n^{th} arc channel.

To calculate equivalent inductance total magnetically stored energy is used. As it is known that $0.5LI^2$ is equal to the total magnetically stored energy, hence both are equated to find out equivalent inductance of the arc channel using formula in equation (3.6).

$$\frac{1}{2}L_s I^2 = \frac{1}{2\mu_0}\int (\sum B_m(n))^2[2\pi r(n)l].dr \qquad (3.6)$$

Where, $r(n)$ is radius of n^{th} arc channel kernel, $B_m(n)$ is magnetic flux density at $r(n)$ radius created by current flowing through m^{th} arc channel kernel.

Calculated inductance is returned back to first subprogram for next time step calculations.

Here it is important to mention that better accuracy in calculations can be achieved with smaller time step and higher number of arc channel kernels. However, smaller step size in time and space increases simulation time. Moreover it is important to mention that too many coupled complicated equations often has tendency to diverge and become unstable. Hence, it requires some trial and error in getting stable comprehensive results. However, these simulations are found to work reliably in the domain of interest. Never the less, computer consumes lot of memory in executing these programs.

Flow chart of the program is shown below for ease of understanding. Program begins with the first block i.e. "Start calculation with first lead of electrons bridge the electrode gap at $t = 0$". Then in the second block it calculates temperature rise in the arc channel kernel and its adjacent kernels; for this calculation it goes to a subprogram and returns to the main program with results (shown with bidirectional arrows).

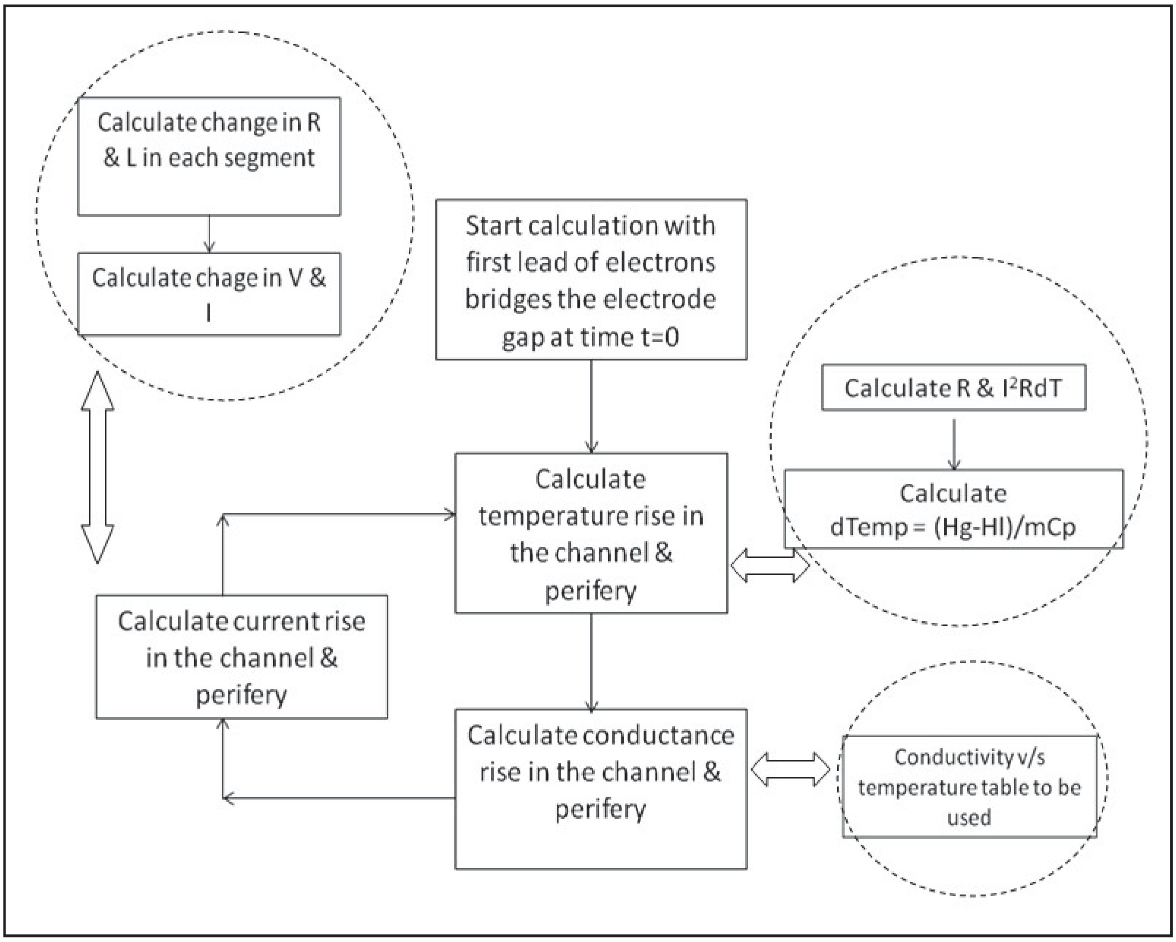

Fig.3.3 Flow chart for calculation of time varying arc channel characteristics

Then in the third block it calculates change in conductance of the arc channel kernels via preset data table. Then in the fourth block arc channel resistance and inductance is calculated through another subprogram. After calculating voltage and current in the circuit this sequence is repeated with increased time step.

Most significant of obtained simulated data are voltage across the capacitor, current through the sparkgap, resistance of the sparkgap and inductance of the sparkgap. Current density inside the arc channel also can be found in the simulation. These time varying data are plotted below in the table as a typical example solution. It is interesting to find that arc channel radius varies significantly with change in pressure of the gas. In figure 3.4, results of two simulations are compared for their arc channel radius. It is found that arc channel radius at 1 kg/cm^2 is much thicker than that of 5 kg/cm^2. Correspondingly their inductance values are also significantly different. Importance of those results will be discussed in the course of the thesis in following chapters.

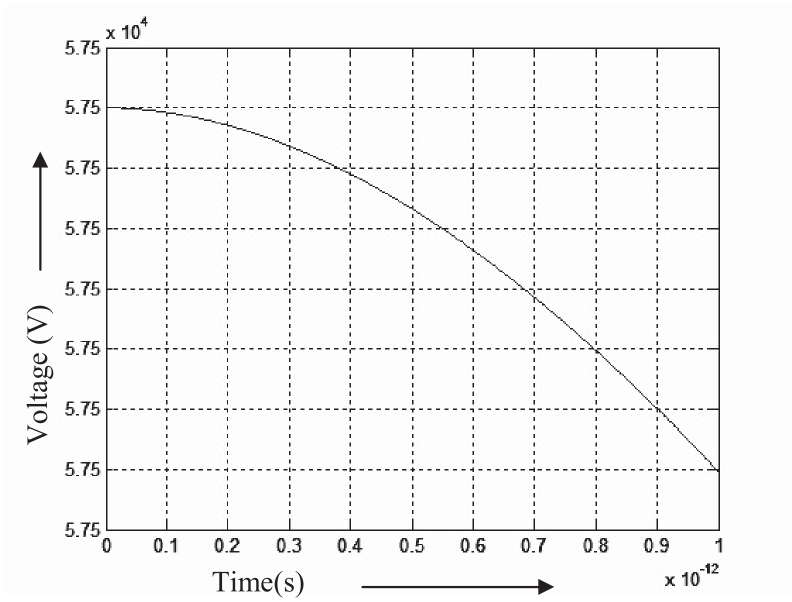

Fig. 3.4(a) Voltage across the capacitor

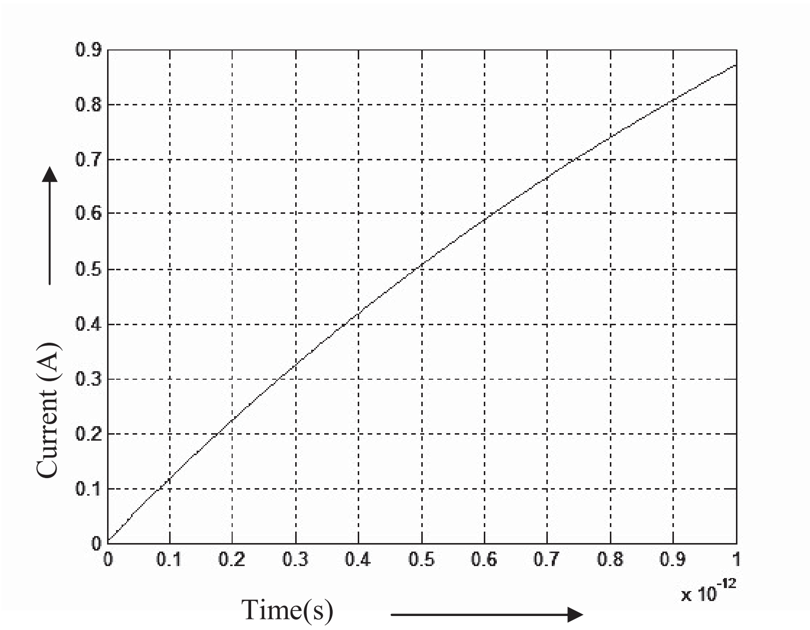

Fig. 3.4(b) Current through the circuit (I)

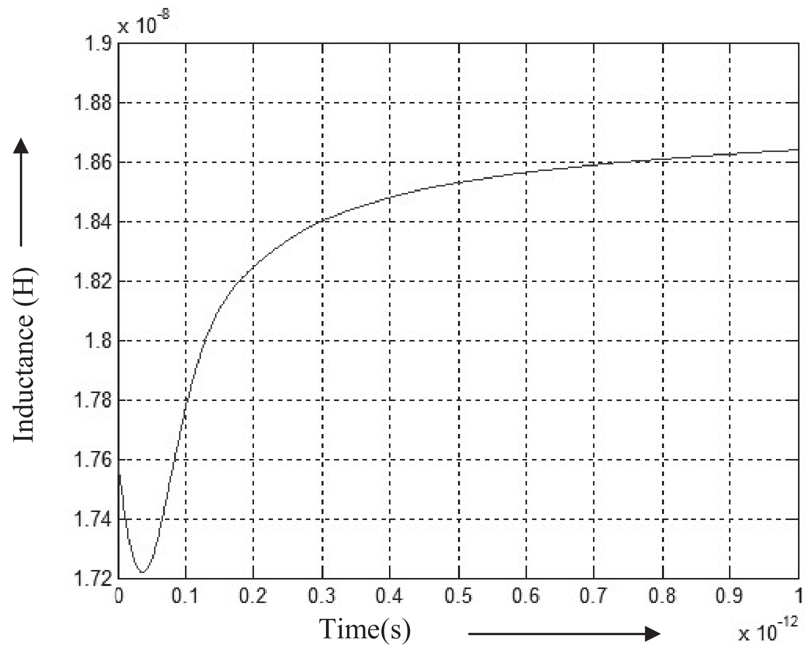

Fig. 3.4(c) Inductance of sparkgap

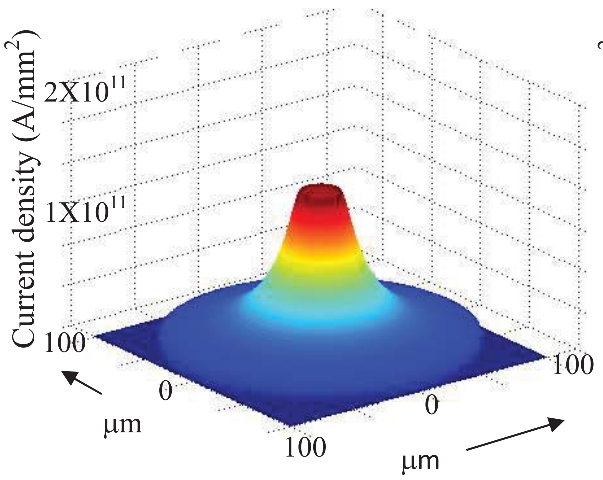

Fig. 3.4(d) Arc channel with 1 atm pressure

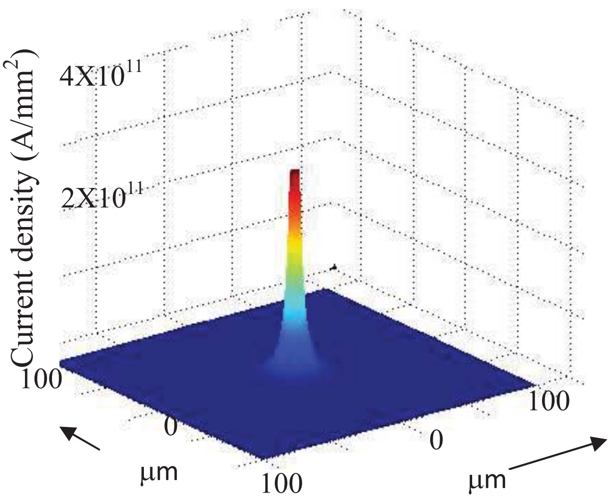

Fig. 3.4(e) Arc channel with 5 atm pressure

3.4 Results and discussion

Results shown in figure 3.4 are typical output of the program displayed after post processing. In figure 3.4 (a) voltage of the energy storage capacitor is shown. With onset sparkgap switch, voltage of the capacitor reduces and energy gets transferred to load. Figure 3.4(b) shows a typical current waveform. Current flowing through the sparkgap arc channel increases with time depending on the external circuit parameters and parameters of the sparkgap. Figure 3.4 (c) shows inductance of the arc channel spark gap. Here it should be mentioned that simulation result of 1 pico second is only shown in these screens. In figure 3.4 (d) and 3.4 (e), current density distribution of spark gap arc channel is shown. As mentioned previously, this simulation assumes axial and azimuthal symmetry. For ease of visualization, current profile has been plotted in 3-D using a post processing program. It can be noticed in the figure 3.4 (d) and 3.4 (e) that radius of arc channel is different in both the cases. Arc channel in case of 1 kg/cm^2 nitrogen pressure is shown in figure 3.4 (d) whereas in figure 3.4 (e) arc channel is exhibited for 5 kg/cm^2 atmospheric pressure. It is observed that arc channel diameter gets thinner with increase in gas pressure. As a consequence of that, difference in inductance of arc channel is also observed with increase in pressure. Detailed study of variation of arc channel inductance with pressure of gas is discussed in following chapters. It is also observed that arc channel diameter depends on the type of gas used. With variation of gas medium the very nature of plasma with temperature becomes different. As a consequence of that, arc channel radius is observed to be different for different gases. In lighter gases i.e. nitrogen argon etc. formation of conducting plasma takes place easily, hence larger arc channel diameter is observed. Whereas in case of heavier gas molecules i.e. SF_6 etc. growth of arc plasma is slow and arc channel is much thinner. This causes different gas medium arc channels to exhibit different inductances under similar condition.

As the simulation repeats with time steps, many time varying data are also available as output. It is difficult to appreciate them without proper post processing. Growth of arc channel with time is one of such data of extreme importance. It is observed that, with time arc channel grows in radius and amplitude. Results depicting growth of arc channel with time is displayed in figure 3.5. Figure 3.5(a) shows the arc channel after 10 ps, figure 3.5(b) shows arc channel after 50 ps and figure 3.5(c) shows arc channel after 90 ps. It can be observed that diameter of arc channel increases with time. Here it should be noted that inductance of an arc channel is a logarithmic function of its diameter. Hence, change in arc channel diameter does not increase or decrease inductance in equal proportion. However, with increase of arc channel diameter inductance reduces and vice versa. This simulation gives an interesting insight of the arc channel behavior during firing of sparkgap switches. This simulation is based on a certain model and elaborates behavior of arc channel dynamically with time. It exhibits behavioral differences inside arc channel while the medium, geometry or physical parameters like pressure and temperature of sparkgap is altered. These interesting phenomena and results obtained from this simulation provide definitive directions (i.e. for design of high voltage low inductance sparkgap switches, high pressure operation is more preferred compared to increase in gap between electrodes) in design of sparkgaps for critical applications of ultra wide band system.

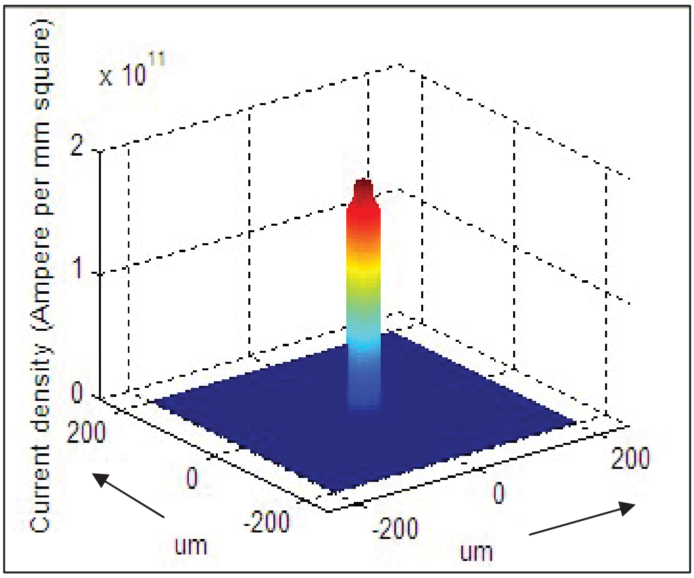

Fig. 3.5 (a) Arc channel after 10 pico second

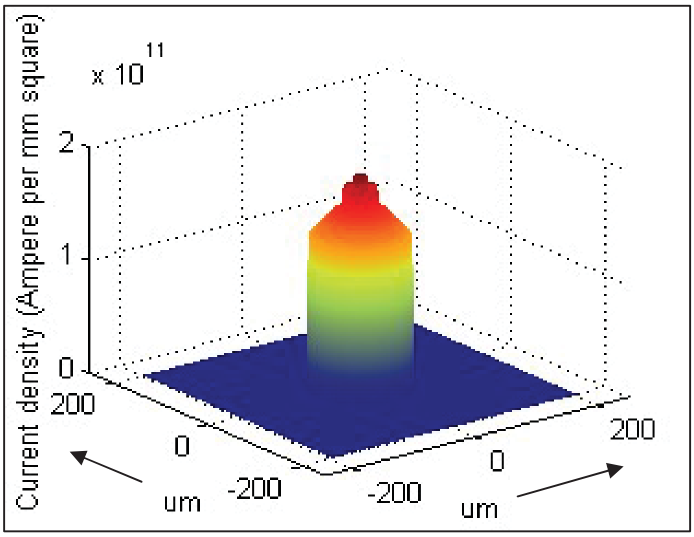

Fig. 3.5 (b) Arc channel after 50 pico second

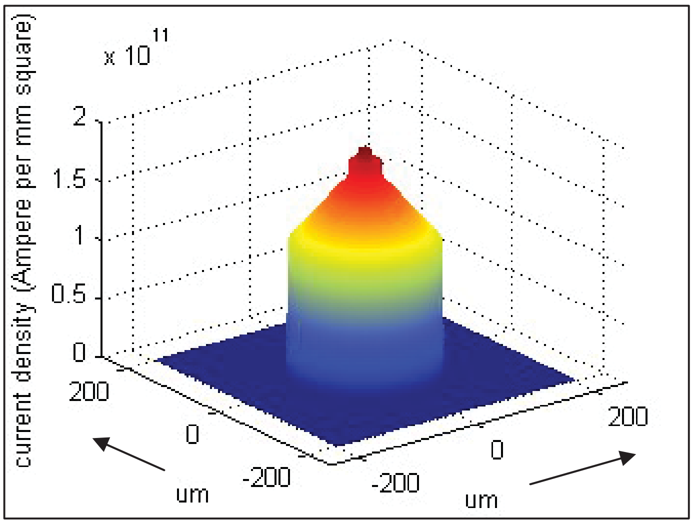

Fig. 3.5 (c) 90 pico second of commencement

3.5 Simulation of V-I characteristics

Voltage across the arc channel and current flowing through the arc channels are calculated and plotted against each other. It is found that voltage across the arc channel is not monotonous with increase in current. Rather simulation results shows that initially with increase in current voltage increase gradually up to a limit then starts decaying slowly. After a certain point voltage again rises up and then suddenly collapses drastically. Initial rising part in figure 3.7 indicates increase in voltage and initiation of Townsend breakdown. Following part of the curve is known as normal glow discharge region. In this region plasma is feeble due to low current and in contact with only a small part of cathode surface. In this region voltage and current are relatively independent to each other. With increase in current, contact surface of plasma and electrode increases and finally plasma covers the entire electrode. This region is known as abnormal glow discharge region. In this region voltage increases significantly with increase in total current.

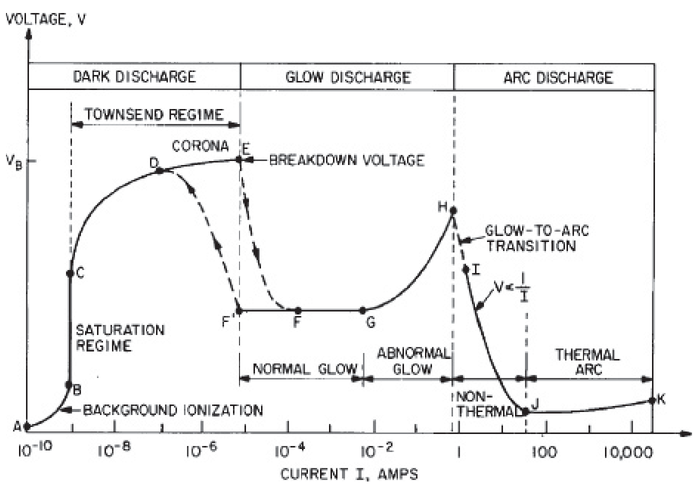

Fig. 3.6. Regimes of the classical DC electrical discharge [61]

Finally at a certain point, arc plasma becomes sufficiently hot and cumulative ionization and increase in current density initiates causing fast collapse of voltage.

This is known as arc discharge. Obtained V-I profile for normal atmospheric pressure nitrogen gas is shown below. This curve significantly matches with well known V-I characteristics of gas discharge shown in figure 3.6 [61]. Different zones are also identified from their trend. This is an attempt to explain the transient gas discharge phenomena using a single model based on thermodynamic condition of gas plasma. This profile shows the versatility of the code developed for study of the arc channel inductance of sparkgap. Different studies can be carried out using this same code and validating the same experimentally. In this thesis basic attention has been given to inductance of arc channel, simulation, measurement and validation of the same. Details of the experimental studies and comparison of the same with simulated results are narrated in following chapters.

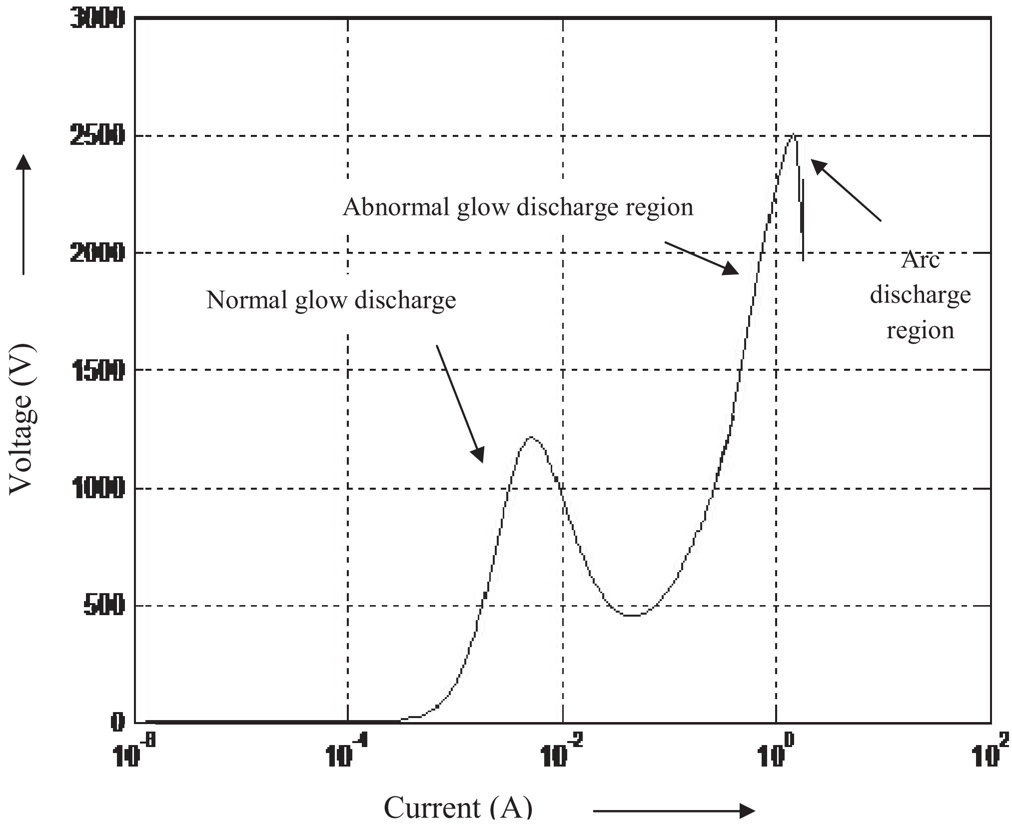

Fig. 3.7. Simulated V-I characteristics of nitrogen arc channel showing different discharge region

3.6 Runaway electrons and ionization waves

It has been reported in literature, that at the nanosecond breakdown of different gases at atmospheric pressure and above, runaway electrons are generated, which produce X-ray radiation while decelerated in a gas at the anode [53]. The runaway electrons are generated, when an anode cathode gap is subjected to high voltage pulse of extreme fast rise time (< 1 ns). The mechanism of generating the runaway electrons in gas-filled gaps depends on the experimental conditions. Cathode surfaces, though usually mirror polished, still consists of lot of micro-projections on its surface. As high voltage is applied across the gap huge field enhancement takes place at the tip of these micro-projections. Due to the field enhancement of the cathode and cathode holder surface, field emission from the cathode at the leading edge of the voltage pulse is observed. Moreover, plasma is formed at the surface of the cathode (usually contains vaporized cathode materials and adsorbed gases in the cathode). These electrons gain acceleration under the high electric field present across the gap. Moving away from the sharp points of cathode fast electrons lose their energy mainly due to collision with particles in the gas gap region. As a result, ionization of gas molecules and further multiplication of electrons take place. Secondary and field-emission electrons initiate the development of electron avalanches. As the concentration of electrons increased a streamer is formed and a relatively dense plasma front produced near the cathode, starts moving from the cathode to the anode. As the plasma grows, the gap between the plasma front and the anode becomes smaller. This results in increase of effective electric field in the gap and a critical field E_{cr} is attained for initiation of runaway mode. The value of E_{cr}, can be estimated by using $\alpha(E_{cr}, p)d = 1$ criterion, where α is the first Townsend coefficient, p is the gas pressure and d is the inter-electrode gap. However, this criterion was obtained for the gaps with a uniform electric field and small initial energies of electrons. With an increase in the initial electron energy, electrons move to the run-away mode at lower E_{cr} field values [54]. Electron energy increases with time both due to higher voltage in the gap (as voltage pulse has a fast rise time, voltage increases with time) and because of the effect of field enhancement caused by travel of ionization wave. The cathode plasma front moves from the cathode to the anode simultaneously with the beam electrons. Part of the energy of runaway electrons cause ionization in the gap and ensures forward movement of the ionization wave. The restriction in electron beam pulse duration occurs due to the gap between anode and cathode is bridged with the ionization wave causing equalization of the electric field in the gas gap. The formation of a streamer initiates from the formation of electron avalanches. When the field strength of the space charge in an avalanche becomes comparable with the strength of the external field in the gap, a streamer is formed. The runaway electrons move towards the anode faster and hence, they cannot produce initial electrons in front of the cathode-directed streamer. However, when runaway electrons are decelerated in a gas, they generate X-ray radiation, which produces sufficient initial electrons in the gap to sustain the streamer. Thus, during discharges of sub-nanosecond time order, movement of the ionization wave front and of the streamer to the anode is caused by the runaway electrons. They are accelerated due to the concentration of the electric field at the dense plasma boundary. The movement of the ionization wave and the streamer towards the cathode is caused by enhancement of the electric field at the boundary of the dense plasma. Ionization of this region is caused by X-ray radiation generated when the runaway electrons slows down in the gas medium.

Most preferred conditions for generation of runaway electrons are as follows [55]:

1. High-voltage pulses with the maximum possible amplitude should be applied to the gap at the time moment of Supershort Avalanche Electron Beam (SAEB) generation.
2. The gas diode should have low inductance, smooth inner walls, and a stepless transition to a flat anode.
3. A stainless-steel foil of thickness 50–100 μm should be used to fabricate the cathode. The foil should be rolled up into a tube. Mostly used cathodes are of 6-10 mm diameter.
4. The beam current can be also increased at the expense of lower wave impedance of the gas diode and a larger cathode area.

Role of runaway electron in the present analysis

In the present set of analysis and study of sparkgap arc channel, emphasis has been given to growth of arc channel. Simulation code starts at the onset of streamer and continues to calculate arc channel current distribution and inductance with time. This spark gap switch under consideration supposedly connects pulse forming line to load (copper sulphate load or antenna load) and not a load itself. Charging of pulse forming line from MARX generator takes about 50 ns time span in the present experimental set up. Spark gap switch, connected at the end of pulse forming line, experiences the same voltage across its gaps. Significant runaway electrons are caused by non uniform E-field of rise time less than a nanosecond, applied across a gas gap. The phenomena of electron beam and allied ionization boundary gets over by few hundreds of Pico second. In this thesis, as the gap under scrutiny, experiences a comparatively slow rise time of 50 ns, hence generation of runaway electron beam will be significantly lower. Never the less, this will create some initial pre-ionization before the streamer formation. As soon as streamer formation takes place, high electrical field across the gas gap will seize to exist and any further ramification of runaway electrons will be extremely insignificant. In this thesis, work has been carried out to find the growth of this streamer with time. No calculations or measurement prior to that is carried out. However, initial conditions assumed for calculation may get affected by presence of runaway electron and ionization boundary just before the onset of streamer. But, the degree and amplitude of such an effect seems extremely small and difficult to quantitatively estimate to the accuracy of simulation and experimentation available to us. In future, efforts may be given in understanding the effect of runaway electrons and pre-ionization in arc channel current distribution and inductance calculation.

3.7 Conclusion

In this chapter detailed discussion on the simulation code is carried out. This code has four main sub programs and a post processing module. These subprograms are written to calculate current and voltage at different nodes of the circuit, thermal and electrical conductivity distribution inside arc channel kernels, resistance of the arc channel and inductance of the arc channel. Post processing module elaborates the obtained results in desired formats. Typical results obtained from this simulation code are described in this chapter. Voltage, current and inductance change with time is shown in figures. Arc channel current distribution is plotted for different gas pressures and varied time to understand their implications. However, this code has its own limitations in calculating the extreme nonlinear coupled conditions. Step sizes required for successful converging is extremely small i.e. in the range of femto seconds. The program takes huge simulation time to simulate for even fraction of a nanosecond. Some nonlinear parameters like thermal conductivity of gas plasma are assumed to be constant at all temperature in this program, in practice it is a function of temperature. Radiation loss of heat energy is not considered in the simulation, though it may be considerable at higher arc channel temperature. These are the issues which may to be addressed to fine tune the program in future and experiments need to be conducted to calibrate and validate the code rigorously.

Chapter 4
Development of 200 kV experimental set up

In this chapter detailed description of the experimental set up and method to measure sparkgap inductance is narrated. Development of experimental set up plays a very crucial role in experimentation, collection of data, analysis of data and validation of simulation model described earlier in chapter 3. In this context it must be noted that expected inductance of arc channel is in the range of tens of nano-Henry. Hence extreme care needs to be taken in order to measure it. All the required measures are taken to minimize errors in measurement. Details of the experimental set up and methodology of measurement are narrated in this chapter. The setup consists of high voltage power supply, MARX generator to charge PFL capacitor, pulse forming line assembly; trigger supply for MARX generator, measuring instruments like voltage divider and copper sulphate dummy load. MARX generator and pulse forming line assembly needs gas pressurization for rated voltage operation. All the systems required for developing the experimental set up, except 30 kV DC power supply, are designed and fabricated in house. Divider calibrations are conducted with best engineering practices to acquire most reliable data during experiments. Details of all the components and experimental methodologies are described below.

4.1 **Description of the Experimental system**

Experimental system is mainly composed of three distinct components i.e. MARX generator, pulse forming line and load cum divider assembly as shown in figure 4.1. 30 kV high voltage DC power supply is used for charging of the MARX generator. MARX generator upon erection generates maximum of 250 kV voltage pulse to charge the pulse forming line. This pulse forming line discharges into a dummy matched copper sulphate load of 60 Ω through the sparkgap under test. 125 kV, 5 ns voltage pulse is obtained across the load and measured using specially designed divider assembly. Rise time of this voltage pulse is measured to calculate inductance of the sparkgap. Detailed description of each components of the experimental setup is given below.

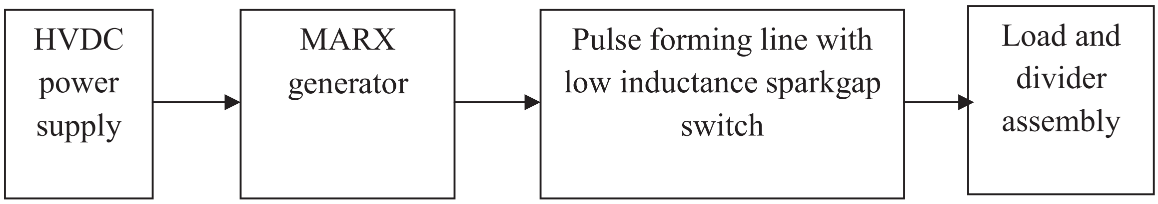

Fig.4.1(a) Block diagram of experimental setup for measurement of sparkgap inductance

4.1.1 High Voltage power supply

Any capacitor charging power supply capable of delivering 30 kV to a capacitance of 35 nF can be used for the purpose of charging the MARX generator. Standard off the shelf power supply made by M/S Spellman is used in this experiment. Depending on the current rating of the power supply charging time of the system varies. For single shot experiments low current rating power supplies (up to 50 mA) can be used suitably.

4.1.2 MARX generator

This is a seven stage unipolar MARX generator. Each stage is composed of four 1.2 nF, 30 kV ceramic capacitor. All the stages are coaxially arranged to achieve low inductance while erecting. These ceramic capacitors are having a disk with metal fitting type electrode used for ultra high voltage applications. They are epoxy-

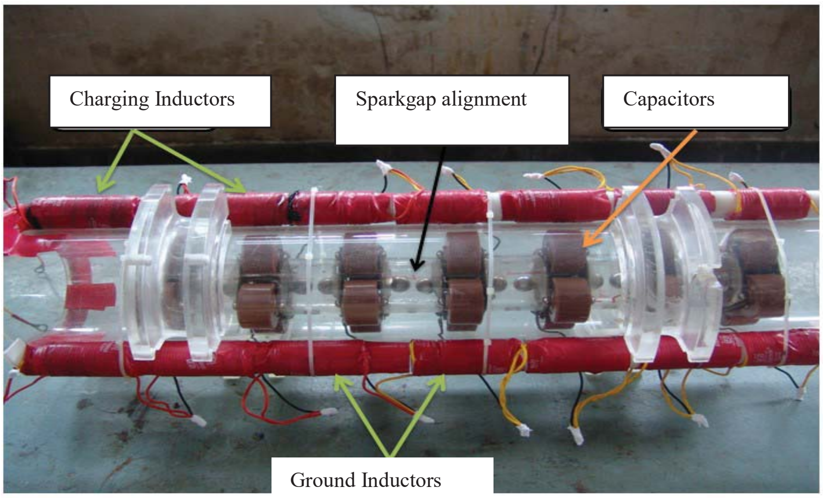

Fig.4.1(b) Photograph of MARX generator

encapsulated and use strontium titanate as dielectric material. The diameter and length of the capacitor is 38 mm and 26 mm respectively. In each stage 4 capacitors connected in parallel between two copper plates which will hold them together. Other sides of the copper plates are fitted with hemispherical electrodes of 15 mm diameter. While placed in sequence, these SS made electrodes form interstage sparkgap switches. Total eight numbers of spark gap switches all with an increasing gap distance from 5 mm to 7 mm for first spark gap to 8th spark gap respectively are used. Gaps between electrodes are adjusted by varying position of the capacitor modules. Whole assembly is placed inside a hollow Perspex cylinder and arranged so that sparkgap switches and capacitors are coaxially placed with respect to the enclosing SS cylinder. The charging and discharging inductors are of solenoid types. Each stage uses 8 μH charging and ground inductors for charging of MARX generators. The total Marx generator is enclosed in a metallic chamber made by stainless steel which provides a return path for the discharge current. While operated at normal atmospheric pressure, MARX generator charges up to 12 kV and charges the pulse forming line to 120 kV upon erection. Output of the MARX generator can be controlled by varying N_2 pressure up to 1 Kg/cm^2.At 0.5 Kg/cm^2 pressure MARX generator erects at a charging voltage of 25 kV and charges the Pulse forming line to 250 kV voltage in 50 ns. The whole MARX structure is mounted on a movable trolley for ease of mobility. Size of the MARX generator is about 750mm and it weighs nearly 15 kg.

This MARX generator is fabricated assembled and tested separately before connecting to the experimental set up. For testing of the MARX generator a copper sulphate load of known impedance is used. MARX generator is charged upto 12 kV and discharged into the load. A detail of this experiment is narrated in following sections of this chapter.

4.1.3 Trigger supply

A trigger supply has been developed for controlled triggering of MARX generator. It is an optically controlled, solid state based trigger supply and capable of generating 20 kV, 200 ns pulse suitably required for triggering of MARX generator. The trigger supply is composed of a solid state switch BSM300GA120D IGBT (Eupec) and TS136B Pulse Transformer (Perkin Elmer, EG&G). A 0.25 μF, 1 kV energy storage capacitor is charged to 600 V through a bridge rectifier. IGBT switch is used to discharge the capacitor into the primary of pulse transformer. Here it must be mentioned that the specific IGBT mentioned here has a turn on time of 30-40 ns. This is a very important parameter for proper operation of the trigger supply. If the turn on time is higher, sufficient energy of the capacitor gets dissipated in the IGBT. If triggered suitably, capacitor discharges energy into transformer primary and a high voltage pulse is correspondingly generated at the secondary of the pulse transformer. Leakage inductance of the pulse transformer decides the rise time of the voltage pulse and current through the IGBT switch. Pulse transformer should be suitably selected based on its core cross sectional area, so as to avoid core saturation during operation. A Diode L33F250 (Siemens) is used for freewheeling the current through the primary coil to protect the IGBT from reverse biasing. Figure 4.2 shows Circuit diagram of the assembly.

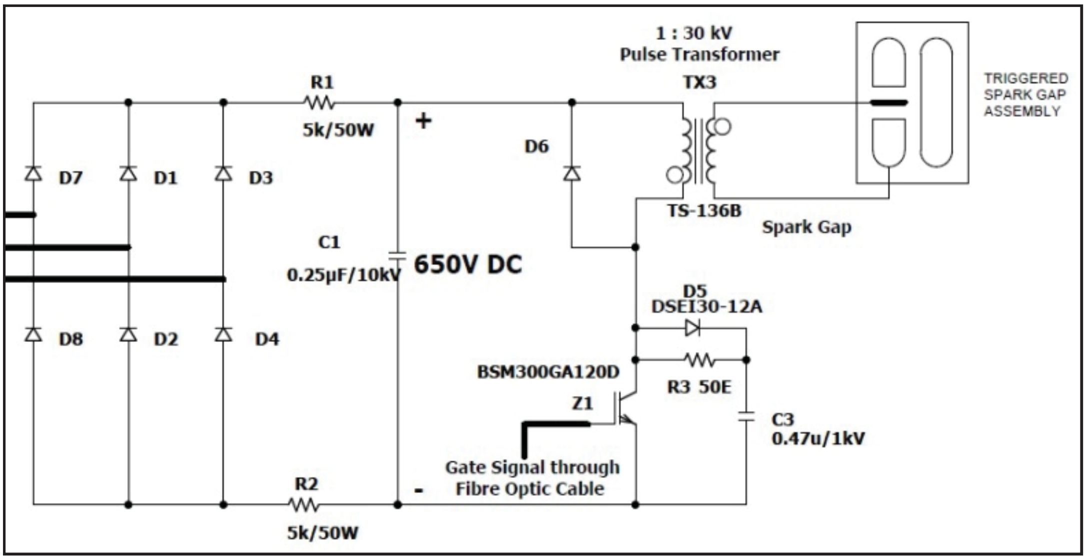

Fig.4.2 Circuit diagram showing IGBT based trigger supply

Fig.4.3 Trigger assembly with handheld controller unit

Upon firing, a 20 kV pulse is obtained at the secondary of the pulse transformer. The pulse transformer is a 1:30 step up pulse transformer and requires capacitive isolation from the triggered electrode of the MARX generator. Moreover, core of the pulse transformer must be grounded suitably to avoid damage of IGBT during erection of MARX generator. The voltage required for triggering the spark-gap at the trigger terminal is 6 – 8 kV in air, the system is designed to supply maximum of 20 kV, 200 ns pulse. For safety of the personal it is good practice to have optical interface between operators and trigger supply. Hence, trigger control unit is designed to get actuated via optical signal and optical signal is generated using a hand held battery powered unit. Photograph of the trigger generator is shown in figure 4.3. Upon triggering the hand held unit an optical signal of 1 μs reaches the controller and generates trigger signal for IGBT. IGBT upon firing generates trigger pulse of 20 kV, 200 ns which trigger the MARX generator to charge pulse forming line to 250 kV. A measured typical trigger pulse is shown in figure 4.4.

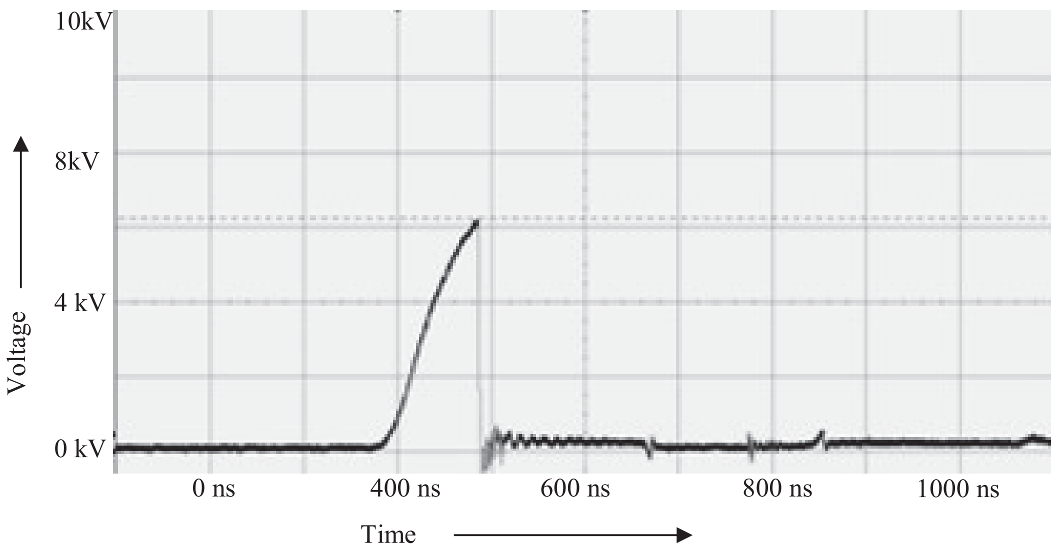

Fig. 4.4. Measured triggering voltage waveform at first spark gap

4.1.4 Pulse forming line

Pulse forming line is a coaxial transmission line. If charged to a voltage V and discharged using a very fast switch into a matched load, it can generate a square pulse of V/2 amplitude across the load. This coaxial transmission line can be modelled as infinitely long L-C-L pi network as shown in figure 4.5. Initially all the capacitors are charged to voltage V and then the switch is closed at time $t = 0$;

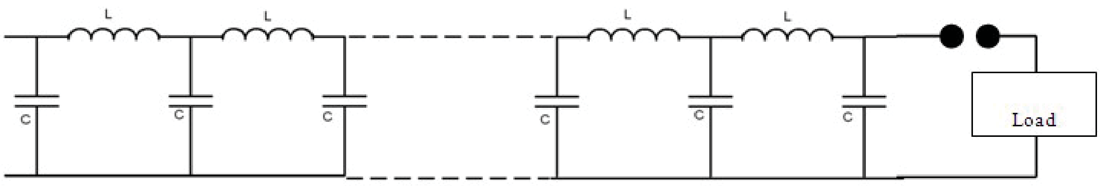

Fig.4.5 Typical equivalent circuit diagram of Pulse forming Line with final switch and antenna load

This circuit is analysed by assuming a DC voltage source of amplitude V is discharged into load impedance of Z_L through internal impedance of Z_{OC}. Where Z_{OC} is defined as input impedance of the line with load is at open circuit.

For infinite transmission line input impedance is defined as

$$Z_i = Z_0 \left[\frac{\frac{Z_r}{Z_0} + \text{ta} \quad (\gamma l)}{1 + \frac{Z_r}{Z_0} \tanh(\gamma l)} \right] \qquad 4.1$$

Where Z_r is the impedance connected at the receiving end, Z_0 is the characteristic impedance of the transmission line, l is length of the line and $\gamma = j\omega\checkmark(LC)$ in loss less transmission line.

Hence, Thevenin's equivalent impedance of this transmission line can be calculated as

$$Z_{OC} = \lim_{Z_r \to \infty} Z_i \qquad 4.2$$

Hence, it can be written using equation (4.1) and (4.2) that

$$Z_{OC} = Z_0 \left[\frac{\frac{1}{Z_0}}{\frac{1}{Z_0} \tanh(\gamma l)} \right] = Z_0 \coth(\gamma l) \qquad 4.3$$

If the circuit in figure 4.6 is solved in Laplace domain using equation (4.3) we can get that

$$V_L(s) = \frac{V}{s} \left(\frac{Z_L}{Z_L + Z_{OC}} \right) = \frac{V}{s} \left(\frac{Z_L}{Z_L + Z_0 \coth(s\delta)} \right) \qquad 4.4$$

Here it can be noted that Z_{OC} can be represented as Z_0 coth(sδ) in frequency domain. Where, δ is defined as travelling time of the wave front from one end of the transmission line to other. In other words δ is defined as the ratio of length of the transmission line to wave propagation velocity.

After certain mathematical manipulations it can be shown that

$$V_L(s) = \frac{V[1 - e^{-2s\delta}]}{s(1 + \frac{Z_0}{Z_L})} [1 - \left(\frac{Z_0 - Z_L}{Z_0 + Z_L} \right) e^{-2s\delta} + \left(\frac{Z_0 - Z_L}{Z_0 + Z_L} \right)^2 e^{-4s\delta} - \cdots] \qquad 4.5$$

Therefore, if load impedance is equal to the characteristics impedance of the line, it can be written that

$$V_L(s) = \frac{V[1 - e^{-2s\delta}]}{2s} \qquad 4.6$$

If converted to time domain we get

$$V_L(t) = \frac{V}{2}[1 - u(t - 2\delta)] \quad 4.7$$

Hence, if a pulse forming line is discharged into a matched load through a fast acting sparkgap switch, a square voltage pulse is obtained. Pulse width of this pulse is double the transit time of the wave front in the line and amplitude is half of charging voltage of the line.

Using this principle, pulse forming line based experimental setup has been developed. For making the pulse shaper two coaxial SS-304L cylinders are used. Perspex support is used for maintaining the gap between them and providing mechanical support. Cylinders are connected with gas filling arrangements and capable of handling up to 10 kg/cm^2 pressure. It is compatible with N_2, Ar and SF_6 chemically. Outer diameter of the inner cylinder is 60 mm and inner diameter of the outer cylinder is 180 mm. these two coaxial conductors constitute a transmission line. Length of the cylinder is approximately 600 mm. Hence, upon firing 5 ns pulse can be generated. Load cum divider assembly is connected to one of the side flange of the cylindrical line. Gap between inner cylinder and load assembly forms the sparkgap under test. This gap can be manually adjusted for experimental purpose. This assembly is fitted with voltage divider for measurement of charging voltage pulse.

4.2 Voltage divider

A copper sulphate voltage divider is designed and fabricated for measurement of charging of pulse forming line from MARX generator. Photograph of the divider is shown below in figure 4.6. This divider has two resistances connected in series. High value resistance is of 1 kΩ impedance and made up of aqua solution of copper sulphate. Low value resistance is of 1 Ω and made up of 10 numbers of 10 Ω quarter watt carbon resistors. Voltage across the low value resistor is tapped using a 50 Ω resistor and measured using RG58 cable and oscilloscope with 50 Ω terminations. Calibration of the voltage divider is carried out against standard voltage dividers applying low voltage pulse of 15 kV, 100 ns. Calibration factor of the divider is found to be 1:2000.

Fig 4.6 photograph of PFL divider

4.3 Load-cum divider assembly

In designing an extremely fast responding voltage divider, the challenge is in the reduction of inductance of the resistive components of the divider. A liquid resistor fundamentally serves this purpose of inductance reduction. In standard electrolytic voltage dividers, this is done using copper sulphate, sodium chloride, or potassium chloride solutions. These types of dividers are good for the measurement of high voltage pulses having rise times of few nanoseconds. In these types of voltage dividers, *R1* (the high side resistor of the divider) is usually made of electrolytes whereas *R2* (the low side resistor of the divider) is made up of small carbon resistors. When measuring a high voltage pulse having sub-nanosecond rise time, all the resistors should have low inductance and hence need to be made of electrolytic solutions. For suitable measurement of high voltage pulses, *R1* should be about a kilo Ohm whereas *R2* should be few Ohms. A 50 Ω reflection dampener should also be in place to avoid any reflection from the 50 Ω coaxial line that carries the signal to measurement oscilloscope. The design has been done in a way that using same copper sulphate solution, all the three resistive components can be realized. The geometry of the structure is made so, that when filled with copper sulphate solution, all three resistors have required impedance and exhibit fast rise time. *R1* is measured as 250 Ω, *R2* is of 2 Ω, and reflection dampener is of 50 Ω. A coaxial load of 65 Ω is placed over the voltage divider as a dummy load to achieve 60 Ω matched impedance. Figure 4.7 shows equivalent circuit diagram of the divider assembly.

The load and divider assembly are combined in a single geometry to ensure coaxial arrangement of both the load and divider. This reduces lead inductances to the load and divider simultaneously. This divider is made up of three coaxial Perspex cylinders. Inner radius of the innermost cylinder is 7.5 mm. Outer radius of intermediate cylinder is 15mmand inner radius of outermost cylinder is 23 mm. Length of the assembly is 56 mm. A Perspex rod of 35 mm length and 7 mm radius is placed inside the inner most cylinder, such that one of the flat surfaces of the Perspex cylinder aligns with one flat surface of other Perspex cylinders. Another small Perspex hollow cylinder of outer radius 1.5 mm, inner radius 1 mm, and 10 mm length is placed coaxially aligning the other flat surface of the cylinders. A connector is placed at the end of this small cylinder to connect the divider with measurement port. Conducting metal flanges are connected on both the sides of the divider to contain liquid inside. Copper sulphate solution of suitable concentration is filled in the volume inside inner cylinder and region in between outer and intermediate cylinders. Whole assembly is sealed properly to avoid any leakage of the liquid. Ground is connected to the flange where measurement connector is connected. Other flange is connected with high voltage spark gap for measurement of voltage. Simulated and fabricated structure of the divider is shown in Figures 4.8 and 4.9 respectively.

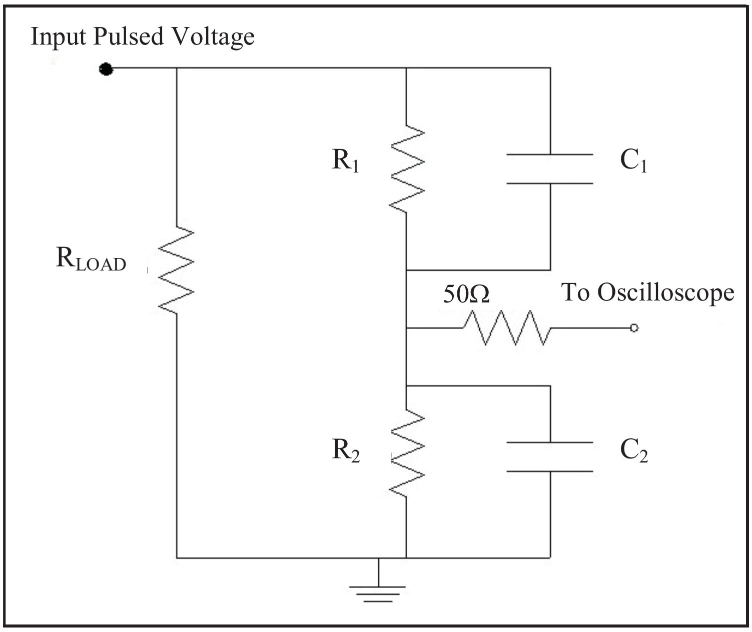

Figure 4.7. Equivalent circuit diagram of the divider assembly

4.4 SIMULATIONS AND ANALYSIS

The design of an extremely fast resistive divider made of liquid resistors is sensitive to frequency. Effects due to parasitic inductance and capacitance of the liquid resistor are negligible at low frequency. As the frequency increases, these effects become dominant and cause distortion in the pulse. Inductance of the liquid resistor can be reduced by increasing the diameter, but reducing the effect of capacitance is extremely difficult. Referring to figure 4.7, to nullify the effect of stray capacitances R_1C_1 must be equal to R_2C_2. It is extremely difficult to design and fabricate divider to match the required C_1 & C_2 value. It can be shown that RC time constant of any structure is equal to $\rho\varepsilon$, the product of electrical resistivity and permittivity of the material. Hence, if same liquid can be used for making all the resistors of the divider then this condition of $R_1C_1 = R_2C_2$ can be achieved. This will make the voltage divider less sensitive to frequency.

Measured voltage at oscilloscope V_m can be expressed as

$$V_m(s) = V(s)\frac{\left(\frac{R_2}{C_2 s}\right)\Big/\left(R_2+\frac{1}{C_2 s}\right)}{\left(\left(\frac{R_1}{C_1 s}\right)\Big/\left(R_1+\frac{1}{C_1 s}\right)\right)+\left(\left(\frac{R_2}{C_2 s}\right)\Big/\left(R_2+\frac{1}{C_2 s}\right)\right)} =$$

$$V(s)\frac{\left(\frac{R_2}{C_2 s}\right)\left(R_1+\frac{1}{C_1 s}\right)}{\left(\left(\frac{R_1}{C_1 s}\right)\left(R_2+\frac{1}{C_2 s}\right)\right)+\left(\left(\frac{R_2}{C_2 s}\right)\left(R_1+\frac{1}{C_1 s}\right)\right)} \tag{4.8}$$

Multiplying numerator and denominator by $s^2C_1 C_2$ we get

$$V_m(s) = V(s)\frac{R_2(R_1C_1s+1)}{R_1(R_2C_2s+1)+R_2(R_1C_1s+1)} \tag{4.9}$$

Hence, if $R_1C_1 = R_2C_2$;

$$V_m(s) = V(s)\frac{R_2}{R_1+R_2} \tag{4.10}$$

From equation (4.10) it can be seen that the measured voltage becomes independent of parasitic capacitance, and the sensitivity of the divider becomes frequency independent. In practice it is extremely difficult to reach this condition at high frequencies. But attempts to achieve this condition ensure lesser variation of sensitivity with increase in frequency.

Any liquid resistor made of aqua solution of chemicals like copper sulphate, sodium chloride, potassium chloride etc. can be made in many shapes and sizes. Shape of the container determines the shape of the resistor. Problems arise in calculating the stray capacitances of non standard resistor shapes. To avoid this problem an innovative approach has been developed. As stated earlier, the effect of these stray capacitances can be nullified if $R_1C_1 = R_2C_2$. It can be shown that RC time constant of any material (in this case copper sulphate solution) is equal to $\rho\varepsilon$. Where, ρ is resistivity of the material and ε is the permittivity of the material. This is true for any shape or size of the resistor provided that ρ and ε of the medium remains constant for the region of interest. While the resistivity and permittivity of any aqua solution does not remain perfectly constant, the variation of these parameters is generally negligible for the present purpose.

Hence, if a single solution of copper sulphate is used to fabricate R_1 & R_2 of the divider, then we can achieve a condition $R_1C_1 = R_2C_2 = \rho\varepsilon$, as ρ & ε are property of the solution and have no geometrical influence, hence this can be achieved. This condition is used in designing and fabricating the copper sulphate divider to facilitate the measurement of high voltage pulses of subnanosecond rise time and nanosecond pulse widths.

To study the performance of this structure with pulsed voltages, a simulation was carried out in CST microwave studio. The actual scenario of calibration is simulated in the software i.e. discharge of a matched PFL (Pulse forming Line) is simulated across the divider assembly.

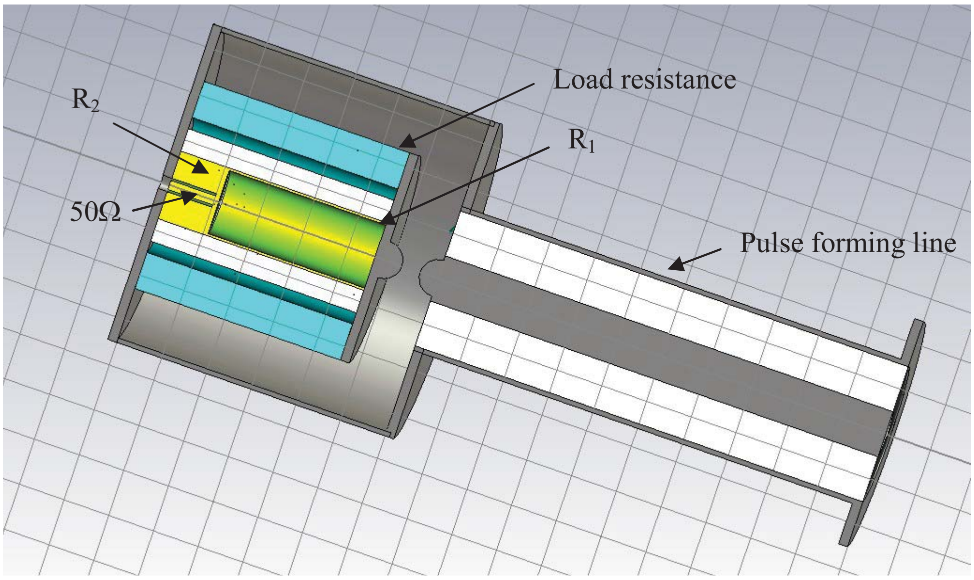

Fig. 4.8 Simulated structure of load cum divider assembly with matched PFL(raster is 10 mm X 10 mm)

The exact structural dimensions and physical parameters, including conductivity and permittivity of the liquid are given as input parameters to the simulation.PFL is charged to V voltage as an initial input and switch is closed at $t = 15\ ns$. On discharge, the PFL generates a square pulse across the load. The voltage that appears across the load and across the output port of the simulated divider is shown in figure 4.10 figure 4.11. These waveforms, shown in the figures, match with each other considering their profiles i.e FWHM (full width half maxima) and rise time.

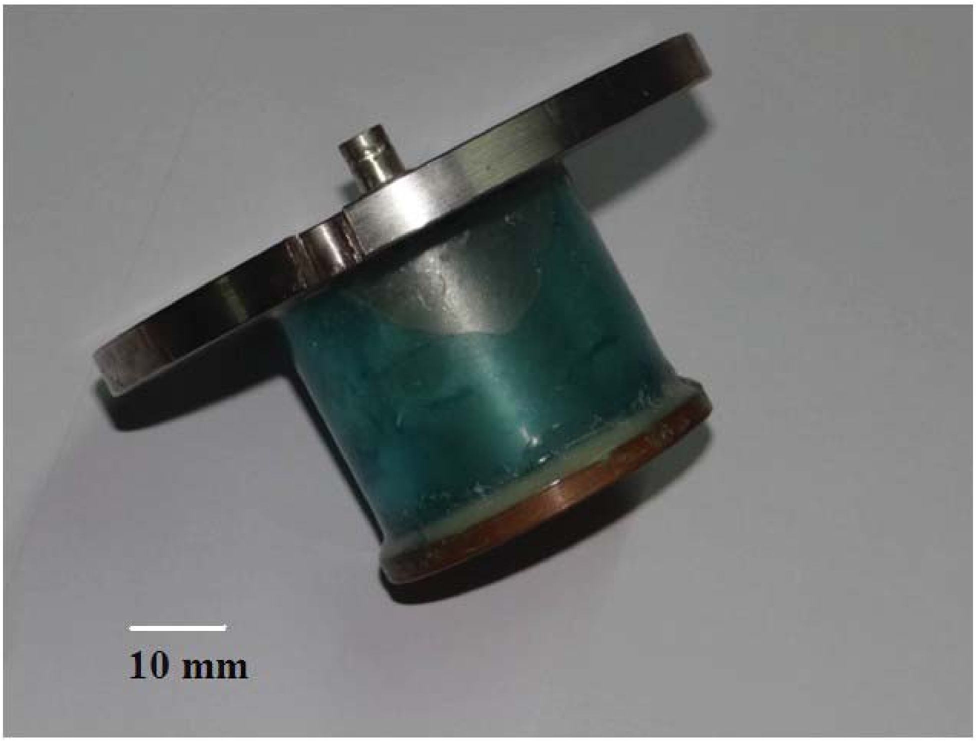

Fig. 4.9 Fabricated structure of load cum divider assembly. (white line indicates 10 mm length)

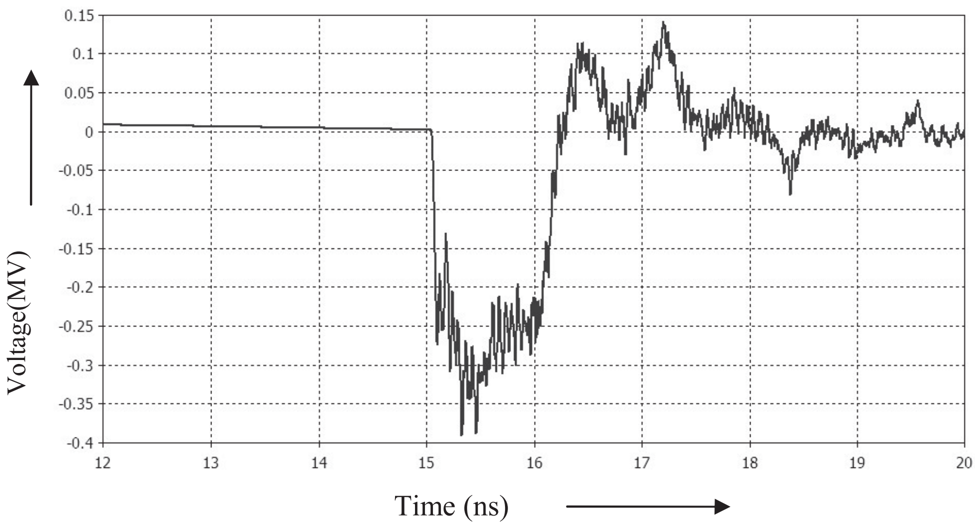

Fig. 4.10 Simulated voltage pulse feed across divider

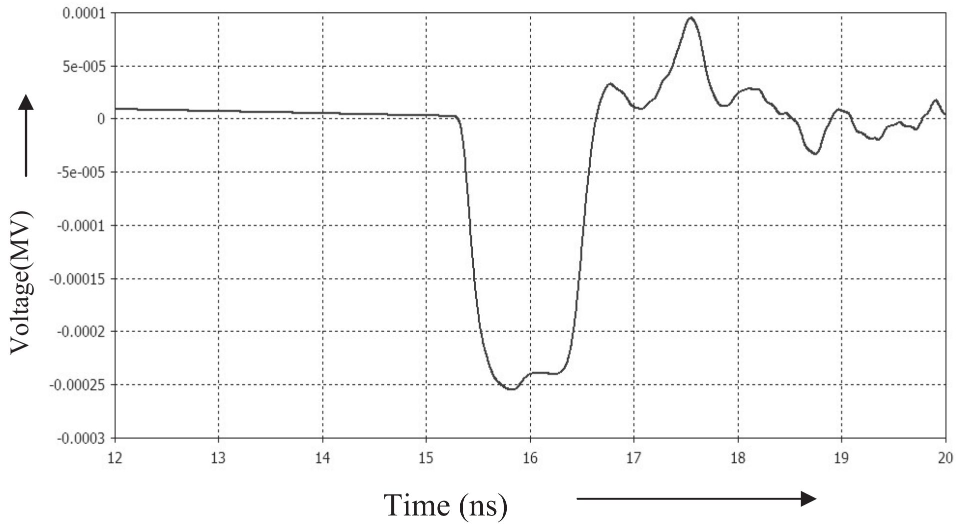

Fig. 4.11 Simulated voltage pulse at output of divider

4.5 RESULTS AND CALIBRATION

A calibration procedure has been designed to study performance of the divider. Calibration of the divider assembly is extremely important for practical use and reliability. Calibration was carried out by discharging a matched Pulse forming line (PFL) into the load assembly. Under perfect matched conditions the divider would measure half the charging voltage as peak of the square pulse output. Hence, if the PFL is charged to V voltage (DC), then on discharge, the output should be a square pulse of amplitude V/2. The pulse width of the output pulse is determined by length of the PFL. This experimental set up was developed for calibration of the divider assembly. The schematic of the calibration set up is shown in figure 4.12. The PFL is charged to 10 kV and then discharged into the divider assembly. The divider output is measured using high frequency (6 GHz) oscilloscope with 50 Ω termination. A typical recorded waveform is shown in figure 4.13. Same experiment was repeated four times to avoid effect of random errors in calibration. Readings were taken for charging voltage of 10 kV to 30 kV. Results are plotted in figure 4.14. The best fit trend line is shown to determine the calibration factor, which was found to be 258:1. The statistical variation in measurement and margin of errors in the reading are calculated and shown below.

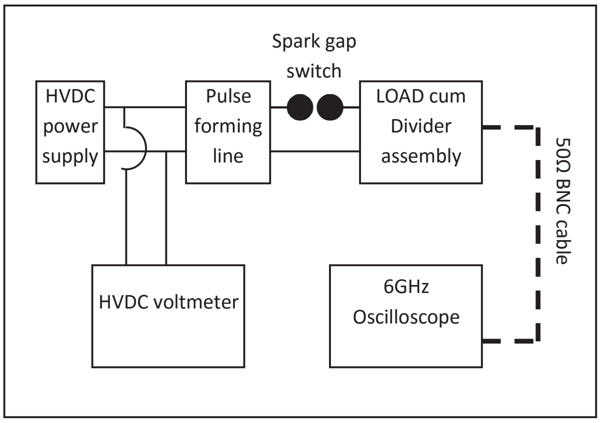

Fig.4.12 Schematic of calibration set up

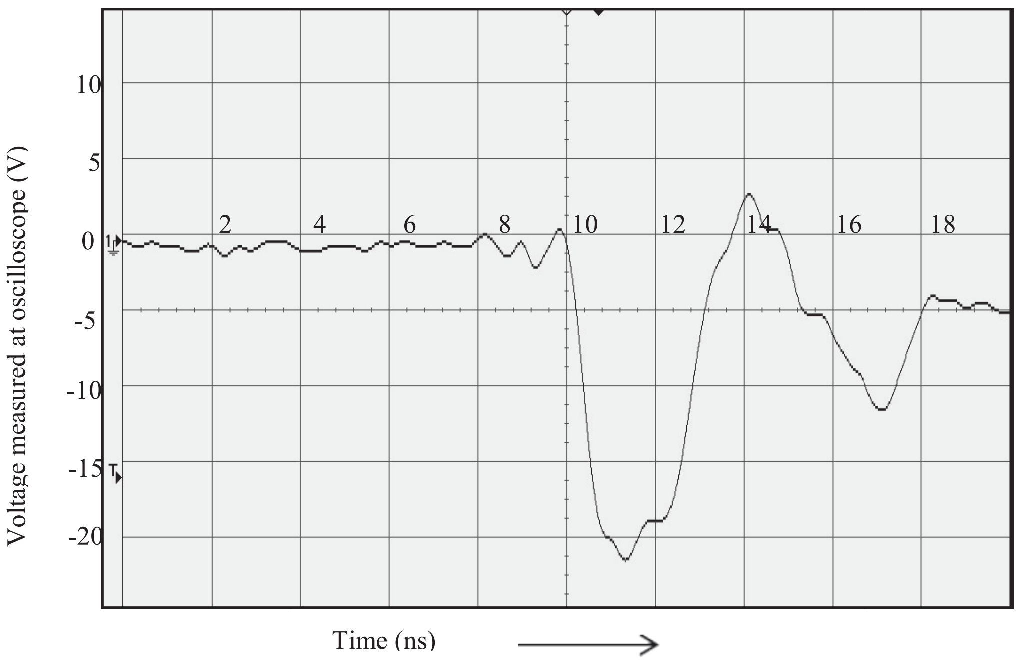

Fig.4.13 Typical calibration waveform showing 5ns square pulse

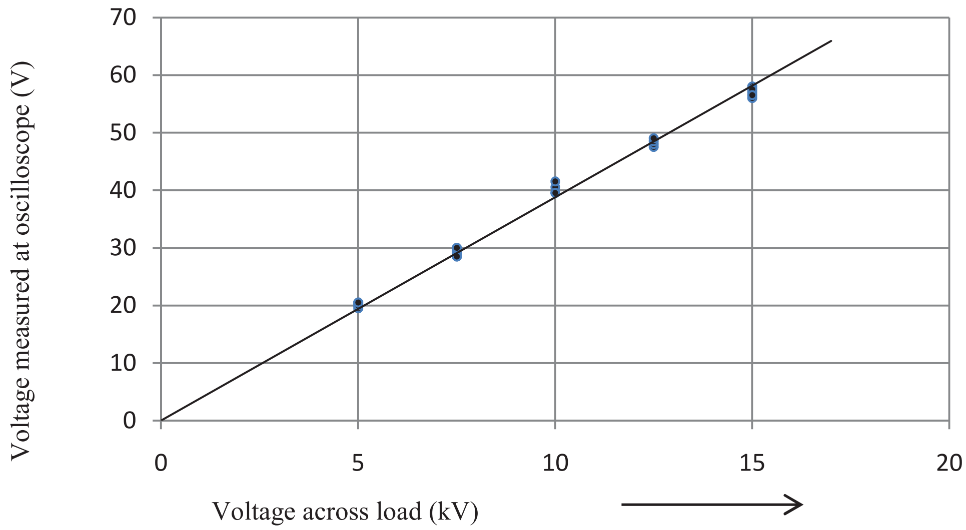

Fig 4.14. Divider calibration data

Fitting equation is $y = mx$ (4.11)

y = measured voltage peak in oscilloscope (Volts); x = expected load voltage across load (kV) = half of PFL charging voltage (kV)

$$m = \frac{\sum x_i y_i}{\sum (x_i)^2} \tag{4.12}$$

$$S_R = \sum (y_i - m x_i)^2$$

(4.15)

$$S_D = \sum (y_i - \bar{y})^2 \tag{4.13}$$

$$R^2 = 1 - \frac{S_R}{S_D} = 0.993 \tag{4.14}$$

Common standard deviation of error

$$S_e^2 = [n \sum y_i^2 - \{\sum y_i\}^2 \ ] - n\, m^2 [n \sum x_i^2 - \{\sum x_i\}^2] \tag{4.15}$$

Standard deviation of error in slope (m)

$$S_m^2 = {S_e^2}\Big/{[n \sum x_i^2 - \{\sum x_i\}^2]} = .214 \tag{4.16}$$

t-statistics for ±10% margin of error is

$$T_m = \frac{0.15m}{\sqrt{\left({S_m^2}\big/{(n-d)}\right)}} = 1.8 \tag{4.17}$$

n = number of data points; d = degrees of freedom; Hence, probability of the calibration factor being within ±10% is defined as

$$\Pr\{-1.8 < T_m < 1.8\} = 91.63\% \tag{4.18}$$

This statistical analysis numerically elaborates repeatability and degree of confidence in the developed instrument mentioned in this literature.

4.6 CIRCUIT SIMULATION OF EXPERIMENTAL SET UP

Electrical equivalent circuit of the subcomponents of the experimental setup is simulated using standard softwares. All the spark gap switches are assumed to be ideal switches with capacitance of 10 pF before closing. Inductance of 20 nH has been placed in series to get results close to reality. In this context it should be mentioned that the approximate values of sparkgap inductance is calculated by analyzing the waveform obtained by erecting MARX generator and discharging it across a copper sulphate load. For UWB applications, compact size of pulse forming line and low inductance of final discharge switch is extremely important. A fast

MARX generator ensures fast application of voltage pulse at pulse forming line. Hence higher field withstanding can be ensured even with smaller diameter. To ensure the same, MARX generator has been designed for charging of pulse forming line within 50-60 ns. This is mostly dominated by the erected inductance of the MARX generator. To estimate erected inductance, MARX generator is tested using copper sulphate load. Estimated inductance from the experimented waveform is used for simulation of the same. Simulated waveform is shown below in figure 4.15. In this context it is important to note that further faster pulse will have tendency to generate larger prepulse at the output of pulse forming line. Amplitude of prepulse will be higher with antenna load compared to that of copper sulphate resistive load. Hence 50-60 ns charging time is reasonably optimized duration for charging of pulse forming line of 5 ns discharge length.

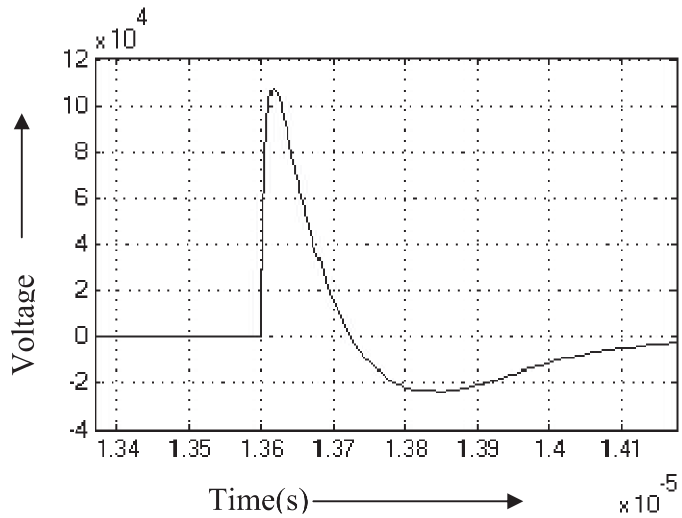

Fig.4.15 Simulated voltage wave form of UWB MARX generator

4.7 ELECTROMAGNETIC FIELD SIMULATION

To analyze the performance of pulse shaper during discharge, simulation is done using dynamic field simulation software. This software uses geometry of the construction to calculate transient behavior of the electrical circuit instead of using lumped parameter circuit simulations. Circuit simulating softwares work on the principle of lumped parameter analysis. As mentioned in the earlier sections, that discharge of a pulse shaper works as a transmission line in the designed frequency range hence, lumped parameter analysis is not sufficient enough to capture its performance. Dynamic field simulating softwares can handle such problems more accurately taking stray capacitance and lead inductances into account. After discharge, pulse forming line is supposed to generate rise time of about 100 ps. Hence, the frequency of discharge pulse will contain approximately up to 1.5GHz frequency ($f = .35/t_r$). This frequency wave will have wave lengths of approximately 0.2 m ($\lambda = c/f$). As standard practice, if geometry of a structure is less than $\lambda/10$ (in some case $\lambda/4$ is used for approximate calculations), lumped element model can work reasonably well. As our transmission line structure is much larger compared to wavelength of discharge pulse, dynamic field simulation softwares are more suitable. In figure 4.16 Geometry of the pulse shaper is shown and figure 4.17 shows the expected output waveform at the dummy load.

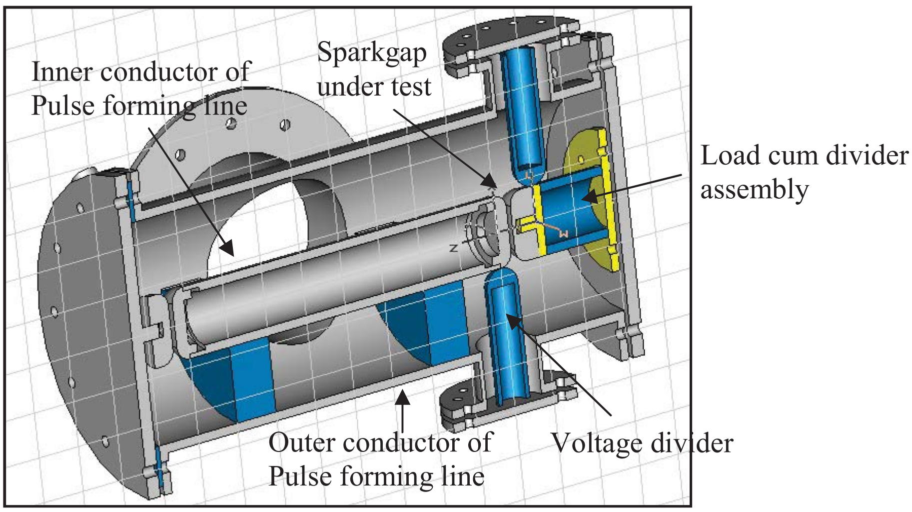

Fig.4.16 structure of experimental pulse forming line

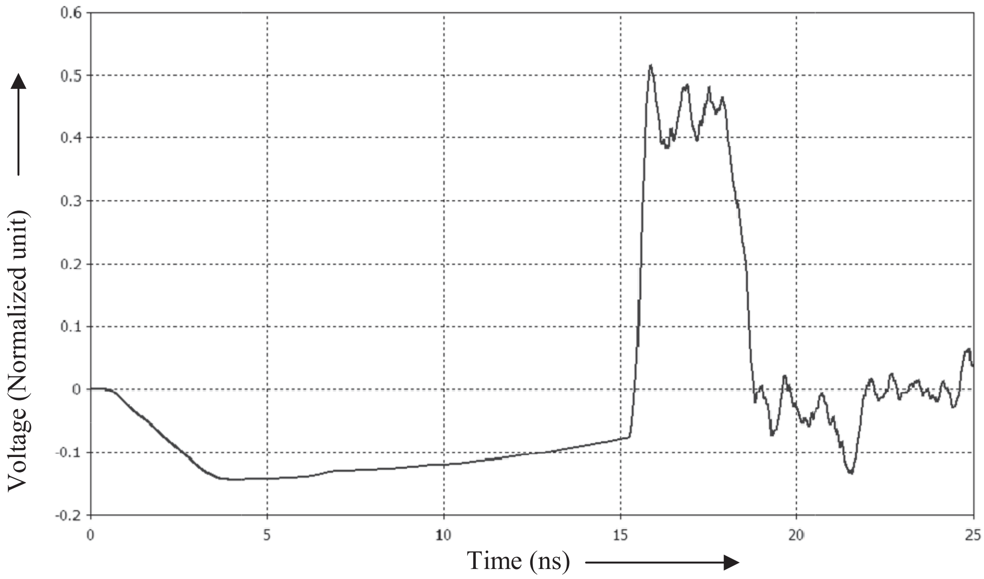

Fig.4.17 Simulated result of pulse forming line output

4.8 EXPERIMENTAL RESULTS

Experimental setup is prepared depending on simulations and subjected to tests before conducting the actual experiments for measurement of arc channel inductances MARX generator is charged up to 12 kV and discharged into a copper sulphate load. A high voltage pulse of approximately 50 kV is observed across 100 Ω $CuSO_4$ load. A high voltage probe HV-P60 having range DC-60kV, 2000:1, 1000 MΩ resistance is used to measure the output pulse voltage. The output pulse is shown in figure 4.18. Erection of MARX generator is found to be reliable. Voltage multiplication factor was as anticipated and rise time of the pulse was reasonably good. Output waveform matched the previously simulated waveform quite closely and connected to pulse forming line for further testing. This experiment was for testing of the developed MARX generator. Results exhibit that MARX generator was performing as desired.

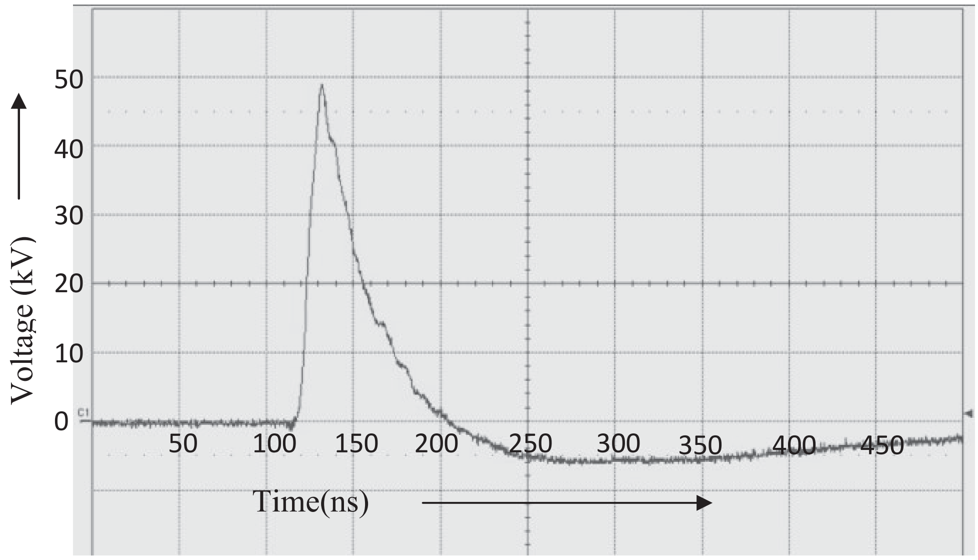

Fig.4.18 50kV MARX output voltage across copper sulphate load

Pulse shaper has a lower capacitance than erected capacitance of MARX generator hence while charging the pulse shaper resonant charging will take place. In resonant charging of dissimilar capacitors over voltage charging is observed. Here it should be mentioned that erected MARX generator capacitance is approximately 685 pF, whereas capacitance of the pulse forming line is approximately 40 pF. As a result of which while charging PFL gets charged to little higher voltage according to equation (4.22).

$$V_{PFL} = \frac{V_M C_M (1+\cos\omega t)}{(C_M + C_{PFL})} \qquad 4.22$$

Where,

V_M is open circuit voltage of MARX generator;

C_M is erected capacitance of MARX generator;

C_{PFL} is capacitance of pulse forming line;

ω is defined as resonant frequency of charging. It is function of equivalent capacitance and loop inductance of the circuit.

However in practice little less voltage is observed than calculated analytically. This is due to presence of stray capacitance of the MARX generator. But for low energy MARX this stray capacitance is comparable to other capacitances i.e. MARX capacitance and PFL capacitance. Hence over volting effect is found to be little less than double.

4.9 Experimental results with copper sulphate load

Initial Experiments are conducted at normal atmospheric pressure to check the performance of the experimental set up. Whole experimental set up is composed of high voltage power supply, MARX generator, pulse forming line, voltage divider, sparkgap under test and load cum divider assembly. Sparkgap under test and load cum divider assembly is placed inside the pulse forming line chamber as an integral part of it. Trigger generator is used to trigger the MARX generator. Photograph of the whole set up is shown below in figure 4.19. MARX generator is charged to 12 kV and erected. Charging of Pulse Forming Line is measured using copper sulphate voltage divider. Charging of PFL to 100 kV in approximately 70ns is recorded in 1GHz Agilent oscilloscope. Waveform is shown in figure 4.19. After 70 ns sparkgap under test self fire to discharge the pulse forming line into coaxial copper suplhate load and generates a square voltage pulse of 5 ns pulse width across 60 Ω load assembly. Output voltage of 50 kV is recorded across matched copper sulphate load using load cum divider assembly and 6 GHz Lecroy oscilloscope. Voltage waveform and corresponding FFT is displayed in figure 4.21. Output wave form is found to have a lump halfway i.e. after 2.5 ns. This is attributed to imperfect reflection of the voltage wave front at the MARX feed point. Under ideal condition there should be complete reflection of voltage wave front from MARX generator feed but in practical world complete reflection does not take place. Moreover geometrical asymmetry in the coaxial structure of the line, because of centre feeding of MARX generator, creates impedance asymmetries in the pulse forming line. As a result of which this lumpy nature in the pulse is observed.

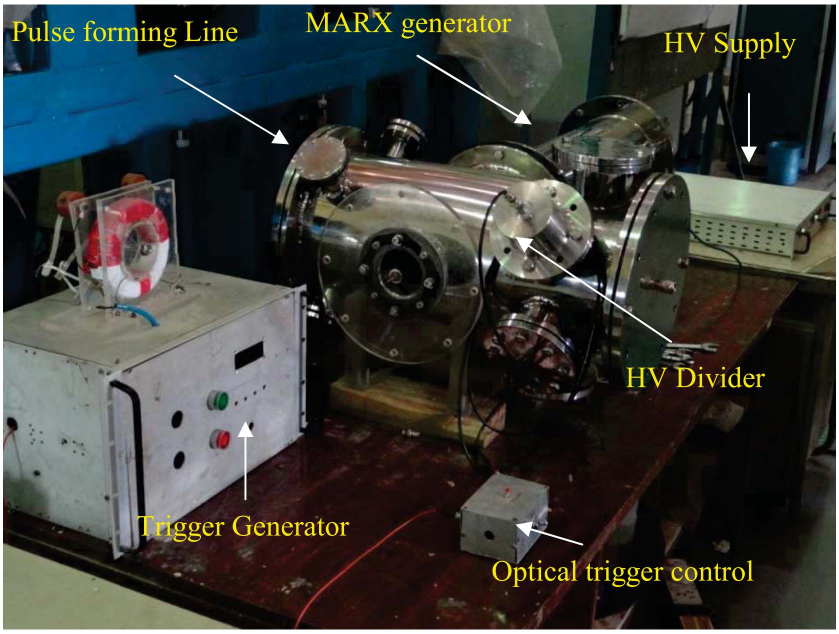

Fig.4.19 Photograph of the experimental set up

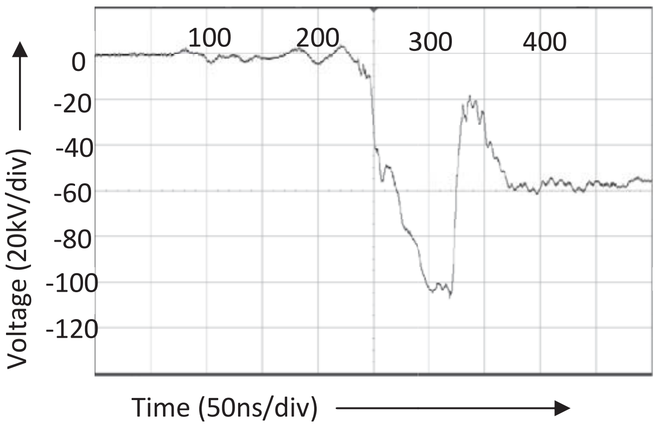

Fig.4.20 Charging and discharging profile of PFL

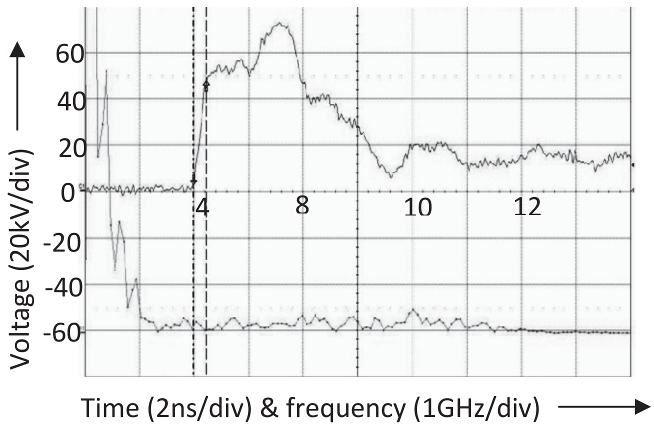

Fig.4.21 Output voltage pulse and its FFT

However, first part or the rise time part of the pulse is significantly clean and suitable to measure the rise time of the pulse. This rise time is function of inductance of discharge path and mostly contributed by arc channel inductance of sparkgap under test.

Hence, inductance of arc channel is estimated by using this rise time data. Details of calculation methodology and obtained results are narrated in the next chapter. This experiment endorses suitable performance of the experimental set up to conduct experiment with different parameters of sparkgap i.e. gap between electrodes, pressure of the gas medium and different gases for detailed investigations. Results of the same are reported in the following chapters.

4.10 Role of stray capacitors in rise time of the voltage pulse should be addressed.

In context of the experimental set up used in this research work, stray capacitance affect rise time of the voltage pulse differently in different places. Experimental set up described in figure 4.19 consists of a MARX generator, pulse forming line, Sparkgap under test and a load. Role of stray capacitances in each stage has been elaborated below.

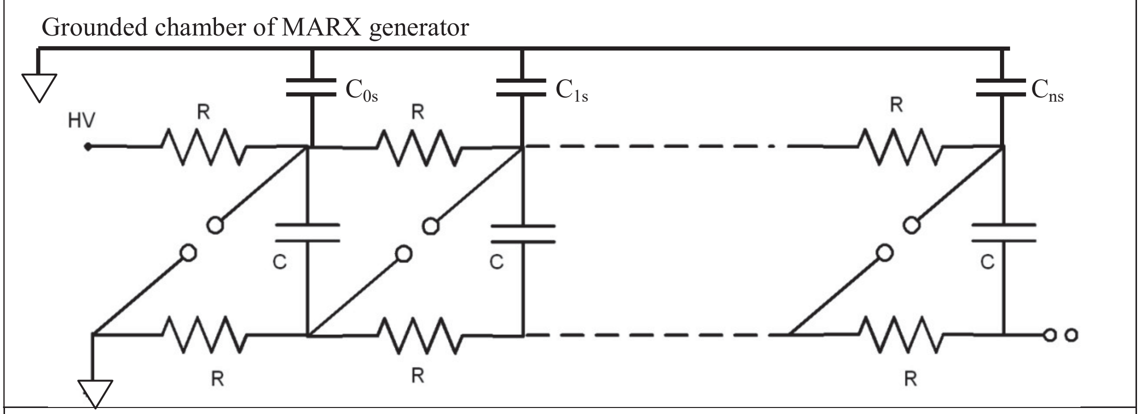

Fig. 21. Figure showing stray capacitance of MARX generator

a) Stray capacitance in MARX generator: MARX generator by its structure is composed of certain number of capacitors, which are charged in parallel and discharged in series. Metallic components present in each stage forms stray capacitances amongst themselves and with the grounded enclosure of the MARX generator. While charged using DC voltage source (in this experimental set up maximum up to 50 kV), these stray capacitances also gets charged to maximum of 50 kV. However, during erection these capacitors get charged to different voltages depending on their position. As an example, while erecting, stray capacitance at metallic components of 2nd stage capacitor (C_{2S}) gets charged to 2V, stray capacitance at metallic components of 3rd stage capacitor (C_{3S}) gets charged to 3V, stray capacitance at metallic components of 4th stage capacitor (C_{4S}) gets charged to 4V and so on to stray capacitance at metallic components of nth stage capacitor (C_{ns}) gets charged to nV. Each of these capacitors store energy and draws it from the stored energy of the MARX generator. Total energy stored in these stray capacitances can be calculated as

$$E_S = \frac{1}{2}[C_{1S}V^2 + C_{2S}(2V)^2 + \ldots + C_{nS}(nV)^2] \tag{4.23}$$

If it is assumed that stray capacitances of all the metal parts are almost same in values, because of symmetric design of MARX generator, then the energy term reduces to

$$E_S = \frac{1}{2}C_S V^2[1 + 2^2 + 3^2 + \ldots + n^2] = \frac{(n^2+1)n}{4}C_S V^2 \tag{4.24}$$

Now, if upon discharge MARX generator charges the Pulse forming line to a voltage of nV , then this effect of stray capacitance can be represented by an equivalent capacitance C_{eqs}. This equivalent capacitance can be defined as follows

$$C_{eqs} = \frac{\frac{(n^2+1)n}{4}C_S V^2}{(nV)^2} = \frac{(n^2+1)}{4n}C_S \tag{4.25}$$

This equivalent capacitance appears in parallel to PFL capacitance while charging from MARX generator. This stray capacitance increases the rise time as root square proportion.

b) Stray capacitance in Pulse forming line: pulse forming line by its structure is composed of two concentric cylinders. These cylinders form capacitances amongst themselves. These capacitances, formed between the geometric structures of pulse forming line, are technically stray capacitances. However due to symmetry of geometry, they form Pi- network of capacitances and inductances. Capacitance values of these structures can be calculated using standard coaxial formula. While charging the Pulse forming line, voltage pulse frequency is much lower (approximately in the range of 20 MHz). Hence, pulse forming line mostly acts as a capacitor of capacitance value summation of all its stray capacitances. However, during discharge frequency of operation is much higher 100 MHz - 1 GHz. At this frequency inductances of pulse forming line separating stray capacitances become significant and pulse forming line become more accurately modeled as pi network. For circuit theory modeling this Pi network, to use in circuit calculations, Thevenin equivalence of the same is calculated. Thevenin equivalent voltage of a pulse forming line charged to a voltage of V_c, is equal to V_c . Thevenin equivalent impedance of such line can be defined as

$$Z_{eq} = Z_0 \coth(s\delta) \tag{4.26}$$

This formula incorporates presence of stray capacitances in the pulse forming line. In this thesis, all the modeling and calculations of rise time are carried out using this circuit equivalence to incorporate effect of stray capacitance during discharge of pulse forming line into copper sulphate or antenna load.

Effect of stray capacitance in MARX generator and pulse forming line is described above in detail. It can be noticed that, effect of stray capacitance of MARX generator in deciding rise time of pulse forming line is significant, more so in cases where number of stages are high. However, during discharge of pulse forming line it does not play any significant role. Stray capacitance of pulse forming line plays role in formation of pulse shape and rise time across the load. Effects of these stray capacitances are incorporated in the analysis using Thevenin circuit equivalence. However, it should be mentioned that, the pulse forming line under test, is a finite one and introduces fringe effects at both the terminals. This fringe effect contradicts the assumption of uniform values of stray capacitances across the pulse forming line. Incorporation of this non uniformity in the analytical model increases the complications of analytical calculations to multiple folds. However, these variations are already incorporated in the field simulations carried out using standard software.

4.11 Conclusion

In this chapter detailed description of the experimental setup is given. This experimental setup is composed of MARX generator, pulse forming line, voltage divider, trigger generators and specially designed load cum divider assembly. Design, analysis and simulations of different subsystems of the experimental set up have been described in detail in this chapter. Experiments conducted to check performance of different components are also discussed in details. Whole set up is assembled together and output pulse is measured under typical operating condition. Minor deviations are observed in the practical pulse compared to simulated one. These deviations are attributed accordingly to different imperfections in the experimental set up while comparing with the simulations. However, these deviations are minor in nature and do not seem to affect the final measurement of interest. This experimental set up is used for measurement of inductance of sparkgap arc channel by varying gaps between electrodes and pressure upto 5 kg/cm^2 in nitrogen atmosphere. Details of the experimental results, measurements and analysis are narrated in the following chapters.

Chapter 5
Measurement of sparkgap inductance

In this chapter detailed description of the method used for measuring inductance of the sparkgap is elaborated. Spark gap inductance along with its arc channel and connecting lead is expected to be in the range of few tens of nano Henrys. Measuring such a low inductance is a challenging task and accuracy of measurement is not very high. To make the measurement as reliable as possible several steps are taken and best engineering practices are followed. Experimental set up described in the previous section generates a square like pulse across load cum divider assembly. When voltage is measured across a copper sulphate load a finite rise time in the range of few hundreds of pico seconds is observed. Now assuming the load as a constant resistance, and inductance in the loop is in series with the load, it is mathematically possible to find out the inductance of the loop. In this calculation capacitance of the load resistor is neglected as its effect is reasonably low. Detailed description of the inductance measurement methodology is narrated below.

Further experiments are conducted by varying gas pressure and the gap between two electrodes, in steps and inductance of sparkgap is calculated from the wave form obtained. Simulations are conducted for similar condition and results are tabulated in comparison with the experimental results. Experimental results are found to be in consistence with the simulated results. As the whole phenomena are highly statistical and observations are in extreme fast domain of sub nanoseconds, inherent shot to shot variations are observed during experimentation. Multiple observations are carried out in the similar physical condition to reduce the effect of random variation. All the experimental data, analysis and simulation results are narrated in detail in this chapter.

5.1 Method of measurement of inductance

Inductance of sparkgap is measured by measuring the rise time of a voltage pulse generated by discharge of pulse forming line into a matched load. A pulse forming line can be assumed as a Pi network of distributed inductance and capacitance. When discharges into an ideal inductance free load resistance it is supposed to generate a step voltage front across the load. With the progression of the voltage front, pulse forming line discharges completely and theoretically speaking, a square pulse is generated across the dummy load of matched resistance value. Detailed mathematical analysis of discharge of pulse forming line is elaborated in chapter 4. The amplitude of the output voltage and the voltage wave front, is function of load resistance and characteristic impedance of the pulse forming line. Pulse width of the pulse is determined by the double transit time of the pulse forming line. In real world due to presence of inductance in the load resistor loop, zero rise time across the load resistor can hardly be realized. But by assuming PFL as an ideal step input to the load resistance and using Laplace's transform equations for transient analysis, inductance of the load loop can be determined.

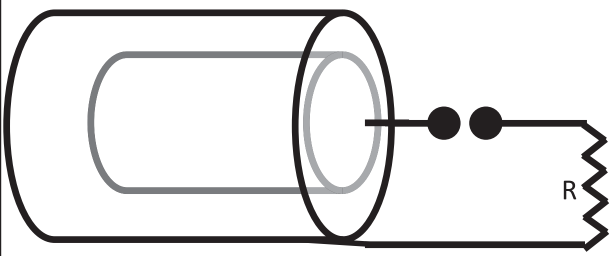

Fig. 5.1 PFL discharging circuit

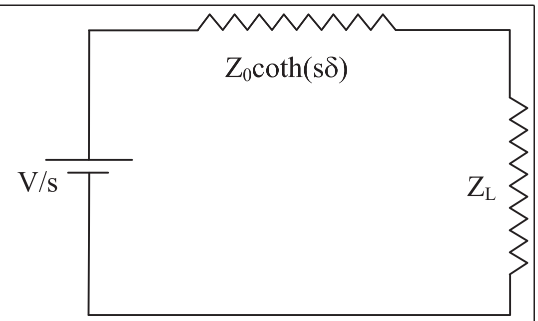

Fig.5.2 Equivalent circuit of PFL discharge

This inductance will include spark gap arc channel inductance, lead inductance and inductance of the load structure itself. Figure 5.1 shows the discharging circuit of pulse forming line into a matched load. Figure 5.2 shows the equivalent circuit of the same. Referring to the equation (4.5) in presence of inductance it can be written that

$$V_L(s) = \frac{VZ_L[1- e^{-2s\delta}]}{s(Z_L+Z_0+Ls)}[1 - \left(\frac{Z_0-Z_L}{Z_0+Z_L}\right)e^{-2s} + \left(\frac{Z_0-Z_L}{Z_0+Z_L}\right)^2 e^{-4s\delta} - \cdots] \quad (5.1)$$

For $Z_L = Z_0$ equation (5.1) reduces to

$$V_L(s) = \frac{V[1- e^{-2s\delta}]}{s(2+\frac{Ls}{Z_L})} \quad (5.2)$$

Hence,

$$V_L(s) = \frac{VZ_L[1- e^{-2s\delta}]}{Ls(\frac{2Z_L}{L}+s)} = \frac{VZ_L[1- e^{-2s\delta}]}{Ls(\frac{2Z_L}{L}+s)}\left[\left(\frac{2Z_L}{L} + s\right) - s\right]\frac{L}{2Z_L} \quad (5.3)$$

Therefore

$$V_L(s) == \frac{V[1- e^{-2s\delta}]}{2}\left[\frac{1}{s} - \frac{1}{\left(\frac{2Z_L}{L}+s\right)}\right] \quad (5.4)$$

Hence in time domain the voltage wave form can be written as

$$V_L(t) = \frac{V}{2}[1 - u(t-2\delta)]\left[1 - e^{-\frac{2Z_Lt}{L}}\right] \quad (5.5)$$

Hence,

$$t_{0.9} - t_{0.8} = -\tau(\ln 0.1 - \ln 0.2) = 0.69\tau = 0.69\frac{L}{2Z_L} = 0.345\frac{L}{Z_L} \quad (5.6)$$

Therefore,

$$L = Z_L(t_{0.9} - t_{0.8})/0.345 \quad (5.7)$$

Where $t_{0.9}$ represents time taken to cross 90% of final value and $t_{0.8}$ represents time taken to cross 80% of final value.

In this context it must be mentioned that inductance has been calculated from the time interval of 80% to 90% of final value instead of standard 10% to 90% time interval. This method is adopted to avoid inaccuracies in the estimation of inductance incorporated due to turn on of sparkgap.

Voltage profile obtained from equation (5.5) is valid with certain conditions. One of the most important conditions is that turn on time of the switch is infinitesimally small. In practice no switch closes with zero turn on time. But provided, the circuit response is sluggish compared to turn on time of the switch the analysis gets reasonably close to practical. In this experimental set up rise time of hundreds of pico second is being attempted to measure. This rise time is contributed by inductance of the circuit. But turn on time of sparkgap switch is also comparable to this range. As a result of which rise time of the pulse contains both the factors i.e. turn on time of the spark gap and circuit inductance. As a result of which the output pulse does not exactly follow exponentially rising nature. Rather the waveform matches the following equation more closely [refer figure 5.3].

$$V_{L1}(t) = \frac{\frac{V}{2}[1-u(t-2\delta)]\left[1-e^{-\frac{2Z_L t}{L}}\right]}{\left[1+\left(\frac{R_{SO}}{Z_0+Z_L}\right)e^{-\frac{t}{\tau_1}}\right]} \qquad (5.8)$$

Where, R_{SO} is the open circuit resistance of sparkgap and τ_1 is turning on time constant of the switch. From this equation it can be shown that at the initial phase of turn on voltage profile is not exponential, but once the sparkgap resistance reduces below the range of milliohms equation (5.8) converges to equation (5.5). This phenomenon has been shown very clearly in figure 5.3. In this figure three curves i.e. V_L, V_{L1} and experimentally measured pulse are plotted together in the same axis. This figure shows that experimentally obtained curve matches V_{L1} profile for all the time span but matches V_L only as it approaches final value. This is because of the fact that, by the time voltage closes to steady state value, sparkgap resistance becomes almost negligible. Hence to calculate inductance of the sparkgap, time span between 80% peak voltage and 90% of final voltage is used.

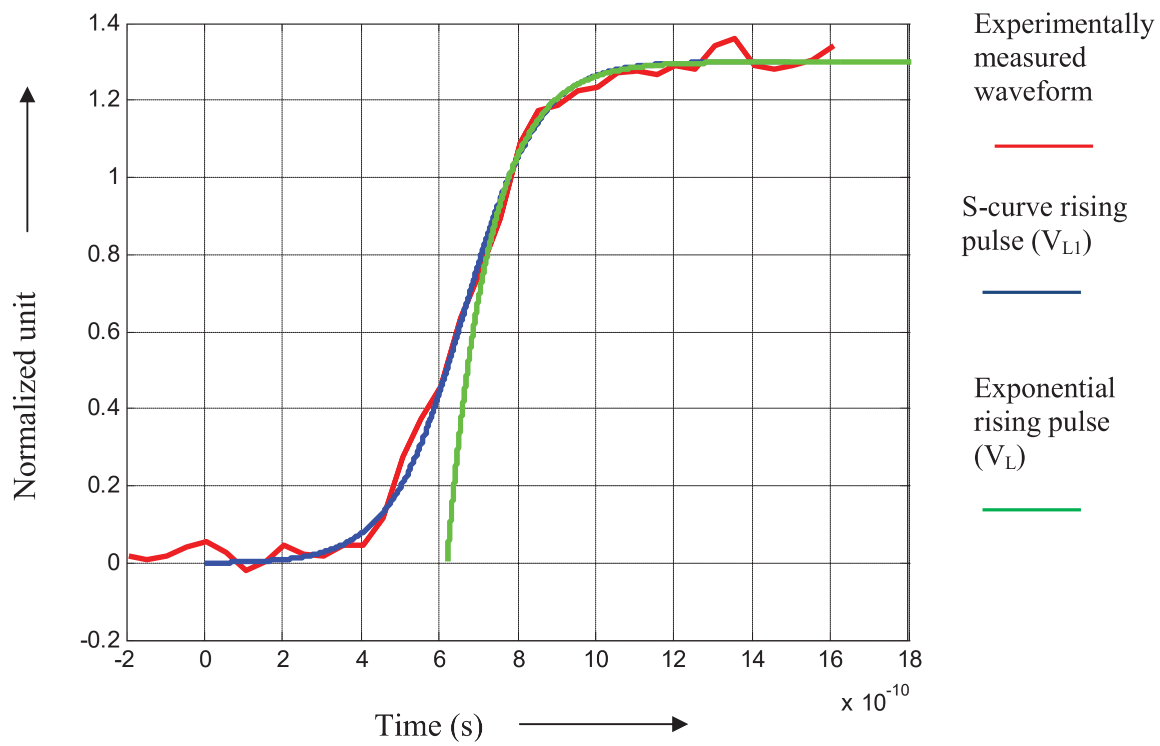

Fig.5.3. Experimentally measured waveform (red), V_{L1} (S-curve rising pulse) and V_L (exponential rising pulse)

In this range, the rising voltage pulse, matches exponential rising nature very closely. In cases where rising time constant is much higher than that of the ON time of the sparkgap; there 10% to 90% rise time can be suitably taken to determine the loop inductance. In this case this may be erroneous and 80% to 90% rise time has been taken to minimize the error in calculation of inductance.

5.2 Measurement of inductance of typical electrode gap

Experimental setup described in previous chapter is used for measurement of inductance of arc channel. The coaxial cylindrical pulse forming line is charged to 100 kV using the MARX generator. MARX generator is charged to 12 kV and triggered using optically controlled trigger supply. N_2 is used as insulating gas in pulse forming line as well as gap between electrodes. A sparkgap is used to discharge the capacitor into a low inductance 60 Ω copper sulphate load. The rise time of the voltage across the resistive load is monitored using specially designed resistive divider and 6GHz oscilloscope. Time span between 80% to 90% of final value is approximately 75 ps. This data is used for measurement of inductance using equation (5.7). Experimental wave form is shown below in figure 5.4.

Values used in the calculation are as follows

$(t_{0.9} - t_{0.8}) = 75$ ps obtained from the recorded waveform.

$Z_L = 60\ \Omega$; pulse forming line characteristic impedance and load impedance are equal and kept close to 60 Ω.

Hence loop inductance is $L = .075X60/.345 = 13$ nH.

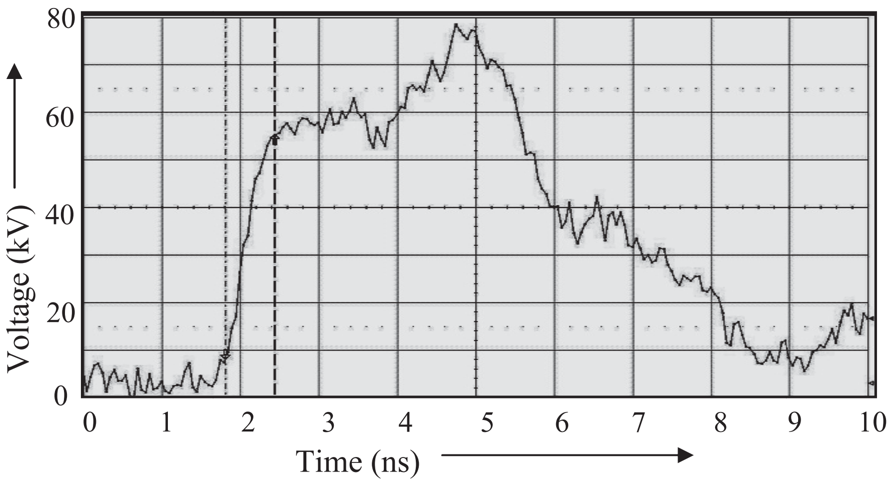

Fig.5.4 Typical output voltage measured across dummy copper sulphate load (X axis 1ns/div, Y-axis 10kV/div)

Inductance measured by this methodology is little over estimation of arc channel inductance. This basically measures the loop inductance of the discharge circuit. Moreover response time of the divider also adds to the estimation of the inductance. Sufficient care has been taken to ensure coaxial arrangement of load as well as divider in this experimental setup. However some amount of inductance definitely is contributed by these lead connections. At this present moment it is impossible to differentiate the lead inductances from arc channel inductance. In the next section attempts has been made to quantify the lead inductance and reduce the same from the total measured inductance to determine arc channel inductance more accurately. In this context it must be mentioned that the order of measurement being attempted here is significantly low. Hence there is always chance of inaccuracies, but all attempts have been made to measure the inductances as accurately as possible, such that proper calibration and correlation can be established with the simulated results. Results in pulsed power experiments vary statistically, to avoid statistical errors in estimation multiple experiments are carried out with same physical parameters. Details of those experiments with variation of parameters are discussed in following sections.

5.3 Experimental results of inductance with variation of gap

Study of arc channel inductance with variation of gap between electrodes is carried out as a part of this project. According to Paschen curve, breakdown strength of gases increases with increase in pressure and distance beyond Paschen minima. For Ultra Wide Band application the very requirement is to increase the voltage handling of sparkgap switch vis-à-vis reduction of arc channel inductance. Hence it is extremely important to understand how inductance of arc channel changes with variation of pressure and distance i.e. gap between electrodes. As part of this study, experiments are carried out in nitrogen environment at atmospheric pressure. Gap between two electrodes of the sparkgap under test is increased from 1 mm to 9 mm in step of 1 mm. Rise time of the pulse is measured using an oscilloscope. Inductance of the arc channel is calculated from the measured pulse using equation (5.7). As discussed in the previous chapter, there is an expected shot to shot variation involved in the sparkgap break down phenomena and its corresponding measurement. To avoid shot to shot random variation effects, multiple shots are taken and all of them are plotted below in figure 5.5. Shot to shot variations are mostly contributed by position of formation of arc channel in the sparkgap. Moreover there is inherent measurement variation which also contributes to shot to shot variations. However, in spite of the natural standard deviations, data obtained are comprehensive and conclusive. While plotted together a natural trend is well observed.

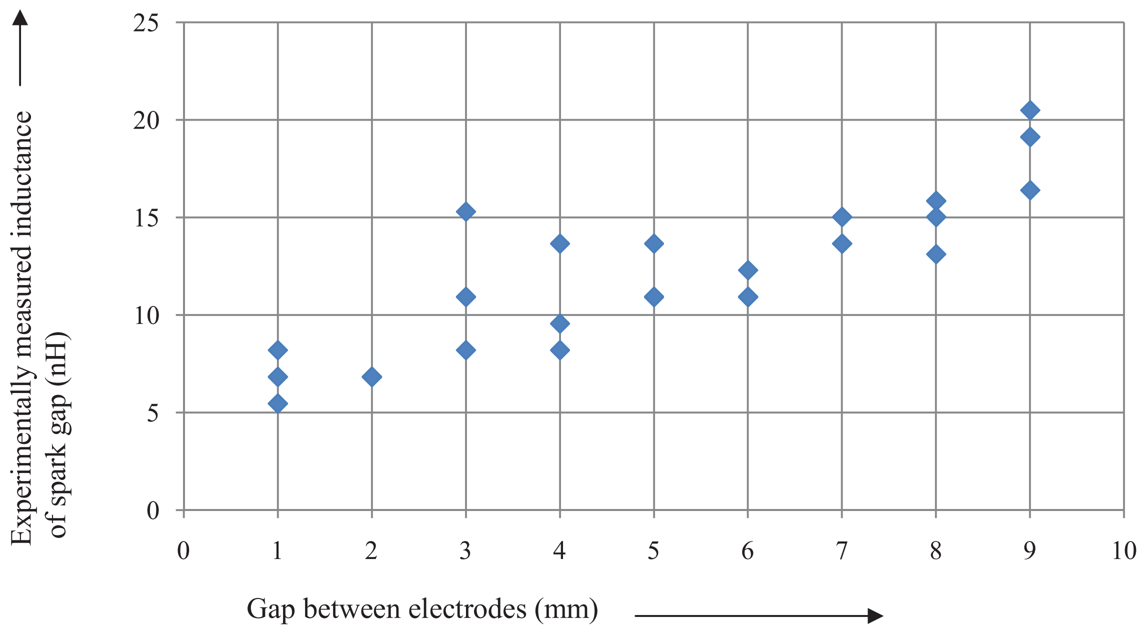

Fig.5.5 Inductance variation of sparkgap with gap between electrodes

Results show an almost linear pattern of inductance variation with increment of electrode gaps. This categorically indicates that with increase in gap between electrodes inductance increases monotonically. Observation indicates that domination of length parameter dominates other variations significantly in case of gap change. With change of gap between electrodes, length of the arc changes directly. Hence inductance, resistance and current profile through the sparkgap also alters. It is evident that current through the sparkgap will have an impact on arc channel radius. However, length of arc dominates inductance so directly that effect of other parameters seems comparatively negligible. Specifically when it comes to measurement, statistical variations overshadow any other effect, even if it is present. But effect of gap variation is so distinct that vivid change in inductance with variation of gap between electrodes is clearly visible. From figure 5.5 it is observed that if the gap between electrodes would have been zero (theoretical assumption), measured inductance would have been somewhere close to 4 nH (i.e. intercept on Y-axis). This indicates that lead inductance of the loop is close to 4 nH. This 4 nH of inductance mostly consists of any loop inductance other than arc channel. This inductance also may include measurement delays and response times as an error in rise time measurement and thus part of calculated inductance. However, if 4 nH is deducted from all the measured inductance values, only arc channel inductances are left with. These corrected values of arc channel inductances are plotted in figure 5.7.

Simulations are carried out to compliment the experiment using simulation code described in chapter 3. Separate program runs are carried out for separate gap setting of 2 mm to 10 mm at an interval of 2 mm. Results show an excellent linear variation of arc channel inductance with variation of gap between electrodes. Minor variations are attributed to simulation accuracies. Results obtained from simulations are plotted in figure 5.6. In figure 5.7 simulation results are plotted along side with experimentally obtained arc channel inductances (corrected). Results obtained are in close agreement with each other and establishes the fact very strongly that arc channel inductance is a linear monotonic function of gap between electrodes in the range of experiment and simulations carried out in this project. Effect of pressure is studied and narrated in the next section.

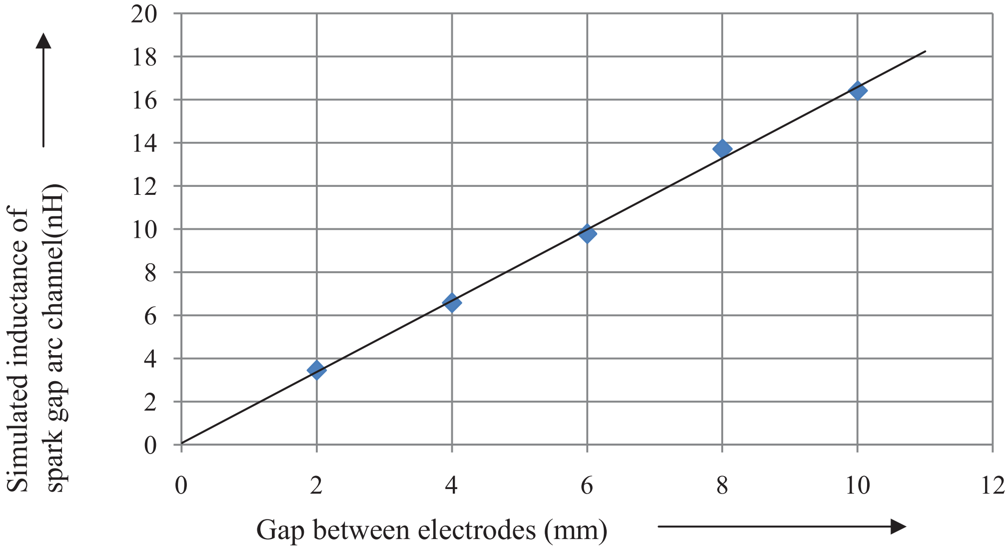

Fig.5.6 Simulated inductance of arc channel at different

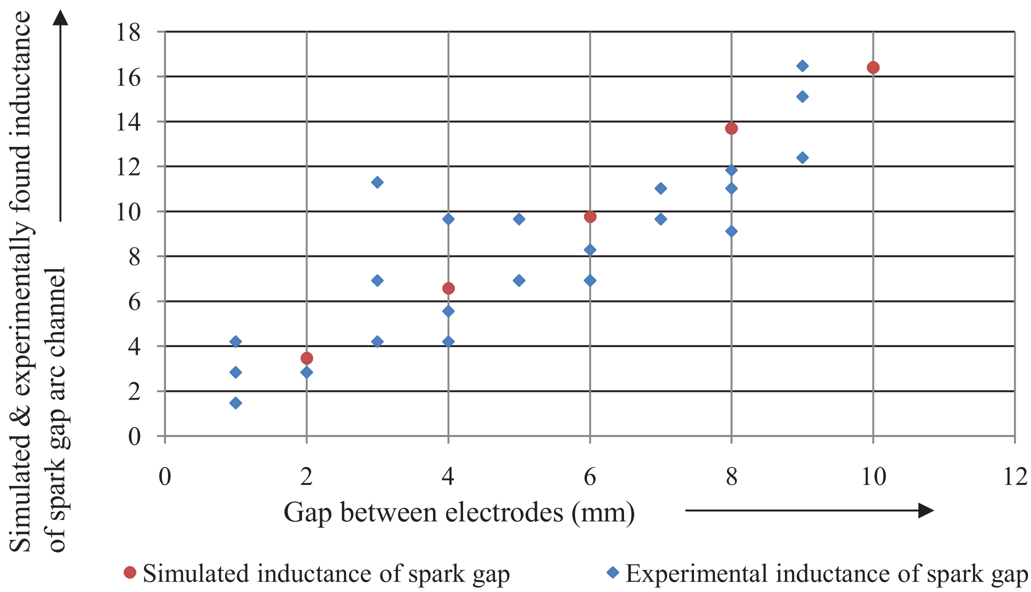

Fig.5.7 Inductance of arc channel at different gaps

5.4 Experimental data of inductance variation with pressure

Second important parameter in the context of ultra wide band system is the effect of pressure in inductance of arc channel. With increase of pressure in the sparkgap, complicated physical phenomena are initiated. With increase of gas pressure, number of gaseous molecule, present in a volume, increase proportionally (according to Charle’s law of gases). Electrical conductivity of gases, at any particular temperature, also varies with pressure. With onset of arc channel, as the current starts flowing through, heat energy starts depositing in and around it. But ionization of gases being a thermal phenomenon (as assumed in this model) demands more energy to ionize gaseous kernels around arc channel. This happens mostly because of the very fact that at high pressure condition more number of molecules are present at the vicinity of the arc channel, and requires higher energy for complete ionization of all the molecules. Hence, increase in conductivity of close kernels of arc channel is rather slow in high pressure gaseous medium compared to atmospheric pressure condition. As a result of which simulation indicates that arc channel radius is smaller in high pressure medium compared to atmospheric condition. This also influences inductance of arc channel and smaller radius causes higher inductance of arc channel. However, change in inductance with gas pressure is not linear because inductance varies as logarithmic function of radius.

Experiments are carried out at different gaps between electrodes of sparkgap to study the effect of gas pressure. Inductance is measured at different gaps i.e. 1 mm, 2 mm, 4 mm, 6 mm, 8 mm and 10 mm with varying pressure from atmospheric pressure to 5 kg/cm^2 pressure (relative). It is observed that variation of inductance with pressure is significantly low and below the range of statistical shot to shot variation. Moreover higher voltage is required for breakdown of sparkgap while gap and pressure both are high. At 6 mm gap experiment was conducted only up to 3 kg/cm^2 pressure (relative). In 8 mm gap sparkgap firing stops beyond 2 kg/cm^2 (relative). At 10 mm gap experiments were possible only up to 1 kg/cm^2. Results obtained from these experiments are plotted in figure 5.8. Results show that shot to shot statistical variation is significantly high compared to expected range of variation. Secondly experimental data available for higher gaps are too small for making any conclusive comment on the dependence of inductance on gas pressure. But this experiment provided the direction that, to measure variation of inductance with pressure an experimental set up capable of generating higher voltage is required. Experiments required to be planned for higher pressure range to significantly identify the nature of variation. This conclusion is also supported by simulated results plotted in figure 5.9. Simulated results show that with increase in pressure of gas medium, inductance of arc channel increases but the variation is significantly low. Presented experimental result has clearly exhibited the statistical variation. As the variation of inductance with gas pressure is lower than statistical variation, experiments could not validate the simulation results. Hence, another experimental setup has been developed for measuring variation of inductance with pressure. The new set up is capable of generating 1 MV and handling pressure up to 40 kg/cm^2. This setup enables us to measure variation of inductance with wide range of pressure variations. Care has also been taken to reduce statistical variations. Details of high pressure experimental set up are discussed in next chapter of the thesis.

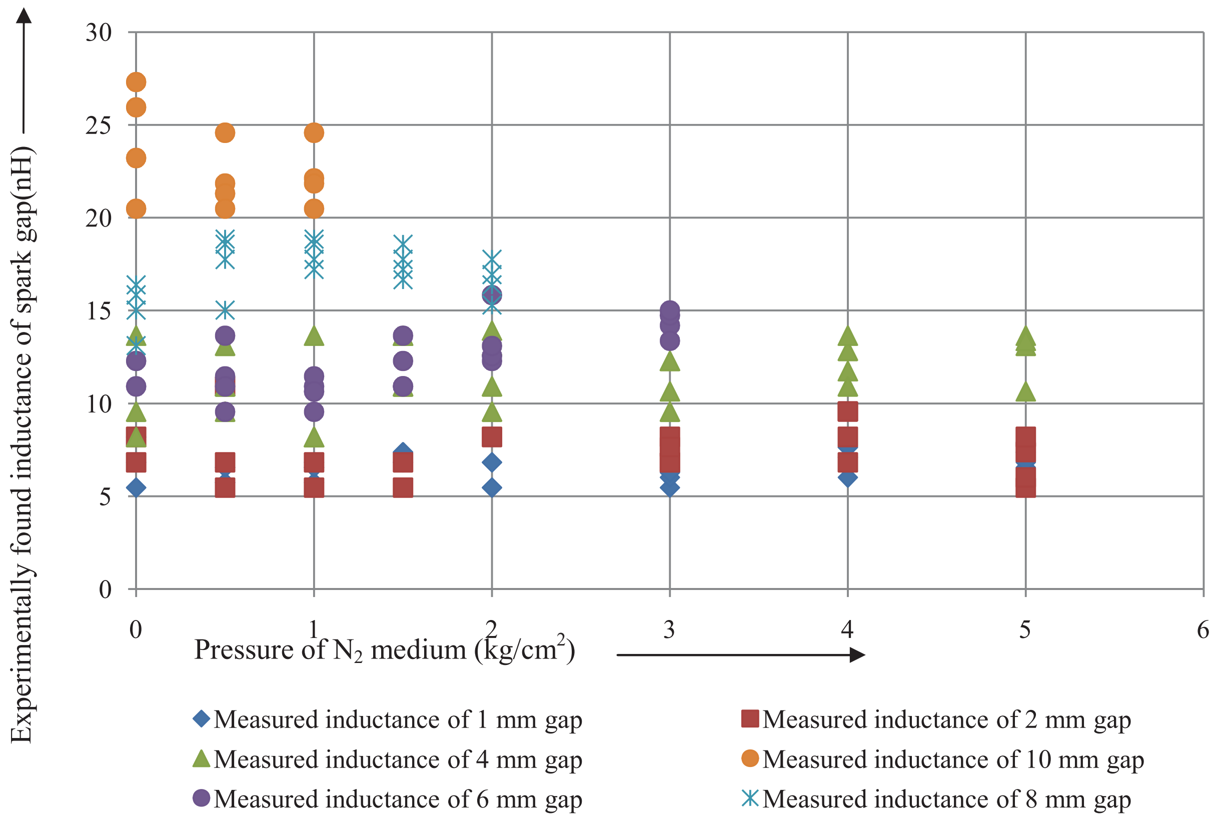

Fig.5.8 Inductance of arc channel at different gaps and pressure of N_2

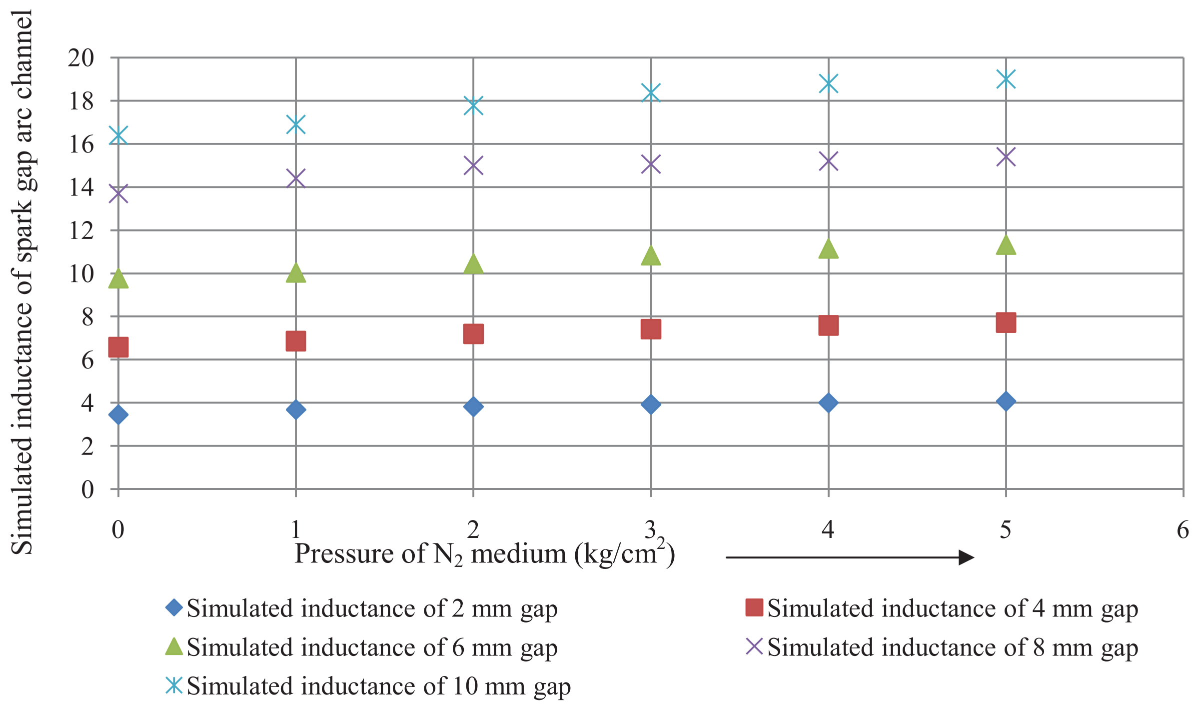

Fig.5.9 Simulated inductance of arc channel at different gaps and pressure of N_2 medium

5.5 Discussion & Analysis

In this chapter measuring methodology of spark gap inductance from the experimental set up (described in chapter 4) is thoroughly discussed. A typical measurement is explained with step wise calculation to measure inductance of arc channel by experimentation. In this context it is important to mention that measurement of the pulse rise time in sub nanosecond regime inherently introduces sufficient amount of measurement errors. These are cumulative errors introduced by the divider, oscilloscope, connecting cables etc. Moreover in the operation of self breakdown sparkgap, certain amount of random uncertainty is always involved. To minimize these effects multiple shots are taken in the same condition (pressure, gas and anode-cathode gap). Several shots are taken by varying gaps and pressures. All these results are discussed thoroughly in this chapter.

With variation of electrode gap, inductance is found to be monotonically increasing. The pattern of increment of inductance with electrode gap is almost linear. This is found by simulation and validated through experimental results reasonably accurately.

In this chapter experimentally measured inductances of spark gap arc channel is plotted against variation of pressure of nitrogen gas. Gas pressure is varied from 0-5 kg/cm^2 to measure inductances of arc channels. A minute increment of inductance with increase of pressure was expected from simulation. Due to statistical variations in obtained experimental data, this minute increment is not clearly observable. However the pattern of minute increment of inductance can be realized as all the readings are plotted together. Experimentation with higher pressure may exhibit this pattern more clearly but due to experimental constraint pressure has been limited to 5 kg/cm^2.

Keeping UWB application in mind it can be concluded that to get faster rise time it is essential to keep the gap between electrodes as minimum as possible. Keeping the gap as minimum as possible and operate at high voltage only two options can be attempted i.e. operating at higher pressure of gas and operating with gases having higher breakdown strength i.e. SF_6. Hence experiments need to be carried out in this context to establish variation of inductance with pressure and different gases. For carrying out this further high voltage experiment different experimental set up has been developed and measurements are carried out. Details of the high pressure high voltage experimental set up and measurements conducted thereafter are narrated in detail in following chapters.

Chapter 6
Development of high pressure 1 MV experimental set up

In this chapter detailed description of the experimental set up prepared under this thesis work is elaborated. Development of experimental setup plays a very crucial role in further experimentation, collection of data, analysis of data and validation of simulation model described earlier in chapter 3. The whole setup consists of high voltage power supply, MARX generator to charge PFL capacitor, solid dielectric pulse forming line assembly, and Half Impulse Radiating Antenna. MARX generator and pulse forming line assembly needs gas pressurization for rated voltage operation. All the systems required for developing the experimental set up, is designed and fabricated in house. Details of all the components and experimental methodologies are described below.

6.1 Description of the Experimental system

Experimental system is mainly composed of three distinct components i.e. MARX generator, pulse forming line and radiating antenna. 60 kV high voltage unipolar power supply is used for charging of the MARX generator. MARX generates maximum of 1000 kV voltage pulse to charge the pulse forming line which when discharges into a matched antenna load of 100 Ohms a 500 kV, 5 ns voltage pulse is obtained. Voltage pulse generated via discharge of pulse forming line sparkgap is radiated by Half Impulse Radiating Antenna (HIRA). Radiated pulse is sensed by using a TEM sensor and waveform is measured using high frequency (8 GHz) oscilloscope. Rise time of the input voltage is calculated from obtained radiated E-field measurement. Inductance of the spark gap is calculated from the rise time of the pulse feeding the HIRA antenna.

6.1.1 MARX generator

Construction: Total 160 numbers of non inductive capacitors of 1.2 nF, 30 kV are chosen as energy storage elements. These ceramic capacitors are having a disk with metal fitting type electrode used for ultra high voltage applications. They are epoxy-encapsulated and using strontium titanate for dielectric material. The diameter of the capacitor is 38mm having thickness and length as 22 mm and 26 mm respectively. Each stage consisting of 8 capacitors (series of two banks each consist of 4 parallely connected capacitors) between two 'Cu' plates which will hold them together and one electrode of 15mm diameter is connected to each 'Cu' plate. Total of 21 spark gap switches all with an increasing gap distance from 5 mm to 10 mm from first spark gap to 21^{st} spark gap respectively is used. For charging of the capacitor, 2.2 kΩ charging and ground resistors are used. These resistors are approximately 25 mm in diameter and 50 mm in length. Fig.6.3, Fig.6.4 and Fig.6.5 show assembly of the high voltage components. The total Marx generator is enclosed in a metallic chamber made by stainless steel which provides a return path for the discharge current. While operated at normal atmospheric pressure MARX generator charges up to 12 kV and charges the pulse forming line approximately to 250 kV. Output of the MARX generator can be controlled by varying N_2 pressure upto 5 Kg/cm^2. While operated at charging voltage of 50 kV, MARX generator generates approximately 1 MV. In practice, the MARX generator charges the PFL higher than 1 MV because of capacitance mismatch between them. PFL is having lower capacitance than MARX generator, hence an over volting phenomenon is observed.

Intra-stage insulation coordination: Difficulties in designing this MARX generator are in handling its high voltage points suitably without causing any unwanted breakdown. MARX generator usually has two phases of high voltage handling. In the first phase, while the MARX generator is charged to comparatively lower value of high voltage i.e. approximately 50 kV. In the second phase MARX generator erects to generate much higher voltage of 1 MV. In both the cases requirement of high voltage design and considerations are little different. While designing MARX generators, both the requirements are needed to be taken care of. In the charging phase each stage is charged to same voltage. Hence, intra stage insulation plays more vital role compared to inter stage insulation. Suitable consideration must be taken that breakdown does not take place between the high voltage points of same stage. Most critical component that sees this high voltage directly is the energy storage capacitors. Surface of this capacitors are most susceptible points of intra stage breakdown. Sufficient care must be taken to avoid this kind of malfunctioning during charging. Secondly, any mechanical assembly that hold the high voltage capacitors in their place are sensitive to breakdown during charging. In case of metallic components proper care must be taken to avoid sharp edges, welding burrs and unevenness in them. These points have potential to initiate corona during charging which will corrode the material with time and lead to malfunctioning of the MARX generator. In case of holding materials being non metallic or insulating, surface of these materials are of extreme importance. These surfaces are the weakest link in high voltage handling of the system. In this context it should be worth mentioning, that most of the solid dielectrics generally used for high voltage applications have very high bulk breakdown strength. But their surface breakdown strength is not as high as bulk breakdown strength. Moreover surface breakdown strength is also a function of cleaning of the surface, presence of moisture in the atmosphere during handling of the material, presence of dust particles in the environment and surrounding dielectric i.e. liquid, gas etc. Besides this, presence of a triple point is also source of initiation for high voltage breakdown. Hence insulation coordination is extremely important. Hence, for insulating materials, wherever required, surface must be increased such that surface breakdown can be prohibited. Proper precaution must be taken to counter sunken nuts to avoid exposure of sharp threaded parts carrying high voltage.

Inter-stage insulation coordination: During erection phase of MARX generator each stage of MARX generator remains at different voltages i.e. first stage remains at 50 kV, second stage at 100 kV with respect to ground and so on till the final stage at 1 MV. In this case mainly two types of malfunctioning are dominant, unwanted inter stage breakdown and breakdown of any high voltage point with body ground. Designing is more complicated in this discharging phase because of its very high value of voltage, in this case it is 1 MV. For inter stage breakdown most susceptible part is charging resistor or ground resistor. These resistors and their mechanical assembly see significant high voltage during discharging phase of operation. Surface of this resistors are sensitive to high voltage flash over during erection of MARX generator. Sufficient standoff distance must be provided in connecting inter stage resistors to avoid malfunction of MARX generators. Finally during erection extreme high voltage points will have tendency to breakdown with the body ground and discharge the whole energy in unwanted path. Surface of insulating holders are most important contributor to this problem. To avoid such unwanted flashover two lines of shifted multiple slits are designed on the surface of Perspex insulator. These slits interrupt the direct line joining high voltage points and body ground. This ensures reduction in breakdown probability drastically. However, if improperly designed, this many a times reduces inter stage flash over distance and may allow inter stage flash over through the slit. Proper care must be taken to avoid any such condition and position of the slits must be judiciously selected. Besides this, all the metallic points carrying extreme high voltage must be suitably rounded off and corona balls must be used judiciously to avoid generation of corona which may lead to easy breakdown during erection.

Design of enclosure: In this context it must be mentioned that making a higher diameter body chamber definitely reduces probability of high voltage breakdown during erection. But, this introduces extra inductance in the circuit which eventually increases the charging time of the pulse forming line. So to keep the inductance of MARX generator low it is important to keep the return chamber body as close as possible. Moreover increase of the chamber increases the whole volume of the system significantly and makes it difficult to handle. Gas requirement to fill the chamber during high pressure experiments also increases.

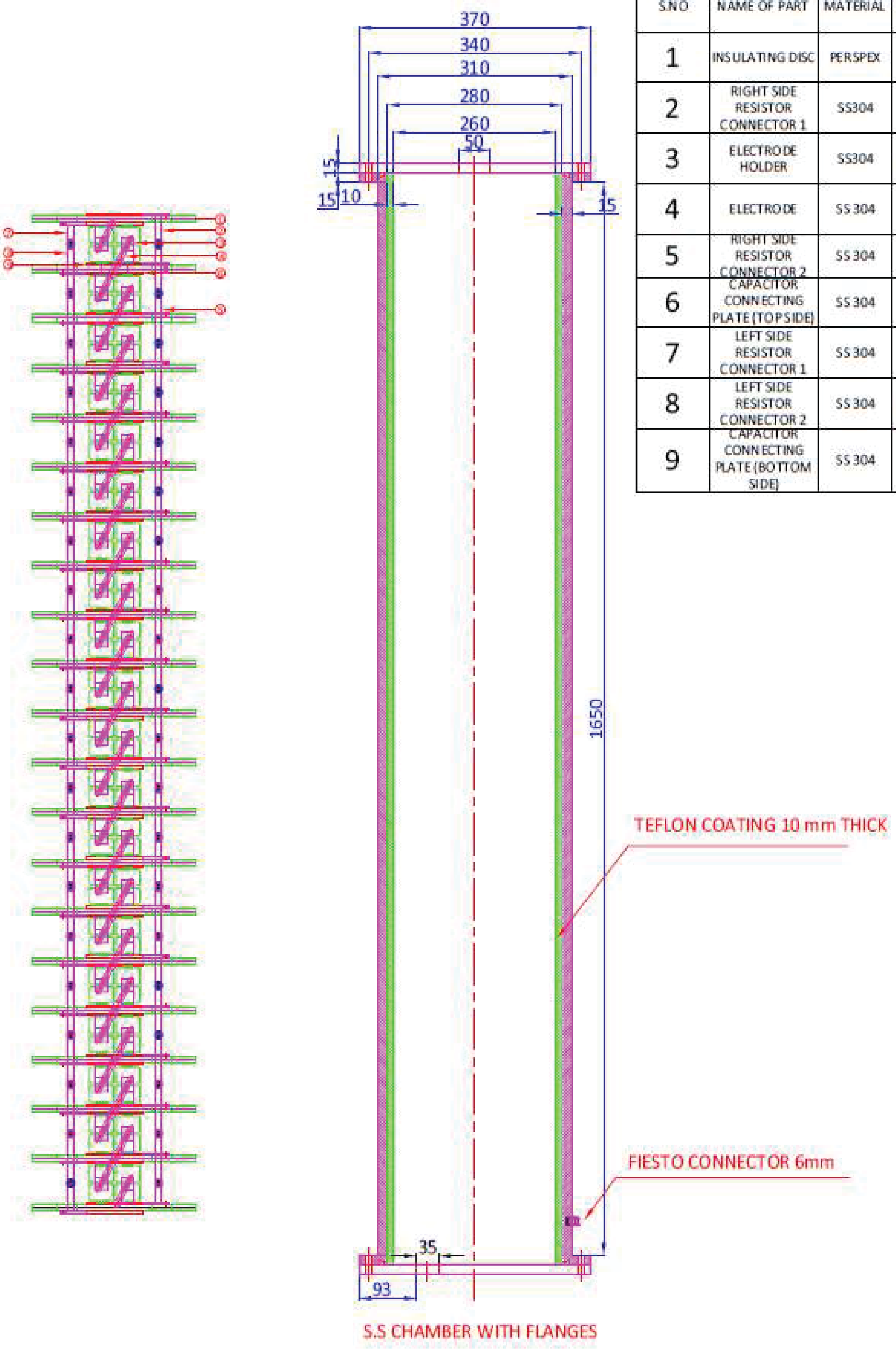

S.NO	NAME OF PART	MATERIAL	QTY
1	INSULATING DISC	PERSPEX	22
2	RIGHT SIDE RESISTOR CONNECTOR 1	SS304	22
3	ELECTRODE HOLDER	SS304	44
4	ELECTRODE	SS 304	44
5	RIGHT SIDE RESISTOR CONNECTOR 2	SS 304	22
6	CAPACITOR CONNECTING PLATE (TOP SIDE)	SS 304	22
7	LEFT SIDE RESISTOR CONNECTOR 1	SS 304	22
8	LEFT SIDE RESISTOR CONNECTOR 2	SS 304	22
9	CAPACITOR CONNECTING PLATE (BOTTOM SIDE)	SS 304	22

Fig.6.1 Drawing showing internal components of MARX generator

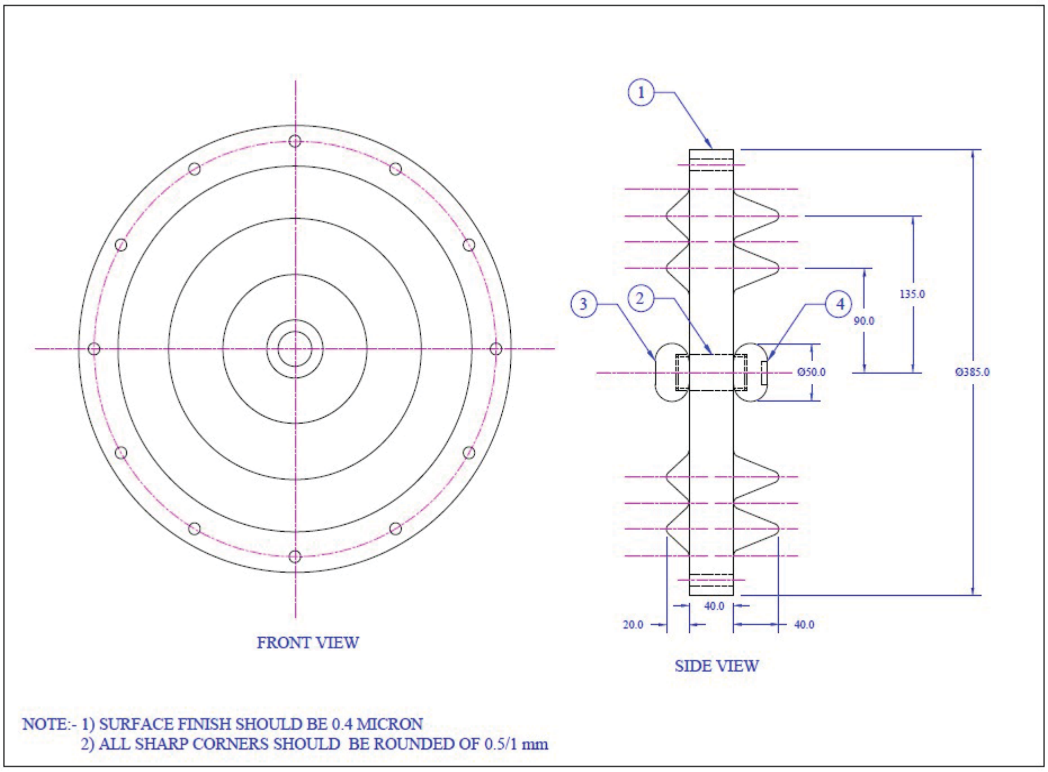

Fig.6.2 Drawing of high voltage feed through flange

Fig.6.3 Internal structure of MARX generator

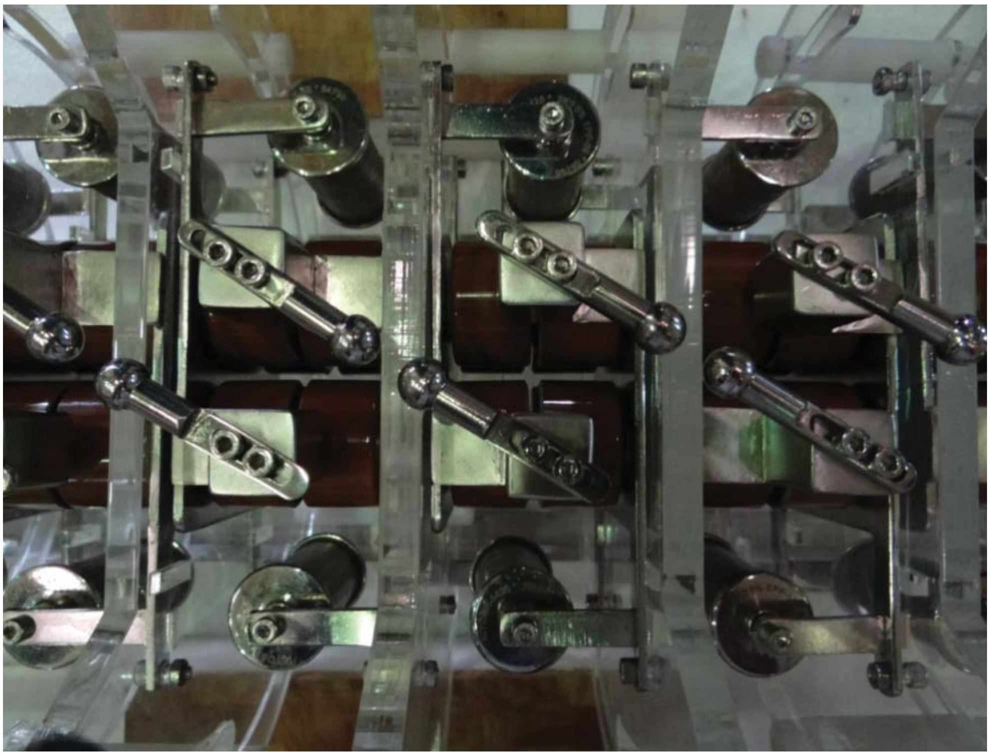

Fig.6.4 Close view of spark gap assembly

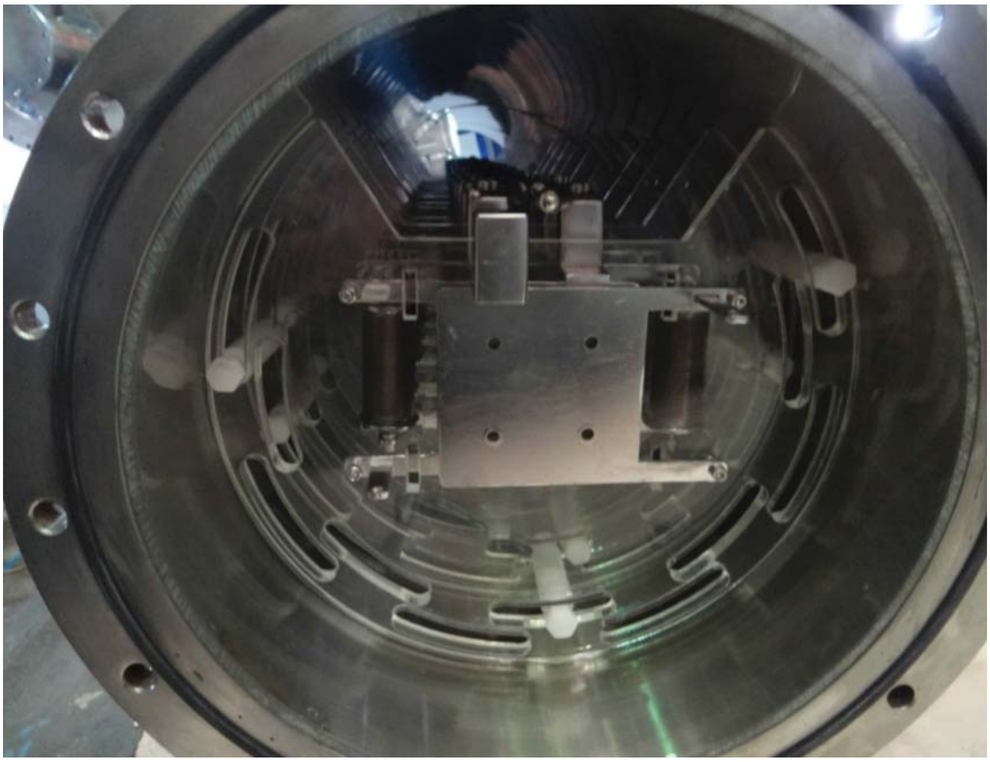

Fig.6.5 MARX generator assembly

After the MARX generator, high voltage design of final feed through is very significant. It is designed to handle high pressure of the chamber keeping in mind the high voltage constraints of the same. Diameter of the feed through is 385 mm and thickness is 40 mm. It is made up of Perspex for its excellent high voltage handling capability. To increase the surface strength of the feed through corrugations of required dimensions are introduced. In this context it must be noted that corrugations of different dimensions are designed for either side of the feed through. This is because; outer side of the feed is always going to be at normal atmospheric pressure whereas inner side of the feeding flange will be seeing higher pressure at higher voltage. Hence surface tracking capability of the inner side will be slightly higher than the outer side. Detailed drawing of the feed through is shown in figure 6.2.

6.1.2 Pulse forming line

Pulse forming line design is the most critical part of this system. Three different engineering aspects of high voltage compatibility, impedance matching and mechanical durability plays vital role in deciding design constraints. This particular spark gap cum pulse forming line assembly is desired to be operated at a very high pressure of approximately 30 kg/cm^2. High frequency requirements restricts outer diameter of the pulse forming line to as low as 80 mm for 1 GHz compatibility. Interface between pulse forming line, sparkgap and antenna requires, there should be minimum possible impedance variation in the follow through of the pulse. Keeping all these parameters in mind many design iterations were carried out. Simulations are carried out in CST microwave studio to check for compatibility with antenna design. Experts in high pressure handling systems and microwave engineering are consulted for their advice and modifications. Details of electrical, mechanical and microwave engineering design of pulse forming line is narrated in this section.

Theory of operation of pulse forming line is described in detail in chapter 4. In this design, operating principle remains same, only design parameters vary. According to microwave engineering theories to avoid higher order mode generations in transmission line following condition needs to be followed [60].

$$k_c = \frac{2}{r_{PFLo}+r_{PFLi}} \quad (6.1)$$

Where, $r_{PFLo}$and r_{PFLi} are outer and inner radius of pulse forming line. k_c is known as wave number of the line and defined as

$$k_c = \frac{2\pi f\sqrt{\varepsilon_r}}{c} \quad (6.2)$$

Field stress produced at the inner cylinder of the pulse forming line is decided by

$$E_{PFL} = \frac{V}{r_{PFLi}\ln\left(\frac{r_{PFLo}}{r_{PFLi}}\right)} \quad (6.3)$$

Length of the pulse forming is calculated using equation

$$l_{PFL} = \frac{\tau c}{2\sqrt{\varepsilon_r}} \quad (6.4)$$

Impedance of the line was suitably decided to be approximately 100 Ω for antenna compatibility. Characteristics impedance of the line is decided by capacitance and inductance of the coaxial line. Capacitance and inductance of coaxial line is calculated by equation (6.5) and (6.6).

$$C_{PFL} = \frac{2\pi\varepsilon_0\varepsilon_r l_{PFL}}{\ln\left(\frac{r_{PFLo}}{r_{PFLi}}\right)} \tag{6.5}$$

$$L_{PFL} = \frac{\mu l_{PFL}}{2\pi}\ln\left(\frac{r_{PFLo}}{r_{PFLi}}\right) \tag{6.6}$$

ε_r = relative permittivity of dielectric material;

c = velocity of light

Design of the pulse forming line is carried out and converged to match all the equations from (6.1) to (6.6). Teflon has been decided as dielectric material to avoid use of multiple materials to meet high pressure mechanical requirements. Teflon (PTFE) is an excellent high voltage dielectric material with good frequency handling capability vis-à-vis excellent gasket material required for high pressure application. If any other dielectric material would have been chosen, then for mechanical requirement and high pressure gas handling gasket of Teflon (εr = 2.1) or Neoprene (εr = 6.7) would have been required. These materials having different relative permittivity may have caused unwanted discontinuities in the line. To avoid all these complications, Teflon is chosen as dielectric material in the pulse forming line. In this context it should be mentioned that gaseous dielectric also requires solid dielectric in combination for mechanically holding the inner cylinder. This invariably introduces issues of multiple dielectrics. Considering all these constraints following parameters have been converged as an acceptable design from electrical and microwave engineering considerations.

Inner diameter of outer cylinder 80 mm;

Outer diameter of inner cylinder 10 mm

Dielectric material Teflon with relative permittivity 2.1

Active length of the pulse forming line approximately 350 mm

These parameters result in the following acceptable design requirements

$$k_c = \frac{2}{0.04+0.005} = 44.4 \qquad \text{from equation (6.1)}$$

$$f = \frac{k_c\, c}{2\pi\sqrt{\varepsilon_r}} = \frac{44.4 \times 3\times 10^8}{2\pi\sqrt{2.1}} = 1.5 \times 10^9 Hz \qquad \text{From equation (6.2)}$$

Hence, the pulse forming line can suitably discharge faster rise time and pass frequency up to 1.5 GHz limit.

Expected pulse width of the output pulse from equation (6.3)

$$\tau = \frac{2 l_{PFL}\sqrt{\varepsilon_r}}{c} = \frac{2\times 350\times 10^{-3}\times\sqrt{2.1}}{3\times 10^8} = 3.3\ nS$$

In this context it should be mentioned that it is an usual practice to design line of little shorter length to get actual desired pulse width. Due to presence of extra mechanical and geometrical lengths beyond active length of the line pulse width is always longer than analytically calculated value.

Maximum E-field of the line will be produced at the central conductor surface. This is calculated as

$$E_{PFLi} = \frac{V_{PFL}}{r_{PFLi}\ln\left(\frac{r_{PFLo}}{r_{PFLi}}\right)} \tag{6.7}$$

For 1 MV of PFL charging maximum field stress produced at the innermost conductor is 1 MV/cm. Usually Teflon is supposed to handle high E-field of 50-150 MV/m. However these data are stochastic and depends on the thickness of the material, quality of the material and manufacturing process. However in case of application of pulsed field this values are usually much higher. In this case as the structure is radial, whole bulk of the insulator does not see the same stress as observed by the central conductor. Moreover charging of PFL is mostly by triangular or rising co-sinusoidal pulse; hence the occurrence of the extreme peak voltage is of very small time span. In this design, charging pulse is of 30-50 ns time. Hence Teflon is selected as suitable insulator to handle this voltage. Though there were doubt about operation of the experimental set up during application of extreme high voltage, after several experimental shot it has been observed to be in perfect good health and no sign of damage is observed in the soild dielectric of the pulse forming line.

Capacitance and inductance of the line pulse forming line is calculated using equation number (6.5) and (6.6) as 20 pF and 140 nH. Hence, the impedance of the line is approximately 84 Ω. This is reasonably close to 100 Ω antennas for proper matching. Here it should be mentioned that, usually in a line, inductance is little higher than designed values. Hence matched impedance is kept usually on the little higher side to get better matching in practice. However, with this we expect less than 8% voltage reflection and less than 1% energy reflection at the worst.

Mechanical design aspect of the Pulse forming line is another critical parameter. The system is supposed to handle about 40 kg/cm^2 gas pressure of nitrogen and SF_6. Microwave engineering aspect of the design rules out presence of any connecting flange on the load side or antenna side of the line. This is to reduce any impedance variation on the output side of the pulse forming line. Hence, both the electrodes are mounted on different Teflon structure (one ‘U’ shaped and another ‘I’ shaped) and fitted perfectly to each other. Both the structures are connected to the MARX end of the Pulse forming line using suitable flange.

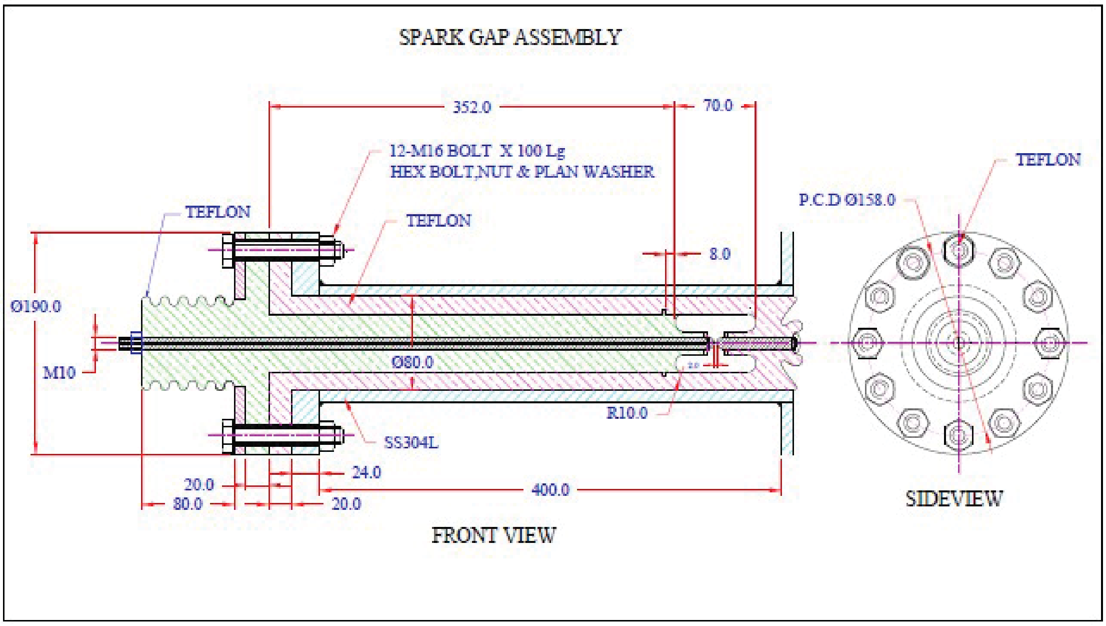

Fig.6.6 Drawing of PFL cum sprakgap assembly

To get pressure tight connection of the innermost conductor in Teflon, metallic structure is thermally cooled, get fitted inside the port of Teflon and bought to normal temperature. This gave excellent mechanical holding to avoid gas leakage. Whole structure is placed inside 1 cm thick SS-304L chamber for mechanical rigidity. Final design drawing and dimensions of the pulse forming line is shown in figure 6.6.

6.1.3 *Radiating antenna*

Half Impulse radiating antenna is used for radiation of UWB pulses in this system. This antenna is a parabolic reflector antenna with a TEM feed. Antenna diameter is approximately 2 m for appropriate electromagnetic field radiation. Two numbers of constant impedance coplanar TEM feed lines are used for feeding the reflector antenna. Impedance of each feed line was 200 Ω. Each feed arm is terminated with a

200 Ω copper sulphate aqueous resistor to provide low frequency impedance matching. Together, they make the antenna impedance close to 100 Ω.

Far field for a Half Impulse radiating antenna is calculated using following formula.

$$E_{far} = \frac{1}{2\pi c r f_g} \frac{D}{4\sqrt{2}} \frac{dV(t)}{dt} \tag{6.8}$$

Where D is antenna diameter, f_g is impedance ratio of antenna impedance Z_c to free space impedance Z_o i.e. $f_g = Z_c/Z_o$, c is velocity of light in free space. $V(t)$ is the applied voltage function at input of antenna.

Feed pulse of the pulse forming line is radiated using this HIRA antenna and radiated far field is measured using TEM sensor. From the measured data arc channel inductance of spark gap under test is estimated. Detail description of measurement methodology and analysis is given in next chapter.

6.2 Conclusion

In this chapter detailed description of the high pressure high voltage experimental set up is discussed. This set up is mainly composed of three major components i.e. MARX generator, Pulse forming line and radiating antenna. MARX generator is capable of generating 1 MV and charges the pulse forming line. Pulse forming line discharges through the sparkgap switch under test and delivers square pulse to the radiating antenna. Radiated E-field is measured using TEM horn sensor to diagnose the rise time of the feed pulse. Detailed description of MARX generator, difficulties constraints and limitations are narrated thoroughly in this chapter. Pulse forming line design is identified as one of the most complicated and challenging part of the design because of its extreme limitations from high voltage engineering, microwave engineering and mechanical engineering point of view. Details of constraints and methodology to mitigate the same have been narrated in this chapter. This experimental setup is used for measurement of arc channel inductance of sparkgaps under high pressure condition. Measurement is carried out in nitrogen and SF_6 atmosphere. Using nitrogen experiments are carried out up to 30 kg/cm^2 and using SF_6 experiments are carried out up to 15 kg/cm^2 pressure. Details of the measurement methodology and results obtained are described in the next chapter.

Chapter 7
Results And Discussion

In this chapter detailed description of the method used for measuring inductance of the sparkgap under very high pressure is elaborated. Variation of inductance with pressure is studied with nitrogen and SF_6 gases by varying pressure from zero to 30 kg/cm^2 and zero to 15 kg/cm^2 respectively. Spark gap inductance along with its arc channel and connecting lead is expected to be in the range of few tens of nano Henrys. Measuring such a low inductance is a challenging task and definitely accuracy of measurement is not very high (error margin ±20%). To make the measurement as reliable as possible several steps are taken and best engineering practices are followed. A PFL transmission line is so designed that it can generate a rise time suitably low for the purpose of the study and can be assumed as an almost step input. Detailed description of the inductance measurement methodology is explained below. In the previous chapter complications of designing pulse forming line is narrated in detail. Introduction of direct measurement methodology i.e. voltage divider etc, at this voltage and pressure level is extremely difficult. Hence indirect radiative method using antenna is used for measurement of rise time and then calculation of inductance. Details of the measurement, observation, typical calculation methodology and conclusive inferences are narrated in this chapter. However, with introduction of indirect measurement method, probability of error in the observed data increases. But results obtained shows a definite pattern in their behavior which corroborates with the simulations. This gives more insight to the physics of arc channel inductance and effective modeling of the same.

7.1 Method of measurement of inductance

As mentioned earlier, design of PFL is extremely difficult due to multiple constraints related to mechanical high pressure, impedance matching and extreme high voltage. It is extremely difficult to provide fast responding potential divider at PFL and load junction for measurement of voltage pulse unlike low voltage experimental set up (mentioned in details in chapter 4). In this experimental setup indirect methodologies are used for measurement of voltage pulse rise time. Output voltage pulse is directly fed at a Half Impulse Radiating Antenna (HIRA) as load. Radiated E-field is measured at 10 m distance using TEM E-field sensor. E field profile at far field nearly equals the rise time of the feeding pulse. Hence near field to far field correction is incorporated in the observation and rise time of the feeding pulse is estimated.

Equation describing E-field value at a certain distance is given by following equation (7.1) [56].

$$E(r,t) = \frac{1}{4\pi r c f_g}\left[\frac{dV(t-\frac{2F}{c}-\frac{r}{c})}{dt} - \frac{C}{2F}\left\{V\left(t-\frac{r}{c}\right) - V(t-\frac{2F}{c}-\frac{r}{c})\right\}\right] \tag{7.1}$$

Where, $fg = Z_{feed}/Z_0$ and F = focal length. Rest all symbols represent their usual meaning. Second part of the equation describes prepulse and vanishes *at* $t = 2F/c + r/c$. first part of the equation starts at $t = 2F/c + r/c$. Though this formula is best suited for far field measurements, still it can be used for reasonably large distance compared to antenna size (2 m diameter). In this experiment, measurements are carried out at 10 m distance from the antenna due to space constraints.

Correction for near field measurement

As described in the previous section, far field measurement of E-field is representative of rise time of the feed pulse. Hence to measure the spark gap inductance, FWHM (Full Width Half Maxima) of radiated far field can be used. Far field of an UWB HIRA antenna is defined by the following equation (7.2). In this particular set up far field is at approximately 90 meter from the antenna.

$$r_{FAR} = \frac{2D^2}{ct_r} \tag{7.2}$$

Where, D is diameter of the radiating antenna and t_r is the rise time of the feed pulse. Hence measurement must be carried out beyond 90 meter from the antenna. This is little difficult considering practical constraints of the present Lab size. Hence near field measurement of E-field is carried out and far field pulse width of the E-field is calculated by introducing correction factor.

E-field at a distance *'r'* can be defined by the equation (7.3)

$$E(r,t) = \frac{1}{2\pi f_g}\left[\left\{\frac{V\left(t-\frac{r}{c}\right)}{r}\frac{\sin\beta}{1+\cos\beta} - \frac{V\left(t-\frac{l}{c}-\frac{r_2}{c}\right)}{r}\frac{\sin\beta+\sin\gamma}{1+\cos(\beta-\gamma)}\right\} - \left\{\frac{4V(t-\frac{2F}{c}-\frac{r}{c})}{D} - (2+2\cos\gamma)\frac{V(t-\frac{l}{c}-\frac{r_2}{c})}{D}\right\}\right] \tag{7.3}$$

If *'r'* is high compared to antenna size, first two terms reduce to negligible. These are terms responsible for prepulse. Radiated E- field is mainly function of last two terms. Again at high *'r'* value

$$r_2 + l = r + 2F + \frac{D^2}{8a} \tag{7.4}$$

Hence equation (7.1) reduces to

$$E(r,t) = \frac{1}{2\pi f_g}\left[\frac{1}{D}\begin{Bmatrix} 4V\left(t-\frac{2F}{c}-\frac{r}{c}\right)- \\ (2+2\cos\gamma)V(t-\frac{2F}{c}-\frac{r}{c}-\frac{D^2}{8ac}) \end{Bmatrix}\right] \quad (7.5)$$

Moreover from the geometry shown in figure (7.1) angle γ tends to zero as r increases and hence *cos(γ)* tends to 1. Therefore equation (7.5) further reduces to

$$E(r,t) = \frac{1}{2\pi f_g}\left[\frac{4}{D}\left\{V(t-\frac{2F}{c}-\frac{r}{c}) - V(t-\frac{2F}{c}-\frac{r}{c}-\frac{D^2}{8ac})\right\}\right] \quad (7.6)$$

If we assume

$t-\frac{2F}{c}-\frac{r}{c} = t_1$ and $\frac{D^2}{8ac} = \Delta t$ then equation (7.6) can be represented as

$$E(r,t) = \frac{1}{2\pi f_g}\left[\frac{4}{D}\{V(t_1) - V(t_1-\Delta t)\}\right] \quad (7.7)$$

If *'r'* is very high from the geometry *'a'* is very high and *Δt* is very small. Hence equation (7.7) reduces to

$$E(r,t) = \frac{1}{2\pi f_g}\left[\frac{4}{D}\left\{V(t_1) - V(t_1) + \frac{dV}{dt}\Delta t\right\}\right] = \frac{4}{2\pi D f_g}\Delta t\frac{dV}{dt} \quad (7.8)$$

Putting the value of *Δt* in the equation we get

$$E(r,t) = \frac{D}{4\pi f_g ac}\frac{dV}{dt} \quad (7.9)$$

Hence, it can be said that if a square pulse is fed to HIRA antenna E field at a long distance will be proportional to *dV/dt* and as in square pulse significant *dV/dt* is obtained during rising and falling portion of the pulse, significant E-field will be observed during that period only. However in this study we are mostly concerned about rising part of the pulse and corresponding first E-field peak only. And in practice FWHM of the E-field will be almost equal to the rise time of the square pulse. But in this calculation it is very critical to understand what should be considered as sufficiently long distance or what can be suitably considered as large 'r'.

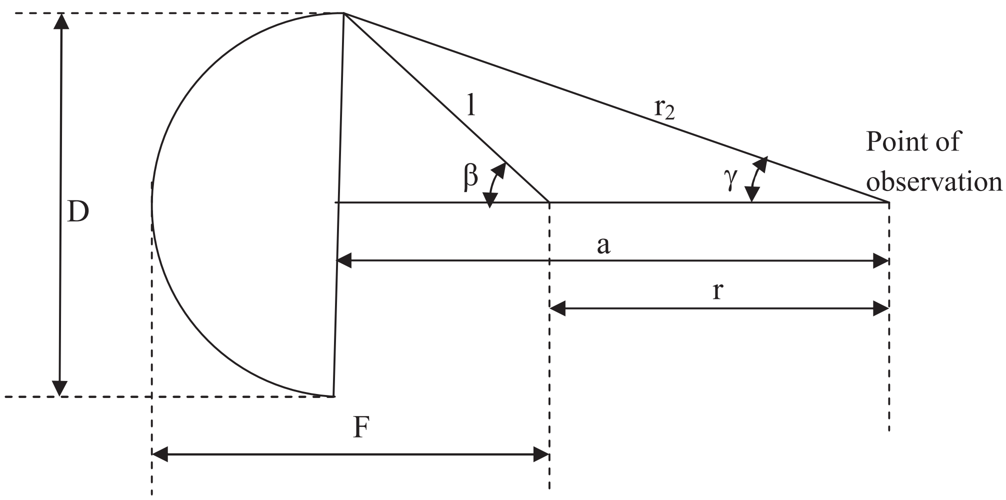

Fig.7.1 Drawing of IRA antenna showing dimensional parameters

In the calculation shown above, one of the most important assumptions is $\frac{D^2}{8ac} = \Delta t$.

This comes from the geometry of the antenna shown above. This suggests the time difference between two propagating waves towards the point of observation. One from reflector and other from the point feed is connected in the antenna. Hence actual expression of Δt can be written as

$$\Delta t = \frac{\sqrt{\left(\frac{D}{2}\right)^2 + a^2} - a}{c} \tag{7.10}$$

At a condition when ‘a’ is much much higher than *‘D’*, then equation (7.10) reduces to $\frac{D^2}{8ac} = \Delta t$. This is possible at an extremely large value of *‘r’*. So for all practical purposes, it is better to check for distortion in the pulse width and suitable corrections must be incorporated in the measurement. In our experimental set up *‘r’* is equal to 10 m and *‘D’* is equal to 2 m. Calculations are carried out for pulse width at 10 m and at a very high value of *‘r’* i.e. 100 m to find difference in FWHM of the E-field. Difference between the FWHM of both has been taken as a correction factor in the measurement. Correction factor is calculated analytically using formula given in equation (7.1) [15]. Figure 7.2 shows analytically calculated E-field at 10 m distance using equation (7.1) for a square pulse.

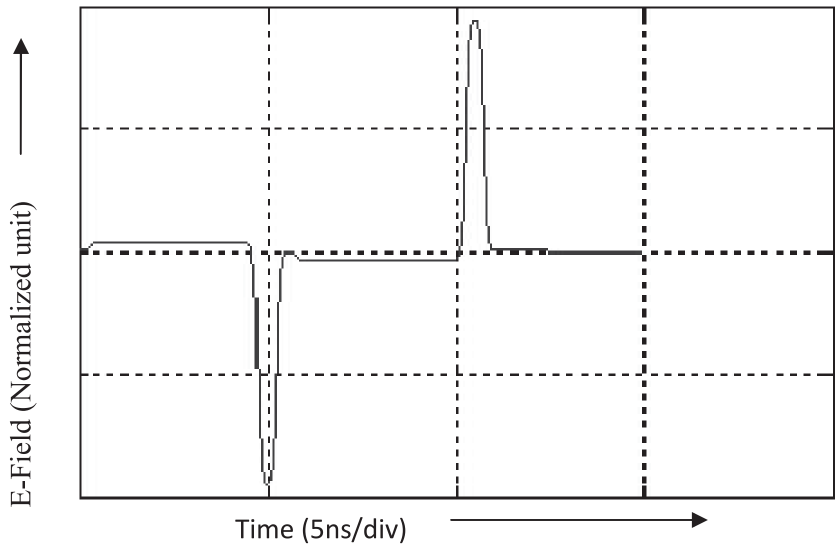

Fig.7.2 Analytically calculated radiated field at 10m distance

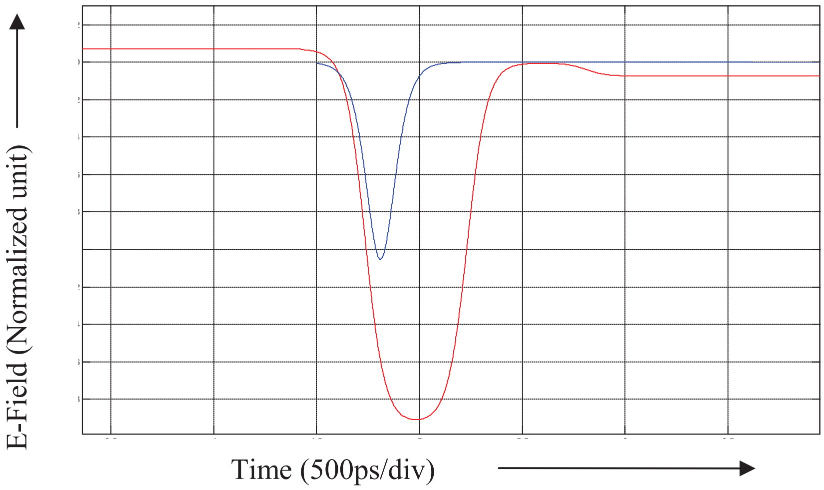

Fig.7.3 400ps correction factor in FWHM introduced due to near field measurement

Figure 7.3 shows pulse width difference between E-field measured at 10m distance (red) and at far field (black). Rise time of the fed pulse is calculated from obtained rise time data at different pressure of nitrogen and SF_6 gas and applying correction factor to it.

Here it should be noted that impulse radiating antenna (IRA) basically behaves as a differentiator. If a square pulse is fed to the antenna input, a bipolar radiating E-field is observed at far-field. If measurements are carried out at near field location, radiated fields show higher FWHM. Formula shown in equation (7.1) explains the same and can be suitably used to find out far field FWHM from near field FWHM. Far field FWHM of radiated E-field pulse is almost equal to rise time (10%-90%) of the feeding pulse. In this experiment near field radiated E-field is measured using antenna. Far field FWHM is calculated using analytical relations and rise time of the fed pulse is calculated from far field FWHM. In our experimental set up Half Impulse Radiating Antenna (HIRA) is used.

7.2 Finding inductance from rise time

In the previous section it has been discussed how to measure rise time of the feed pulse from the radiated E-field measurement. In this section methodology to find out inductance of sparkgap from the rise time of the pulse is discussed. Similar calculations have been carried out in chapter 5 to find out inductance of arc channel from measured rise time of the feed pulse. Please refer to equation (5.7) to find out inductance of arc channel. But in equation (5.7), time span between 80% of final value to 90% of final value is used for calculating inductance of arc channel. Here in this measurement method of radiated E-field we only have time span between 10% of final value to 90% of final value. Hence the formula given in equation (5.7) cannot be used directly. A relation between rise time (10%-90%) and rise time (80%-90%) has to be worked out. Here it must be reiterated that rise time of the feed pulse is observed not to follow exponential pattern rather a different curve which approaches exponential rising towards final value. Please refer to figure 5.3 where this effect is discussed in detail. Actually this rising curve follows pattern mentioned in equation (5.7).

$$V_{L1}(t) = \left. \frac{V}{2}[1-u(t-2\delta)]\left[1-e^{-\frac{2Z_L t}{L}}\right] \middle/ \left[1+\left(\frac{R_{SO}}{Z_0+Z_L}\right)e^{-\frac{t}{\tau_1}}\right] \right. \tag{7.11}$$

A relation between rise time (10%-90%) and rise time (80%-90%) of this curve needs to be derived to further approach the estimation.

If the time required for 10% of final value is defined as $t_{0.1}$, 80% of final value is defined as $t_{0.8}$ and 90% of final value is defined as $t_{0.9}$, then following parameters can be defined from equation (7.10)

$$V_{L1}(t_{0.1}) = \frac{\frac{V}{2}\left[1-e^{-\frac{t_{0.1}}{\tau}}\right]}{\left[1+\left(\frac{R_{SO}}{Z_0+Z_L}\right)e^{-\frac{t_{0.1}}{\tau_1}}\right]} = 0.1\frac{V}{2} \qquad (7.12)$$

As described in chapter 4 that this phenomenon (rise time following S-curve rather than exponential curve) is predominant because of the very fact that time constant of sparkgap closing i.e. τ_1 and time constant of feed pulse rising i.e. τ are comparable. Hence assuming $\tau_1 = \tau$ equation (7.11) can be written as

$$V_{L1}(t_{0.1}) = \frac{\frac{V}{2}\left[1-e^{-\frac{t_{0.1}}{\tau}}\right]}{\left[1+\left(\frac{R_{SO}}{Z_0+Z_L}\right)e^{-\frac{t_{0.1}}{\tau}}\right]} = 0.1\frac{V}{2} \qquad (7.13)$$

As at 10% of final value $\left(\frac{R_{SO}}{Z_0+Z_L}\right)e^{-\frac{t_{0.1}}{\tau}} \gg 1$, hence equation (7.13) can reasonably be approximated as

$$\frac{\frac{V}{2}}{\left[\left(\frac{R_{SO}}{Z_0+Z_L}\right)e^{-\frac{t_{0.1}}{\tau}}\right]} = 0.1\frac{V}{2} \qquad (7.14)$$

Or $\left[\left(\frac{R_{SO}}{Z_0+Z_L}\right)e^{-\frac{t_{0.1}}{\tau}}\right] = 10$ (7.15)

After doing mathematical manipulations we can write

$$t_{0.1} = \tau \ln\left(\frac{0.1R_{SO}}{Z_0+Z_L}\right) \qquad (7.16)$$

While approaching the final value, equation (7.11) becomes of exponentially rising pattern and $t_{0.8}$ and $t_{0.9}$ can reasonably be written as

$$t_{0.8} = -\tau \ln(0.2) = 1.61\tau \qquad (7.17)$$

And

$$t_{0.9} = -\tau \ln(0.1) = 2.3\tau \qquad (7.18)$$

Please refer to figure 5.3 , figure shows that experimental waveform matches more closely with S-curve which on approaching the final value matches with exponentially rising curve. But the exponentially rising curve with which S-curve matches remains zero shifted. This zero shift is defined here as t_{drift} which is calculated below.

Assuming the zero shift to be equal to *'α'* it can be written that

$$V_{L1}(t) = \frac{\frac{V}{2}\left[1 - e^{-\frac{t}{\tau}}\right]}{\left[1 + \left(\frac{R_{SO}}{Z_0+Z_L}\right) e^{-\frac{t}{\tau}}\right]} = \frac{V}{2}\left[1 - e^{-\frac{(t-\alpha)}{\tau}}\right] \qquad (7.19)$$

Or,

$$\left[1 - e^{-\frac{t}{\tau}}\right] = \left[1 - e^{-\frac{(t-\alpha)}{\tau}}\right]\left[1 + \left(\frac{R_{SO}}{Z_0+Z_L}\right) e^{-\frac{t}{\tau}}\right]$$

Or,

$$\left[1 - e^{-\frac{t}{\tau}}\right] = \left[1 - e^{-\frac{(t-\alpha)}{\tau}} + \left(\frac{R_{SO}}{Z_0+Z_L}\right) e^{-\frac{t}{\tau}} - \left(\frac{R_{SO}}{Z_0+Z_L}\right) e^{-\frac{(t-\alpha/2)}{\tau/2}}\right] \qquad (7.20)$$

Neglecting the terms having lower time constant it can be written

$$e^{-\frac{t}{\tau}}\left(1+\left(\frac{R_{SO}}{Z_0+Z_L}\right)\right) = e^{-\frac{(t-\alpha)}{\tau}} \tag{7.21}$$

Therefore,

$$\alpha = \tau \ln\left(1+\left(\frac{R_{SO}}{Z_0+Z_L}\right)\right) \approx \tau \ln\left(\frac{R_{SO}}{Z_0+Z_L}\right) \tag{7.22}$$

Hence by using equation (7.16), (7.17) ,(7.18) and (7.22) it can be written that for this particular profile

$$\frac{(t_{0.9}-t_{0.8})}{(t_{0.9}-t_{0.1})} = \frac{(2.3\tau-1.61\ \ )}{\left(2.3\tau-\tau\,l\ \left(\frac{0.1R_{SO}}{Z_0+Z_L}\right)+t_{drift}\right)} = \frac{.69}{\left(2.3-\ln\left(\frac{0.1R_{SO}}{Z_0+Z_L}\right)+\ln\left(\frac{R_{SO}}{Z_0+Z_L}\right)\right)} \tag{7.23}$$

Assuming spark gap open circuit impedance is higher than the combined impedance of load and line, equation (7.23) reduces to

$$\frac{(t_{0.9}-t_{0.8})}{(t_{0.9}-t_{0.1})} = \frac{.69}{(2.3+2.19)} = 0.15 \tag{7.24}$$

Therefore, combining equation (5.7) and (7.24) inductance of arc channel can be written as

$$L = \frac{Z_L(t_{0.9}-t_{0.8})}{0.345} = \frac{0.15Z_L(t_{0.9}-t_{0.1})}{0.345} = \frac{Z_L(t_{0.9}-t_{0.1})}{2.2} \tag{7.25}$$

Here it must be mentioned that actually spark gap open circuit resistance is much much higher than that of load impedance and line impedance, which are in the range of 100 Ω. However, at the instant of this calculation sparkgap resistance must be about an order higher than combined impedance of load and line to ensure output voltage. Otherwise all the voltage will be consumed across the sparkgap resistance only.

This mathematical identity is validated using actual data curve shown in figure 5.3

From the curve in figure 5.3, 10% of final value is achieved at 380 ps, 80% of final value is achieved at 785 ps s & 90% of final value is achieved at 860 ps. Now inductance value calculated using 80% to 90% final value data and equation (5.7) we get

$$L = \frac{Z_L(t_{0.9} - t_{0.8})}{0.345} = \frac{60 \times (860 - 7 \quad) \times 10^{-1}}{.345} = 13\ nH \tag{7.26}$$

If the same inductance is calculated using 10%-90% final value data and using equation (7.25), we get

$$L = \frac{Z_L(t_{0.9} - t_{0.1})}{2.2} = \frac{60 \times (860 - 3 \quad) \times 10^{-12}}{2.2} = 12.5\ nH \tag{7.27}$$

Both the values obtained from equation (7.26) and (7.27) are in close agreement. Therefore, using this method henceforth arc channel inductance is derived from 10%-90% of final value of a rising curve which mostly resembles S-curve pattern.

7.3 Simulation of experimental set up

To verify the expected operation and measurement methodology simulation is carried out in CST microwave studio. Pulse forming line feeding the antenna is simulated together in its true dimension. Simulated far field is measured using E-probe. Result obtained from measurement corroborates with the rise time of the pulse feeding antenna. This validates the measurement methodology of rise time of the feeding voltage pulse. In figure 7.4 simulation structure is shown. Figure 7.5 shows the voltage appearing across antenna feed and figure 7.6 shows the far field corresponding to the same voltage pulse. In the figure it can be seen that rise time of the feed pulse is almost equal to FWHM of the measured E-field in far-field region.

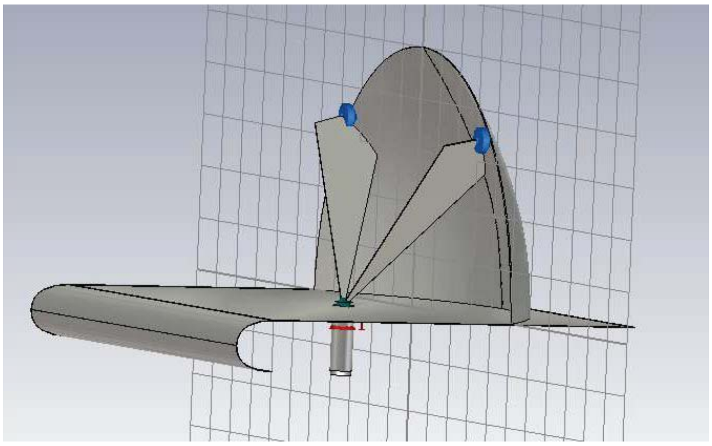

Fig.7.4 Simulated model of experimental setup

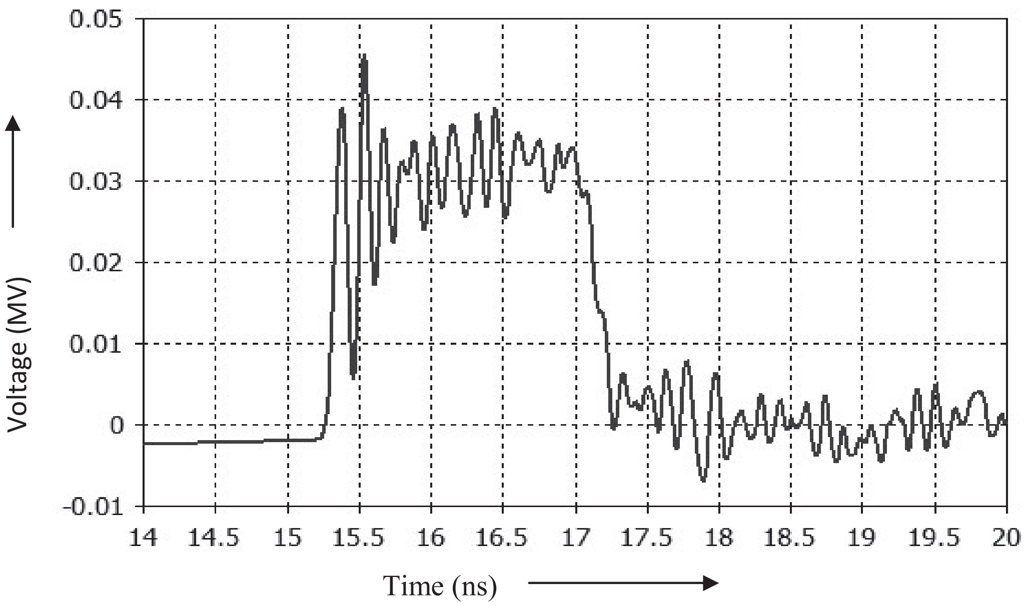

Fig.7.5 Simulated voltage feed to the antenna

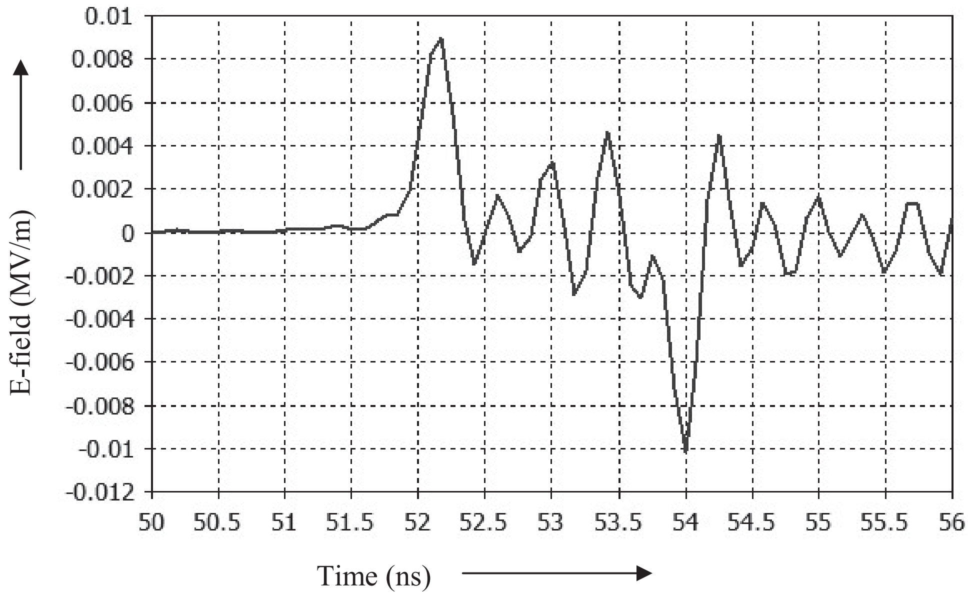

Fig.7.6 Simulated pattern of radiated far field

7.5 Typical example of inductance calculation for 2 mm gap

Measured radiated waveform at 10 m distance is shown in figure 7.7. FWHM of the measured E-field is 625 ps. Applying near field to far field pulse width correction of 400 ps, FWHM of the radiated far field is approximately 225 ps. This FWHM of far field radiated E-field is almost equal to 10%-90% rise time of the feed voltage at the antenna feed. PFL impedance is 83 Ω and antenna impedance is 100Ω. Therefore, applying the equation (7.26)

$$L = \frac{(Z_L + Z_0)(t_{0.9} - t_{0.1})}{2 \times 2.2} = 9.4 \times 10^{-9} \quad (7.28)$$

We get the inductance of spark gap equal to 9.4 nH. This is a typical example of arc channel inductance measurement in high pressure experimental set up. Experiments and studies are carried out in this set up using nitrogen and SF_6 as gas medium at different pressure. Results and analysis of those experiments are narrated in the following sections.

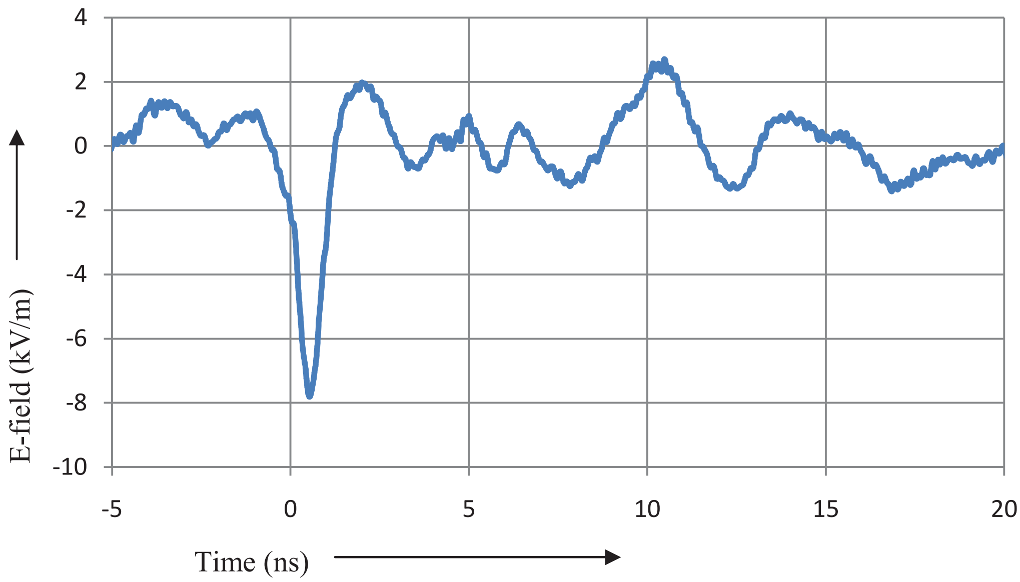

Fig.7.7 Measured E-field at 10m distance

7.6 Inductance variation study with gas pressure

Variation of inductance of arc channel is studied at different gas pressure. For nitrogen gas medium pressure is varied from atmospheric pressure to 30 kg/cm^2. In case of SF_6 gas medium pressure is varied from atmospheric to 15 kg/cm^2. Inductance is measured for 2 mm gap between electrodes. Results obtained are plotted in figure.7.10 and 7.11. Simulated results to find arc channel inductances at similar condition are plotted in the figure 7.8 and figure 7.9.

Experiment with different gases i.e. N_2 (elemental) and SF_6 (compound) shows that, gases with lower molecular weight (i.e. nitrogen) give less inductance compared to gases of higher molecular weight (i.e. SF_6). With increment of pressure, inductance increases in both the gases. This is explained by same kernel theory described in earlier sections. With increase of molecular weight and pressure energy requirement for ionizing gaseous kernel increases. With increase of gas pressure, number of gas molecule present in a certain volume increases. Mean free path of the free electrons also reduce with increase of pressure. As a result of which energy of the striking electrons reduces and probability of secondary ionization reduces. Attributed by all these factors finally we observe a thinner arc channel in high pressure gas medium. In case of molecules like SF_6 which is having high molecular weight and a natural tendency to adsorb free electrons consumes lot of energy and free electron in secondary ionization. As a result of which thinner kernels are found. Experiments show that if gas pressure of nitrogen is increased from 2 kg/cm^2 to 30 kg/cm^2 inductance of sparkgap under test varies from 6 nH to 10 nH (Approximately). In case of SF_6 gas medium experiments are conducted from 2 kg/cm^2 to 15 kg/cm^2. Results show a variation of inductance from 8 nH to 12 nH. Simulations with similar parameters show a little lower rate of increment (i.e. 3.2 nH to 3.4 nH in N_2 medium and 3.5 nH to 4.5 nH in SF_6 medium). This is attributed to imperfections in the experiment, measurement and assumptions in simulation carried out. Never the less they agree in their range of variation, trend of variation and relative magnitudes. In practical experiment, extra inductance is expected due to presence of leads that connects the sparkgap, discontinuity due to mechanical arrangements and probability of radial offset in the formation of arc channel. More over measurements are done indirectly from radiated waveforms in near field which incorporates extra error in the measured value of inductances. Moreover calculations of arc channel inductance from raw data involve lot of assumption. Variation in simulated and measured inductance values are mostly attributed to those factors.

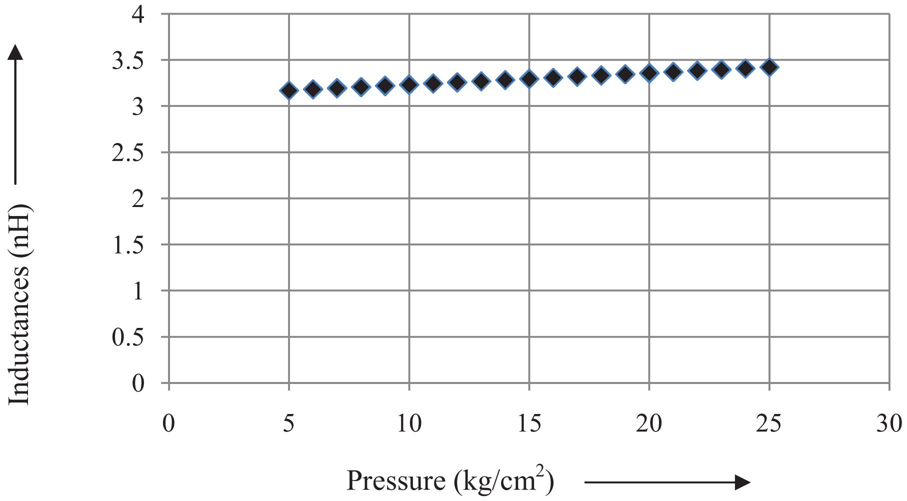

Fig.7.8 Simulated result of variation of inductance in N_2 medium

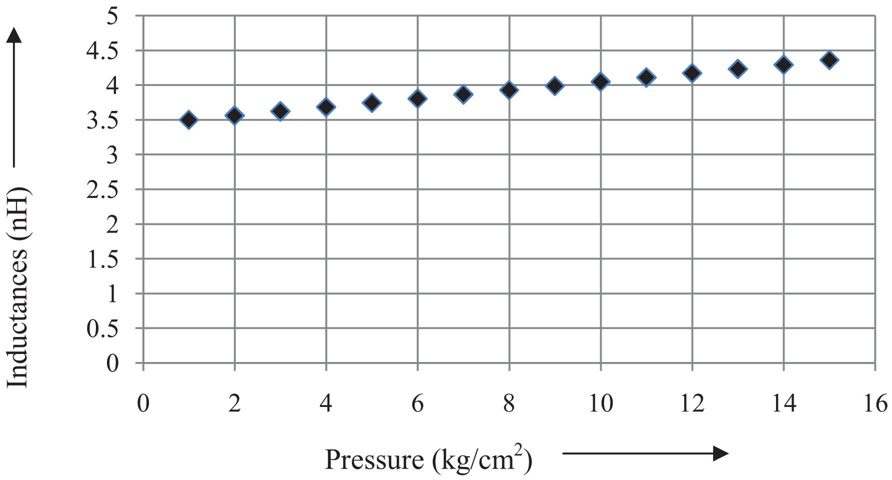

Fig.7.9 Simulated result of variation of inductance in SF_6 medium

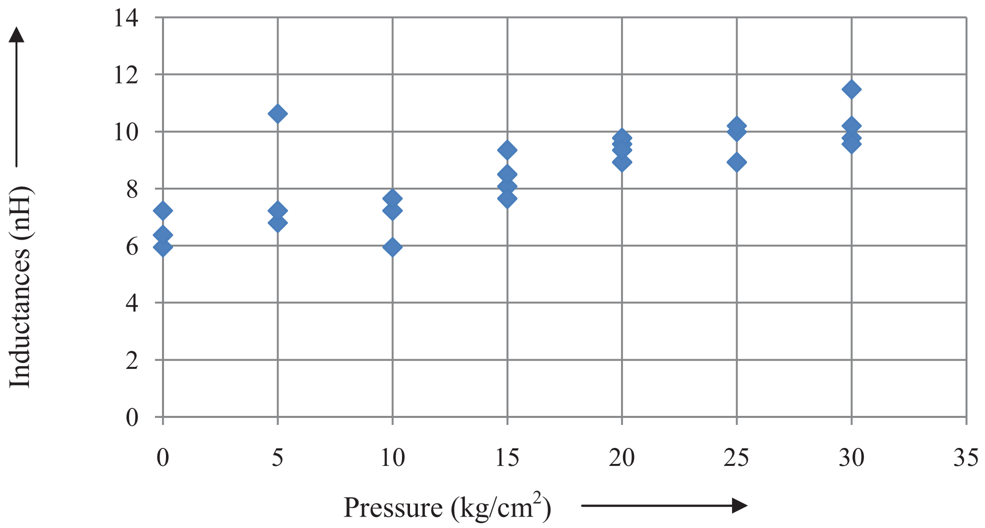

Fig.7.10 Experimental result of variation of inductance in N_2 medium

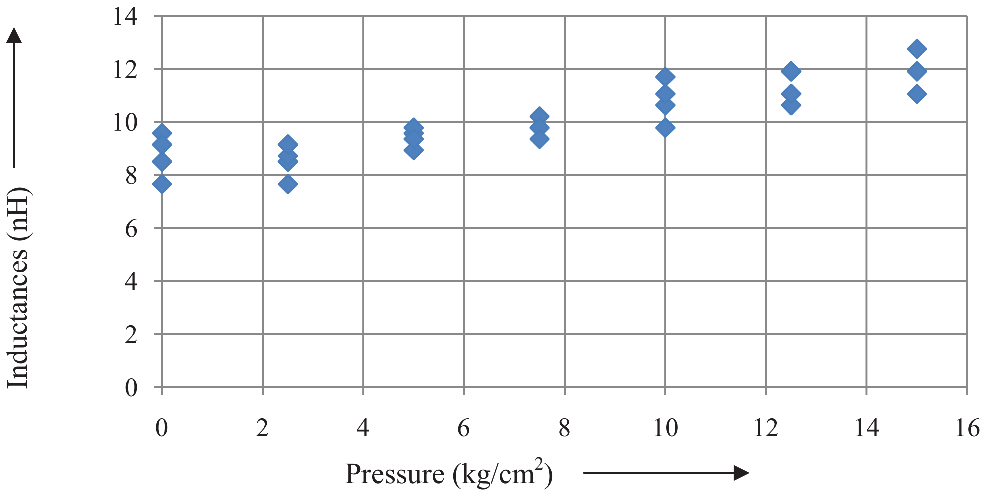

Fig.7.11 Experimental result of variation of inductance in SF_6 medium

The set up developed for experimental purpose can be suitably used for experiment on electronic susceptibility. Whole system is mounted on wheels for portability, weighs nearly 300 kg and occupies floor area of approximately 2m X 2m. This system can be truck mounted and carried to places for experimental purpose. In house susceptibility experiments are conducted using this system. Intel core-to quad processor based computers are found to get affected at a field of approximately 8-10 kV/m and 10-20 Hz repetition rate. Such fields are generated using this system at a maximum distance of approximately 20m. Several experiments are carried out using this system to disrupt a running computer from approximately 20m distance.

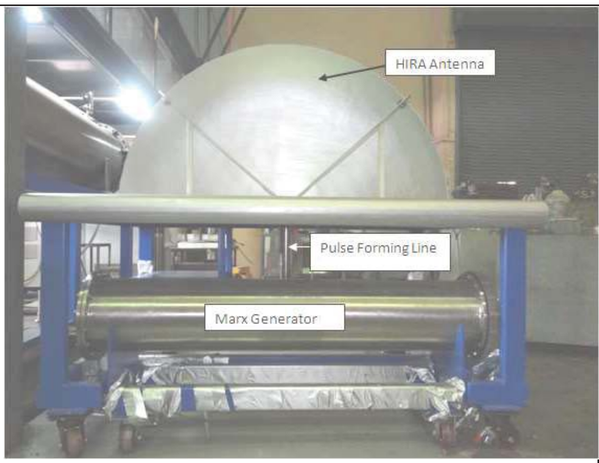

Fig.7.12 Photograph of 1 MV UWB setup

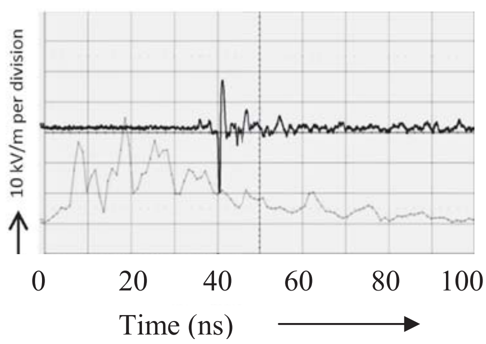

Fig.7.13 Electric field signal(20 kV/m) and FFT at 10 m distance from source

7.7 Conclusion

Results obtained in the experiment are found to be a little higher than anticipated in simulation. The difference in simulation and experimentally measured waveform is in the range of 5-6 nH. This may be due to presence of stray inductance in the circuit connecting PFL output with antenna. Moreover, this measurement is not a direct measurement of inductance via pulse rise time. In this experiment, measurement of inductance is carried out indirectly via measurement of radiated field and its pulse width. This potentially introduces more error in the measurement due to probable presence of many unquantifiable factors. Gain of the UWB radiating antenna, insertion losses etc. are not exactly constant for the whole range of radiating frequencies. These factors introduce measurement errors and variation in experimentally measured inductance and simulated inductances. Further attempt may be conducted to accurate the measurement of these inductances to get closer a match.

Never the less experiment validates the simulated inference that with pressure inductance of arc channel increases and SF_6 medium offers higher inductance compared to N_2 medium at any constant pressure of operation.

Chapter 8
Conclusions and Future scope

During the course of thesis works following important conclusions are drawn and elaborated below

1. A computer code has been developed to estimate inductance of arc channel inductance of a sparkgap with variation of gas medium (i.e. Nitrogen, SF_6), variation of gas pressure and gap between electrodes. This is a generic code and can be used for estimation of sparkgap inductance extensively for other applications also. With minor modifications this code can be extended suitably for other gases like argon, helium, hydrogen etc.

2. It has been found from simulation and verified using experimentation that spark gap arc channel inductance is a function of gap between electrodes, gas pressure and gas property. Inductance of arc channel inductance increases with gaps between electrodes and pressure of the gas medium. It is also found that inductance of arc channel is less in nitrogen (lower molecular weight) compared to SF_6 (higher molecular weight) for same gas pressure and gap between electrodes [section 7.4].

3. V-I characteristics of gas discharge has been simulated using the same computer code. Simulated profile categorically exhibits normal glow discharge region, abnormal glow discharge region and arc discharge region.

4. Design, simulation and development of 200-500 kV, 300 ps (rise time), 5 ns pulsar has been carried out. A maximum radiating field 10 kV/m at 20 m distance has been measured using conical horn antenna.

During the research work two experimental setups were designed and developed (i) 250 kV pulser for preliminary studies at moderate pressure up to 5 kg/cm^2, and (ii) 1 MV pulser with high pressure capacity up to 40 kg/cm2 for output switch. From experiments and computational analysis it has been found that applications of high pressure gas switches with extremely small gap between electrodes, are most suitable for UWB applications. In this research work high pressure gas sparkgap switch has been analyzed and effect of gap distance, gas pressure and gas property were studied. Simulation of sparkgap inductance and arc channel also has been carried out and validated with the experimental results.

Present thesis work can be extended to study the effects of different other types of gases and liquid dielectric medium used in spark gap switches. It is believed that, hydrogen gas can be of good use as gas medium, for high pressure high voltage applications. This is because of its very low molecular weight and capacity to handle very high pressure without getting liquefied. But handling inflammable hydrogen gas at such high pressure and high voltage application is hazardous. Suitable precautions are required to be taken for experiments with hydrogen. Multi channeling of spark gap switches can reduce inductance significantly. Future study in this direction will be very useful in further reduction of rise time of high voltage pulse. Susceptibility of different modern day electronics ICs and digital gates can be studied using such UWB systems.

CONTENTS

REFERENCES

1. William D. Prather, "Ultra-Wideband Source and Antenna Research", *IEEE Transactions on Plasma Science*, vol. 28, no. 5, October 2000.
2. William D. Prather, "Survey of Worldwide High-Power Wideband Capabilities", *IEEE Transactions on Electromagnetic Compatibility*, vol. 46, no. 3, august 2004
3. Y. Yankelevich, A. Pokryvailo, and M. Shapira,"A compact source of sub-GW, subnanosecond pulses" , in *Proc. 14th IEEE Int. Pulsed Power Conf.*, Dallas, TX, June 2003.
4. M. I. Yalandin and V. G. Shpak, "Compact High-Power Subnanosecond Repetitive-Pulse Generators(Review)" in *Instruments and Experimental Techniques*, Vol. 44, No. 3, 2001, pp. 285–310.
5. Zheltov, K.A., "Picosecond High-Current Electron Accelerators", in *Proc. of Energoatomizdat* Moscow, 1991.
6. Morugin, L.A. and Glebovich, G.V., "Nanosecond Pulsed Technique", in *Sovetskoe Radio* Moscow, 1964.
7. F. Olsson,W. E. Edbom, G. Filipsson, M. Karlsson, S.E. Wiippa, S. hansson and B.O. Bergman, "Experiments And Simulations of A Compact UWB Pulse Generator Coupled to Different Antenna Structures", in *Proc. IEEE Conference on Pulsed Power*, pp 1310-1313, 2005.
8. F. Olsson, M. Larbi, M. Karlsson, H. Christensen, G. Filipsson, and B.O. Bergman, "Experiments and Simulations of a Compact UWB Pulse Generator Coupled to an Exponential Flared TEM-Homn Antenna", in *Proc. IEEE Power Modular Symposium*, pp 153-156, 2006.
9. C. E. Baum,"The dispatcher: a new mesoband, high-power radiator,"in *Proc. URSI General Assembly*, Maastricht, The Netherlands, 2002.

10. J. W. Burger, C. E. Baum, W. D. Prather, R. J. Torres, T. C. Tran, M. D. Abdalla, M. C. Skipper, B. C. Cockreham, and D. R. Mclemore,"Design and development of a high voltage, coaxial hydrogen switch", in *Ultra Wideband/Short-Pulse Electromagnetics 6*, New York: Plenum, 2003

11. L. H. Bowen, L. M. Atchley, E. G. Farr, D. E. Ellibee, W. J. Carey, J. R.Mayes, and L. L. Altgilbers, "A prototype high-voltage UWB transmitter", in *Sensor and Simulation Note 473*, Air Force Res. Lab., Kirtland AFB, NM, Mar. 2003.

12. C. E. Baum William L. Baker, William D. Prather, Jane M. Lehr, James P. O'loughlin, D. V. Giri, Ian D. Smith, Robert Altes, James Fockler, Donald Mclemore, Michael D. Abdalla And Michael C. Skipper, "JOLT: A highly directive, very intensive, impulse-like radiator", in Sensor and Simulation Note 480, Nov. 10, 2003.

13. J. S. H. Schoenberg, J. S. Tyo, J. W. Burger, M. D. Abdalla, and M.C. Skipper,"A linear array of ultra-wideband radiators driven by photoconductive, semiconductor-switched blumleins," in *Ultra-Wideband,Short-Pulse Electromagnetics 4*, NewYork: Plenum, 1999.

14. Zhenru Gao, Huichang Zhao, Youchao Tu, Xiang Fang, Xingang Zhou, and Jing Liu, "Study on the Ultra-Wide Band High Power Microwave Coupling Effect on Electronic Fuze System", in *Proc. Automation Congress in Hawai,*pp 1-4, Sept,2008.

15. Oleg V. Mikheev and Stanislav A. Podosenov "New Method for Calculating Pulse Radiation from an Antenna With a Reflector", *IEEE Transactions on Electromagnetic Compatibility*, Vol. 39, No. 1, February 1997.

16. Pecastaing, L.; Cadilhon, B.; Reess, T.; De Ferron, A.; Pignolet, P.; Vauchamp, S.; Andrieu, J.; Lalande, M.; Brasile, J.P, "A 250KV-300PS-350HZ Marx Generator As Source For an UWB Radiation System", *in Proc. IEEE Pulsed Power Conference*, 2009.

17. Cadilhon, B.; Cassany, B.; Modin, P.; de Ferron, A.S., "Repetitive Auto-Triggered Marx Generator as the Driver of an Ultra wide band Source"; *in Proc. Pulsed Power Conference*, 2009.

18. P. Sarkar, S.W. Braidwoody, I. R. Smith4, B. M. Novac, R. A. Miller and R. M. Craven, "A Compact Battery-Powered 500kV Pulse Generator For UWB Radiation", in *Proc. IEEE Pulsed Power Conf.*, pp.1306-1309,2005.

19. D. Goerz, T. Ferriera, D. Nelson, R. Speer, M. Wilson, "An Ultra-Compact Marx-Type High-Voltage Generator" in *Proc. IEEE Pulsed Power Plasma Science*, pp.628-631, 2001.

20. Jon S. H. Schoenberg, Member, IEEE, Jeffrey W. Burger, J. Scott Tyo, Member, IEEE,Michael D. Abdalla, "Ultra-Wideband Source Using Gallium Arsenide Photoconductive Semiconductor Switches", *IEEE Transaction on Plasma Science*, pp.327-334, 1997.

21. Yu.A. Andreev, V.P. Gubanov, A.M. Efremov, V.I. Koshelev', S.D. Korovin, B.M. Kovalchuk, V.V. Kremnev, V.V. Plisko, A.S. Stepchenko, K.N. Sukhushin, "High-Power Ultra-wideband Electromagnetic Pulse Source" in *Proc. IEEE Pulsed Power Conf.*pp.1458-1461,2003.

22. B.Han, M.Han, "Computational Simulation of the Time Dependent Resistance and Inductance of a Field Distortion Spark Gap" in *Proc. IEEE pulsed Power Plasma Science*, pp. 1762 – 1765, 2001.

23. Kim A. A., Kovalchuk B. M., Kremnev V. V., Kumpjak E. V., Novikov A. A, "Multi Gap, Multi Channel Spark Switches", in *Proc. of IEEE Pulsed Power Conf.* pp. 862 – 867,1997.

24. Kimura, W. D.; Kushner, M. J.; Seamans, J. F., "Characteristics of a laser triggered spark gap using air, Ar, CH4, H2, He, N2, SF6, and Xe", *Journal of Applied Physics* Volume: 63 , Issue: 6.

25. J.M. Lehr, C.E. Bauim, W.D. Prather and F. J. Agee "Aspects of Ultrafast Spark Gap Switching for UWB HPM Generation" in *Proc. of Pulsed Power Conf.* pp. 1033 – 1041,1997.

26. T. E. James, "High-Current 60 KV Multiple-Arc Spark-Gap Switch Of 1-7 nH Inductance", in *Proc. of the Institution of Electrical Engineers*,Volume: 117, Issue: 7

27. H. C. Harjes, E. E. Kunhardt, M. Kristiansen, L. L. Hatfield And A. H. Guenther "Space-Charge Effects in a Laser Fiber-Optics Triggered Multichannel Spark Gap", *IEEE Transaction on Plasma Science.* Vol 10, 1982

28. Xinxin Wang; Haiyun Luo; Yuan Hu, "Numerical Simulation of the Gas Discharge in a Gas Peaking Switch", *IEEE Transactions on Plasma Science,* Volume: 35.

29. Khan, S.H.; Walsh, D.; "Effect Of Various Gases On Formative Times Of Laser-Triggered Spark Gap", in *Electronics Letters* Volume: 6 , Issue: 17

30. Guenther, A.H.; Bettis, J.R. "A Review Of Laser-Triggered Switching"; in *Proceedings of the IEEE* Volume: 59 , Issue: 4 pp. 689 – 697, 1971.

31. MacGregor, S. J.; Timoshkin, I. V.; Given, M. J.; Fouracre, R. A.; Lehr, J. M.; Warne, L. K. "Sub-Nanosecond Jitter High Voltage Spark-Gap Triggered By Femtosecond Laser Pulses"*;in Pulsed Power Conference*, 2007.

32. J.M. Lehr, C.E. Bauim, W.D. Prather and F. J. Agee. "Aspects Of Ultrafast Spark Gap Switching For UWB HPM Generation", in *Proc. IEEE Pulsed Power Conf.* pp. 1033 – 1041, 1997.

33. Jane M. Lehr, Carl E. Baum, William D. Prather and Robert J. Torres, "Fundamental Physical Considerations for Ultrafast Spark Gap Switching", in *Proc. of Ultrawide Band short pulse Electromagnetic conf.* pp. Pages: 11 – 20,1998

34. P. Persephonis, K. Vlachos, C. Georgiades, and J. Parthenios,"The inductance of the discharge in a spark gap" *J. Appl. Phys.* 71 (lo), 15 May 1992.

35. Ryo Ono, Masaharu Nifuku, Shuzo Fujiwara, and Sadashige Horiguchi,Tetsuji Odab. “Gas temperature of capacitance spark discharge in air”, *J. Appl. Phys.* 97,2005

36. Reza Najafzadeh and Ernest E. Bergmann“Nanosecond evolution of a low-inductance air spark”, *J. Appl. Phys.* 59, 269,1986

37. A.Wells “Numerical Calculations of the Properties of Axially Symmetric Arc Columns”, in *R.A.E. Tech. Report No. 67076*--A.R.C. 29 301.

38. E. Bishop, “Low-Inductance 100kV Switch (Spark Gap) For Starting, Diverting and Clamping Capacitor Discharges”, in *Proc. of the Institute of Engineers*, pp. 1549 – 1556,1966.

39. Alan H. Cookson, “Review of high-voltage gas breakdown and insulators in compressed gas”*, IEE Proc, Vol. 128, No. 4, May1981*

40. T.H.Martin etal; “J.C.Martin on pulsed power”: Springer 1996

41. Yu.P. Raizer; “Gas Discharge Physics”: Springer, 1991

42. Z Lj Petrovic, N Skoro, D Maric, C M O Mahony, P D Maguire, M Radmilovic-Radenovic and G Malovic “Breakdown, scaling and volt–ampere characteristics of low current micro-discharges” *J. Phys. D: Appl. Phys. 41, (2008) 194002.*

43. M. Pejovic et al., “Analysis of low-pressure dc breakdown in nitrogen between two spherical iron Electrodes” Phys. Plasmas, 13 (2006) 022108

44. Momcilo M Pejovic, Goran S Ristic and Jugoslav P Karamarkovic; “Electrical breakdown in low pressure Gases” *J. Phys. D: Appl. Phys., 35(2002) R91*

45. M. Klas, Š. Matejčik, , B. Radjenović, and M. Radmilović-Radjenović,“Measurements of the volt-ampere characteristics and the breakdown voltages of direct-current helium and hydrogen discharges in microgaps” *Physics of Plasmas 21, (2014) 103503.*

46. S. Kuhlbrodt, R. Redmer, H. Reinholz etal; “Electrical Conductivity of Noble Gases at High Pressures” *Plasma Phys. vol. 45, No. 1, pp. 61 – 69,2005.*

47. P. Swarbrick; “Composition and properties of a sulphur hexafluoride arc plasma” *J. Appl. Phys. vol. 18 pp.419,1967*

48. Yasunori Tanaka, Yasunobu Yokomizu, Motohiro Ishikawa, and Toshiro Matsumura; “Particle Composition of High-Pressure SF_6 Plasma with Electron Temperature Greater than Gas Temperature” *IEEE Transactions on Plasma Science, vol. 25, no. 5, october 1997.*

49. Pascal Andre; “Partition Functions and Concentrations in Plasmas out of Thermal Equilibrium” *IEEE Transactions on Plasma Science, Vol. 23, No. 3, 1995*

50. B. Bottin, D. Vanden Abeele, Th.E. Magin, P. Rini; “Transport properties of collision-dominated dilute perfect gas mixtures at low pressures and high temperatures “ *Progress in Aerospace Sciences vol. 42 pp. 38–83,2006.*

51. F.J.Smith; “The Numerical Evaluation of The Classical Angle of Deflection and of The J.W.K.B. Phase Shift” *Physica Volume 30, Issue 3, pp. 497–504,1964.*

52. D. Bruno, C. Catalfamo, and A. Laricchiuta etal; “Convergence of Chapman-Enskog calculation of transport coefficients of magnetized argon plasma”, *Physics of Plasmas vol. 13,pp. 072307 ,2006.*

53. Yu.L. Stankevich and V.G. Kalinin; “Fast electrons and X-radiation in the initial stage of pulse spark discharge development in air” , *Doklady Akademii Nauk SSSR 177 (1967), pp. 72–73.*

54. S.I.Yakovlenko, “Beams of runaway electrons and discharges in a dense gases, based on a wave of multiplication of background electrons”, *Proc. Prokhorov General Institute, Vol. 63. Prokhorov General Physics Inst., Moscow, Nauka, 2007, 186 pp*

55. Viktor F. Tarasenko , Evgeny Kh. Baksht , Aleksandr G. Burachenko , Igor D. Kostyrya , Mikhail I. Lomaev and Dmitry V. Rybka; "Generation of supershort avalanche electron beams and formation of diffuse discharges in different gases at high pressure", *Plasma Devices and Operations, vol. 16:4, pp. 267-298*

56. Oleg V. Mikheev, Stanislav A. Podosenov, Konstantin Y. Sakharov,Alexander A. Sokolov, Yanis G. Svekis and Vladimir A. Turki; "New Method for Calculating Pulse Radiation from an Antenna with a Reflector", *IEEE Transactions On Electromagnetic Compatibility, Vol. 39, No. 1, February 1997.*

57. C. E. Baum and E. G. Farr, " Impulse Radiating Antennas," in *Ultra Wideband/Short-Pulse Electromagnetics*, pp. 139-147 Plenum Press, New York, 1993.

58. Everett G. Farr "Off-Boresight Field of a Lens IRA" in *Sensor and Simulation Notes*; Note 370, 1994.

59. Sandeep Kumar Singh "RF & Microwave technology" M.Tech Desertion, Indian Institute of Technology, Khargapur.2010.

60. David M. Pozar; "Microwave Engineering" John Wiley & Sons (Asia), 1989

61. J Reece Roth, Jozef Rahel, Xin Dai and Daniel M Sherman "The physics and phenomenology of One Atmosphere Uniform Glow Discharge Plasma (OAUGDP™) reactors for surface treatment applications" *J. Phys. D: Appl. Phys. vol. 38 (2005) pp. 555–567.*

Appendix-I

Statistical Analysis of Experimental Data

Statistics of experimental results are quantified using certain parameters. Those parameters are defined as follows

Independent variable = x_i ; dependent variable = y_i;

Number of data points = n; degrees of freedom = m;

$$\bar{x} = \frac{\sum_{i=0}^{n} x_i}{n} \quad \text{(A.1)}$$

$$\bar{y} = \frac{\sum_{i=0}^{n} y_i}{n} \quad \text{(A.2)}$$

Residual sum of squares for linear fit i.e. $y = a_1 + a_2 x$ can be written as

$$S_R = \sum_{i=0}^{n} (y_i - a_1 - a_2 x_i)^2 \quad \text{(A.3)}$$

Mean squared error is defined as

$$s^2 = S_R/(n - m) \quad \text{(A.4)}$$

Square root of s^2 gives an estimate of common standard deviation of measurement of *y*

Goodness of fit can be tested using R-square criteria, which suggests that if R-square value is greater than 0.9, then high degree of correlation exists between data and fit. If R-square is between 0.8-0.9 it indicates 'somewhat fit'. If R-square is less than 0.8 it indicates data does not match the fit significantly.

R-square is defined as

$$R^2 = 1 - \frac{S_R}{S_D} \quad \text{(A.5)}$$

Where, S_D is total corrected sum of squares which is defined as

$$S_D = \sum_{i=0}^{n} (y_i - \bar{y})^2 \quad \text{(A.6)}$$

Uncertainty in measurement

Uncertainty in fitting parameters can be defined as follows:

Standard error in intercept

$$se_{a1} = \sqrt{\frac{S_{a1}}{(n-m)}} \tag{A.7}$$

Standar error on slope

$$se_{a2} = \sqrt{\frac{S_{a2}}{(n-m)}} \tag{A.8}$$

Where S_{a1} & S_{a2} is defined as follows

$$S_{a1} = \frac{n\sum_{i=0}^{n} y_i^2 - \left(\sum_{i=0}^{n} y_i\right)^2 - a_2^2 n \sum_{i=0}^{n} x_i^2 - a_2^2\left(\sum_{i=0}^{n} x_i\right)^2}{\left(n\sum_{i=0}^{n} x_i^2 - \left(\sum_{i=0}^{n} x_i\right)^2\right)(n-m)} X \frac{\sum_{i=0}^{n} x_i^2}{n} \tag{A.9}$$

$$S_{a2} = \frac{n\sum_{i=0}^{n} y_i^2 - \left(\sum_{i=0}^{n} y_i\right)^2 - a_2^2 n \sum_{i=0}^{n} x_i^2 - a_2^2\left(\sum_{i=0}^{n} x_i\right)^2}{\left(n\sum_{i=0}^{n} x_i^2 - \left(\sum_{i=0}^{n} x_i\right)^2\right)(n-m)} \tag{A.10}$$

Tstat value for interception and slope is found using these values as follows

$$tstat_{a1} = \left|\frac{e_1.a_1}{S_{a1}}\right| \tag{A.11}$$

$$tstat_{a2} = \left|\frac{e_2.a_2}{S_{a2}}\right| \tag{A.12}$$

Probability of uncertainty can be found from two sided t-test once tstat values of slope and interception is known.

Appendix II

Experimental evaluation of arc channel inductance data

Experimentally obtained arc channel inductance data for different gap and pressure

Pressure Of N_2	Inductance (nH) of 1mm gap	Inductance (nH) of 2mm gap	Inductance (nH) of 4mm gap	Inductance (nH) of 6mm gap	Inductance (nH) of 8mm gap	Inductance (nH) of 10mm gap
0	8.19	6.83	9.56	10.9	15.8	20.5
0	6.83	6.83	13.7	10.9	13.1	27.3
0	5.46	6.83	8.19	12.3	15	25.9
0	5.46	8.19	10.9	12.3	16.4	23.2
0.5	5.73	6.83	9.56	11.5	17.7	24.6
0.5	6.55	10.9	10.9	10.9	18.8	21.8
0.5	5.73	10.9	13.1	9.56	18.6	21.3
0.5	6.55	5.46	8.19	13.7	15	20.5
1	5.73	6.83	8.19	10.9	18.6	22.1
1	6.55	6.83	13.7	11.5	17.2	20.5
1	6.83	6.83	8.19	10.6	17.7	24.6
1	6.55	5.46	10.9	9.56	18.8	21.8
1.5	6.83	5.46	13.7	10.9	18.6	
1.5	6.83	6.83	10.9	13.7	17.2	
1.5	7.37	6.83	13.7	10.9	17.7	
1.5	7.37	6.83	13.9	12.3	16.7	
2	5.46	8.19	10.9	12.3	16.9	
2	5.46	8.19	13.1	15.8	16.4	
2	6.83	8.19	9.56	12.6	15.3	
2	6.83	8.19	12.3	13.1	17.7	
3	5.46	6.83	10.6	14.2		
3	6.01	8.19	9.56	14.7		
3	6.55	6.83	12.3	15		
3	6.28	7.65	12.8	13.4		
4	7.65	9.56	11.7			
4	7.1	8.19	10.9			
4	6.01	9.56	13.7			
4	7.65	6.83	13.1			
5	7.92	5.46	10.6			
5	6.55	6.01	13.7			
5	7.37	7.37	13.4			
5	6.83	8.19	13.9			

Voltage measured across copper sulphate load under different gap and pressure condition of sparkgap and FFT of the same

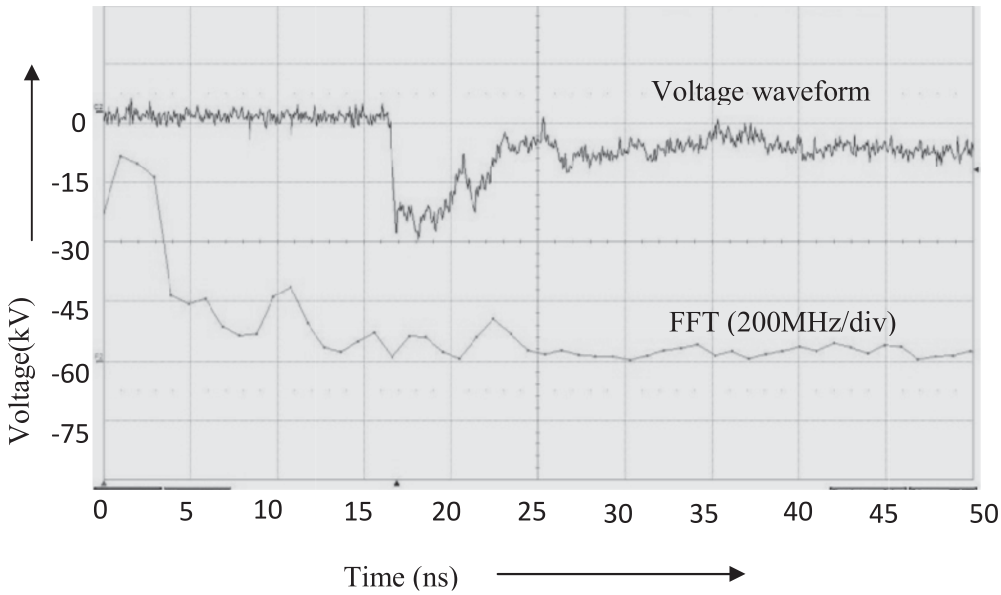

a)Voltage pulse with 2 mm gap at normal atm. pressure

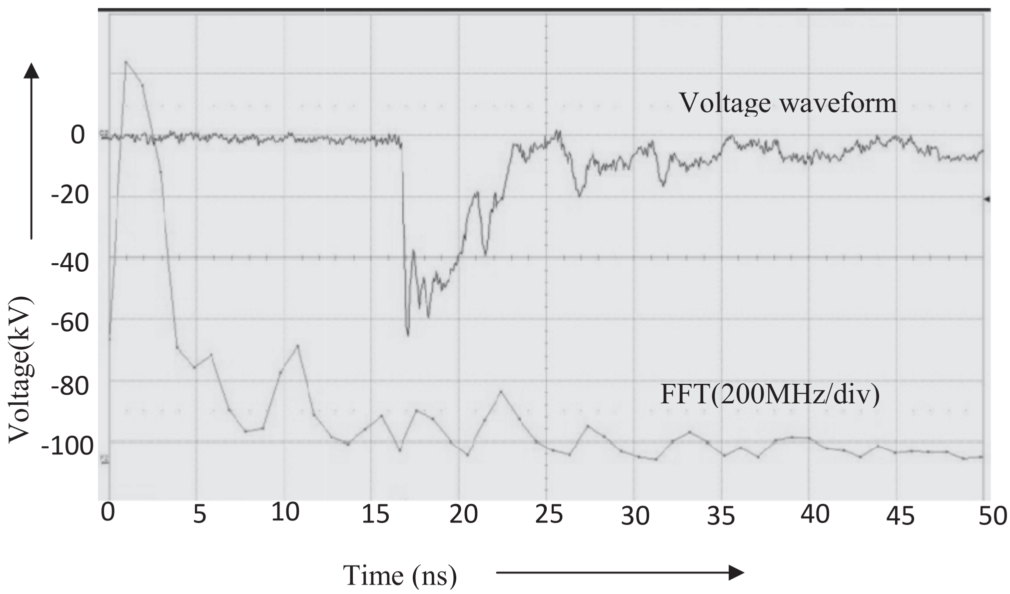

b) Voltage pulse with 4 mm gap at 3 kg/cm^2. pressure

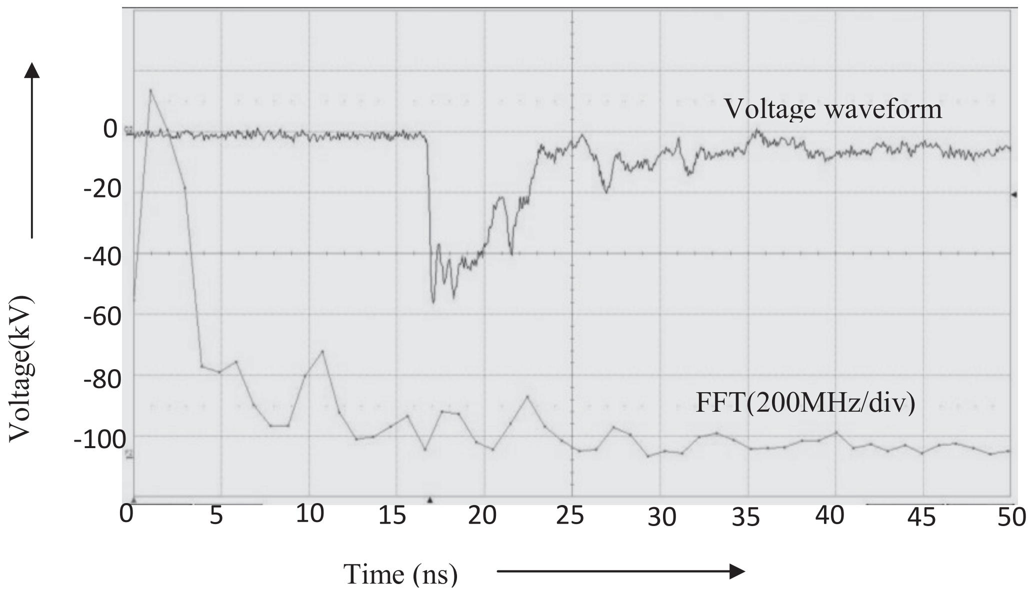

c) Voltage pulse with 4 mm at 1 atm. pressure

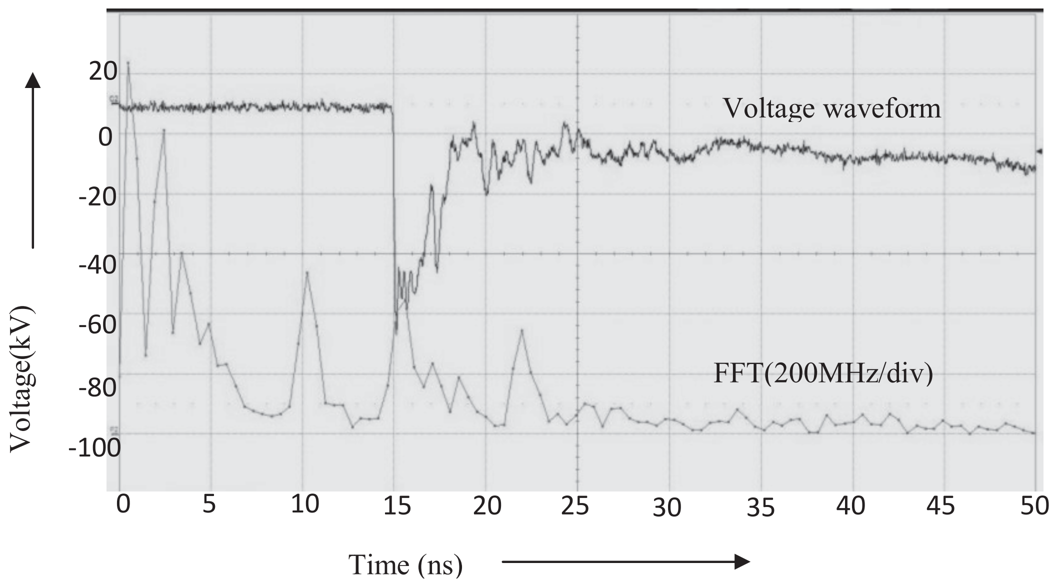

d) Voltage pulse with 1 mm gap 4kg/cm^2 pressure

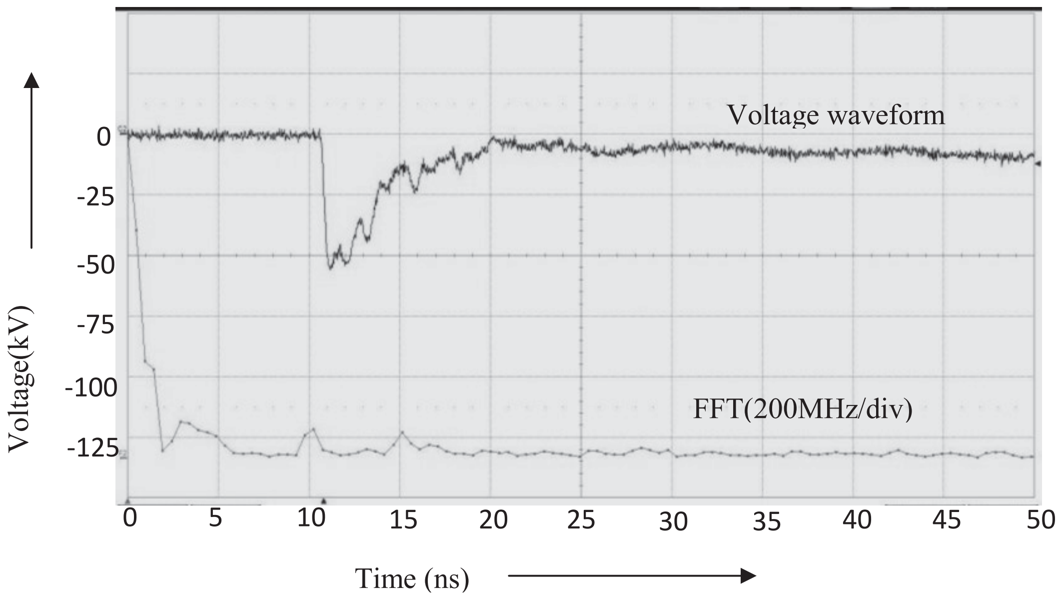

e) Voltage pulse with 8 mm gap 1kg/cm^2 pressure

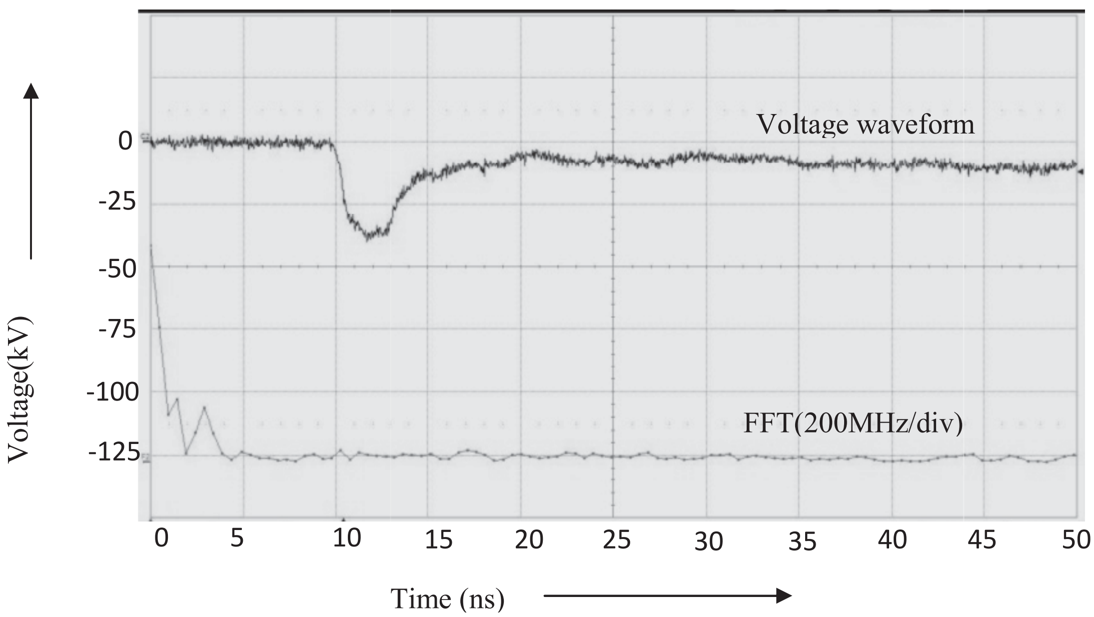

f) Voltage pulse with 10 mm gap normal atm pressure

Appendix III

Arc channel Inductance with respect to Pressure and Gases

Experimentally obtained arc channel inductance data for nitrogen and SF_6 gas at different gas pressure are tabulated below.

Nitrogen gas medium

gas pressure(kg/cm^2)	arc channel inductance(nH)
0	6.375
0	5.95
0	7.225
0	6.375
5	10.625
5	6.8
5	7.225
5	7.225
10	7.225
10	5.95
10	7.225
10	7.65
15	8.075
15	8.5
15	7.65
15	9.35
20	9.5625
20	9.775
20	8.925
20	9.35
25	8.925
25	9.9875
25	10.2
25	8.925
30	9.775
30	10.2
30	11.475
30	9.5625

SF_6 gas medium

gas pressure(kg/cm^2)	arc channel inductance(nH)
0	8.5
0	9.5625
0	9.1375
0	7.65
2.5	8.5
2.5	8.7125
2.5	7.65
2.5	9.1375
5	9.5625
5	8.925
5	9.775
5	9.35
7.5	9.775
7.5	10.2
7.5	9.775
7.5	9.35
10	10.625
10	11.05
10	11.6875
10	9.775
12.5	10.625
12.5	11.05
12.5	11.9
12.5	11.05
15	11.9
15	12.75
15	11.05

List of figures

Abstract

In recent years development of ultra wide band (UWB) high power systems has been taken up by many laboratories worldwide for their industrial, strategic and academic applications. In the thesis attempt has been made to analyze and simulate critical issues related to UWB pulse generation system. A comprehensive literature survey is carried out to study the technologies involved in generating high voltage short (few nanoseconds) pulses with very fast rise time (about a nanosecond). It has been identified that, spark gap switch and its inductance, is one of the major challenges in realizing suitable fast rising high voltage pulse required for UWB applications. Hence a detailed study of spark gap arc channel formation and estimation of its inductance in gaseous medium is carried out in this project. A computer code has been developed to study the complex phenomena of arc channel formation and to estimate its inductance during fast discharge of capacitors. 250 kV Experimental set up has been developed based on MARX generator and a pulse forming line. Study has been carried out by varying gap between electrodes ranging from 2 mm to 10 mm and pressure from atmospheric pressure to 5 kg/cm^2 for inert gas environment of Nitrogen gas. It has been observed that inductance of arc channel increases with increment in gap between electrodes and increment in gas pressure. But variation of inductance with gaps is significantly high compared to that with pressure. To study the effect of high pressure, another experimental set up capable of generating up to 1 MV, has been developed. Inductance of spark gap arc channel is measured with increasing gas pressure in N_2 and SF_6 medium up to 30 kg/cm^2 & 15 kg/cm^2 respectively. Results obtained from experiments are found to be in coherence with simulation results. Details of the computer code developed under this project, simulation results, experimental set up and results of experiments are presented in the thesis.